Multi-Layer Insulation as Contribution to Orbital Debris

Von der Fakultät für Maschinenbau
der Technischen Universität Carolo-Wilhelmina zu Braunschweig

zur Erlangung der Würde

eines Doktor-Ingenieurs (Dr.-Ing.)

genehmigte Dissertation

von:	Sven Kevin Flegel
aus:	Mainz
eingereicht am:	08.11.2013
mündliche Prüfung am:	19.12.2013
Gutachter:	Prof. Dr.-Ing. Peter Vörsmann
	Prof. Dr. Thomas Schildknecht
Vorsitzender:	Prof. Dr.-Ing. habil. Georg-Peter Ostermeyer

2014

This is dedicated to

my family

and to my colleagues and friends at the ILR.

Many things we do naturally become difficult
only when we try to make them intellectual subjects.
It is possible to know so much about a subject
that you become totally ignorant.

– Frank Herbert, *Chapterhouse: Dune*

Contents

List of Figures **v**

List of Tables **vii**

Abstract **xv**

Zusammenfassung **xvii**

1 Introduction **1**
1.1 State of the Art 3
1.2 Scope 5

2 Multi-Layer Insulation in Space Applications **7**
2.1 Common Materials 8
2.2 Configurations 8
2.3 Characterization of Optical Properties 10
2.4 First- and Second Surface Mirrors 12

3 Defining Common Optical Property Parameters **15**
3.1 Equivalent Solar Hours 16
3.2 Overview of Published Results 16
3.3 Reflectivity of Pristine Material 17
3.4 Deterioration Progression 17
3.5 Deterioration Rate 19
3.6 Penetration Depth 21

4 Probability Distributions **23**
4.1 Increasing Section: $\sin$ – Approach 25
4.2 Increasing Section: $1/cosh^2$ – Approach 27
4.3 Decreasing Section: $\sin$ – Approach 28

4.4 Decreasing Section: $1/\cosh^2$ – Approach 29

5 MLI Model History **33**
5.1 MASTER-2009 MLI Applications on Spacecraft 35
5.1.1 MLI on Satellite Buses 35
5.1.2 Radio Frequency (RF) Antennae Sun Shields 37
5.1.3 Area Loading 37
5.2 Effective Area 37
5.2.1 Deformation 38
5.2.2 Tumbling 39
5.2.3 Reflectivity 40
5.3 MASTER-2009 MLI Fragmentation Model 40
5.3.1 Total MLI Area 40
5.3.2 Debris (Fragment) Characteristic Length 42
5.3.3 Debris Fragment Area 43
5.3.4 Debris Fragment Mass 45
5.3.5 Added Velocity 46
5.3.6 Release Time 46
5.4 MASTER-2009 Continuous MLI Source Model 46
5.4.1 Debris Object Characteristic Length 49
5.4.2 Total MLI Area, Debris Object Area and Debris Object Mass 50
5.4.3 Added Velocity 50
5.4.4 Release Time 51
5.5 MASTER-2009 MLI Population 52

6 Orbit Prediction of HAMR Objects **57**
6.1 Overview of Effects 59
6.2 Special Perturbations Model 61
6.3 Extending the Special Perturbations Model 63
6.3.1 Inertially Fixed and Rotating Plates 64
6.3.2 Reflectivity Coefficient 67
6.4 Orbit Evolution of HAMR Objects 68
6.4.1 Common Simulation Parameters 69
6.4.2 Spherical Objects 69
6.4.3 Plates with Inertially Fixed Orienation 74
6.4.4 Plates with Inertially Fixed Rotation Axis 81
6.5 Population Evolution 85

6.5.1 Initial population . . . 86
6.5.2 Average Illuminated Area . . . 86
6.5.3 Comparison of simulation results . . . 88
6.6 Conclusions of Orbit Perturbation Effects . . . 93
6.6.1 Spherical HAMR Objects . . . 94
6.6.2 Oriented and Rotating HAMR Plates . . . 95
6.6.3 Population Evolution . . . 96
6.7 Outlook . . . 97

7 MLI Model Update **99**
7.1 MLI Applications on Spacecraft . . . 100
7.2 Effective Area . . . 102
7.2.1 Deformation . . . 102
7.2.2 Tumbling . . . 103
7.2.3 Reflectivity . . . 103
7.3 MLI Fragmentation Model . . . 106
7.3.1 Complex Fragments from Spacecraft . . . 106
7.3.2 Single Layer Fragments from Spacecraft . . . 108
7.3.3 Titan III Transtage Insulation . . . 109
7.3.4 Added Velocity . . . 110
7.4 Continuous MLI Source Modeling . . . 113
7.5 Updated MLI Population . . . 114

8 Simulating the ESA-SDT Observations **119**
8.1 ESA's Space Debris Telescope Debris Detections . . . 120
8.2 Simulating Fragmentations in GEO . . . 124
8.3 Ariane H10 3rd stage fragmentations . . . 129
8.3.1 1989-006B Fragmentation . . . 129
8.3.2 Simulating Ariane H10 3rd stage fragmentations . . . 130
8.4 Estimating MLI Albedo . . . 132
8.5 Results . . . 133
8.6 Error Analysis . . . 140
8.6.1 Drifting GEO MLI . . . 141
8.6.2 Anomalous GEO Events . . . 142
8.6.3 Velocity Imparted on MLI During Fragmentations . . . 143
8.6.4 Events in Unconventional GEO Regions . . . 144

9 Summary **147**

10 Outlook **151**

References **151**

A Equivalent Solar Hours **163**

B Area-to-Mass Ratio of HAMR Fragments **165**

C Eccentricity versus Effective Area-to-Mass Ratio **167**

D Special Perturbations **169**
D.1 Radiation Pressure 169
D.2 Rotating Motion 170

E Orbit Evolution of Plates **173**

F Average Illuminated Area: $F_{\text{rotating plate}}$ **177**

G Detection Results **179**

List of Figures

2.1 Typical MLI configuration 9
2.2 Schematic of first and second surface mirrors 13

3.1 Increase in solar absorptance $\alpha_\odot$ normalized to 10,000 ESH. . . . 20

4.1 Converting probability density functions for software applications 24
4.2 Schematic of an arbitrary probability density. 26

5.1 Sketch of European Retrievable Carrier (EuReCa) 36
5.2 Structure of MLI fragmentation model. 41
5.3 Characteristic length L_c of MLI fragments from ground tests . . . 43
5.4 Derived fits for characteristic length of shots F and R 44
5.5 Structure of MLI continuous source model. 48
5.6 MASTER-2009 MLI population validation 55

6.1 Selected accelerations on objects orbiting Earth 58
6.2 Vector definition for radiation incident on oriented surface 63
6.3 Spheres: Eccentricity evolution for various area-to-mass ratios . . 71
6.4 Spheres: Inclination evolution for various area-to-mass ratios . . 73
6.5 Spheres: Semi-major axis evolution for various area-to-mass ratios 74
6.6 Spheres: Semi-major axis as function of area-to-mass ratio 75
6.7 Definition of the reference frame for orienation of plates 76
6.8 Fixed plates: semi-major axis change over 1,000 days 77
6.9 Fixed plates: eccentricity change over 1,000 days 78
6.10 Fixed plates: semi-major axis change over 10,000 days 79
6.11 Fixed plates: eccentricity change over 10,000 days 80
6.12 Fixed plates: inclination change over 10,000 days 81
6.13 Fixed plates: evolution of angular momentum unit vector 82
6.14 Rotating plates: semi-major axis change over 10,000 days 83

6.15 Rotating plates: eccentricity change over time 84
6.16 Rotating plates: inclination change over time 85
6.17 Initial HAMR object population 87
6.18 Average annual illuminated area 88
6.19 Eccentricity vs. semi-major axis of propagated population 90
6.20 Eccentricity distribution of propagated population 91
6.21 Inclination vs. RAAN of propagated population 92
6.22 Inclination histogram of propagated population 93

7.1 Escalation of MASTER-2009 MLI population above 10 cm 100
7.2 Surface area per kilogram of spacecraft mass 101
7.3 Probability density distribution for F_{Tumbling}. 104
7.4 Structure of the updated MLI fragmentation model. 107
7.5 MLI fragmentation model characteristic length L_c 109
7.6 Δv applied to MLI fragments 112
7.7 Inclination vs. RAAN of continuous source MLI 113
7.8 Evolution of in-orbit MLI larger than 5 cm over time 115
7.9 Area loading and effective AMR of simulated MLI objects 116
7.10 Spatial object density over altitude of objects larger than 5 cm. . . 117

8.1 ESA-SDT detections from all campaigns performed in 2001. . . . 121
8.2 Inclination vs. RAAN of uncorrelated tracklets 123
8.3 Magnitude histogram of uncorrelated detections from 2004 124
8.4 Overview of GEO fragmentation events from 2001 surveys 127
8.5 Inclination vs. RAAN of tracklets from 2002 to 2007 surveys . . . 128
8.6 Inclination vs. RAAN of 2001 and 2002 surveys 131
8.7 2001 simulated and observed uncorrelated tracklets 134
8.8 2006 simulated and observed uncorrelated tracklets 135
8.9 Inclination vs. RAAN and effective area-to-mass ratio of MLI . . 136
8.10 Histogram of effective area-to-mass ratio ($A/m \cdot C_R$) 137
8.11 Inclination versus effective area-to-mass ratio of GEO MLI 138
8.12 Eccentricity vs. mean motion of all simulated detections 139
8.13 Comparison of detections from 2001 to 2007 surveys 140
8.14 Apparent magnitude histogram from 2001 and 2006 surveys . . . 141
8.15 Δv distribution among GEO fragmentation MLI debris 144
8.16 Influence of fragmentation Δv on detections of MLI 145

C.1 Spheres: Maximum eccentricity versus effective area-to-mass ratio 168

D.1 The body frame has its origin in the center of mass 172

E.1 Fixed plates: Change in semi-major axis over 1,000 days 174
E.2 Fixed plates: Change in semi-major axis over 10,000 days 175
E.3 Fixed plates: Change in eccentricity over 1,000 days 176

List of Tables

2.1 Multi-layer insulation materials 8
2.2 First surface mirror optical properties 14
2.3 Second surface mirror optical properties 14

3.1 Equivalent solar hours on selected surfaces 16
3.2 Overview of satellites carrying THERME experiment 17
3.3 Optical properties from ground and in-situ measurements 18
3.4 Degradation time for LEO and GEO orbits 21

4.1 Equations required for determining α 31

5.1 MASTER-2009 area loading parameters. 38
5.2 MASTER-2009 MLI Fragmentation Model characteristic length L_c 45
5.3 MASTER-2009 Continuous MLI Source characteristic length L_c . 50
5.4 MASTER-2009 Continuous MLI Source release time 52
5.5 MASTER-2009 MLI detections 53
5.6 Simulated number of in-orbit objects for May 1st, 2009 54

6.1 Effect of radiation pressure model on the position prediction . . . 60
6.2 Reflectivity coefficient $C_R \equiv \|\boldsymbol{R}\|$ values for a sphere 68
6.3 Common parameters for orbit evolution analysis 69
6.4 Comparison of HAMR object evolution 96

7.1 Area-to-mass ratio distribution of fragments from ground tests . 103
7.2 Estimated parameters of Titan III Transtage components 111

8.1 List of GEO fragmentation events from MASTER-2009 125
8.2 Revised list of GEO fragmentation events. 126
8.3 1989-006B Ariane H10 3$^{\text{rd}}$ stage fragmentation event. 130
8.4 Simulated Ariane H10 3$^{\text{rd}}$ stage fragmentations 132

8.5 Estimating the MLI object albedo for validation with *PROOF* . . 132

B.1 Area-to-mass ratio distribution of fragments from ground tests . 165

G.1 Comparison of detections from ESA-SDT's 2001 to 2007 180

Nomenclature

Abbreviations

Abbreviation	Description
AIUB	Astronomical Institute of the University of Bern
BOL	Beginning-of-life
CNES	Centre National d'Etudes Spatiales
EOL	End-of-life
ESA	European Space Agency
GEO	Geostationary Orbit
GSO	Geosynchronous Orbit
GTO	Geotransfer Orbit
HAMR	High Area-to-Mass Ratio
HEO	Highly Eccentric Orbit
IADC	Inter-Agency Space Debris Coordination Committee
ISON	International Scientific Optical Network
ITO	Indium tin oxide
LEO	Low Earth Orbit
LST	Local Solar Time
KIAM	Keldysh Institute of Applied Mathematics
MASTER	Meteoroid and Space Debris Terrestrial Environment Reference
MEO	Medium Earth Orbit
MLI	Multi-Layer Insulation
PROOF	Program for Radar and Optical Observation Forecasting

Abbreviation	Description
RAAN	Right ascension of ascending node (see also Ω)
RSW	Satellite coordinate system with $\boldsymbol{R}$ pointing towards the satellite, $\boldsymbol{W}$ being normal to the orbit plane and with $\boldsymbol{S}$ pointing along-track.
SDT	Space Debris Telescope
SRP	Solar radiation pressure
SSM	Second surface mirror
VOP	Variation of parameters

Glossary

Convention	Description
X	Scalar
$\|X\|$	Absolute value of scalar
$\boldsymbol{X}$	Vector
$\|\boldsymbol{X}\|$	Magnitude of vector
$\hat{\boldsymbol{X}}$	Unit vector
$\underline{X}$	One-dimensional array
$\underline{\underline{X}}$	Two-dimensional array
$\underline{\underline{X}}_B^A$	Rotation matrix (also: direction cosine matrix) from frame 'A' to frame 'B'
$[\boldsymbol{X}\times]$	Vector product matrix of vector $\boldsymbol{X}$
$\circ$	Vector multiplication
$\cdot$	Scalar multiplication

Latin Symbols

Abbreviation	Description
$\boldsymbol{R}$	reflectance with directional information (see also C_R)
C_R	reflectivity coefficient ($\equiv \|\boldsymbol{R}\|$) $\in [1,2]$
A	area
m	mass
m/A	area loading
A/m	area-to-mass ratio
$(A/m) \cdot C_R$	effective area-to-mass ratio
mil	1 mil = 0.001 inch = 25.4 μm

Orbit Parameters

Abbreviation	Description
a	Semi-major axis
e	Linear eccentricity
ϵ	Numerical eccentricity
i	Inclination
ν	True anomaly
ν_E	Eccentric anomaly
ν_M	Mean anomaly
Ω	Right ascension of ascending node
ω	Argument of perigee

Greek Symbols

Abbreviation	Description
β	longitude

Abbreviation	Description
λ	latitude
$\alpha_\odot$	absorptivity = solar absorptance = amount of radiation which is absorbed between wavelengths 0.25 and 2.7 μm relative to the energy emitted by the Sun
$\epsilon_\odot$	emissivity = infrared emittance = amount of radiation which is emitted in the infrared spectrum relative to the total energy emitted by a black body radiator
$\rho_\odot$	reflectivity = solar reflectance = amount of radiation which is reflected between wavelengths 0.25 and 2.7 μm relative to the energy emitted by the Sun
τ	transmittance = amount of radiation which is transmitted relative to the incident radiation
Υ	vernal equinox

Indices

Abbreviation	Description
$\oplus$	Earth
$\odot$	Sun
obj	Object

Abstract

The main topic of this thesis is the modeling of multi-layer insulation (MLI) as a potential source for space debris. Observation data which seems to be consistent with the specific properties of multi-layer insulation exists almost exclusively for the geosynchronous orbit region. An emphasis is therefore put on this altitude regime. The European Space Agency's (ESA) reference model for the terrestrial space debris environment MASTER-2009 includes multi-layer insulation as part of the space debris population based on the latest comprehensive models. These rely on several assumptions which lead to a seemingly unrealistic escalation of MLI beyond the validated reference epoch of May 1st 2009. In the frame of the current thesis, published results from ground tests and from in-situ measurements from spacecraft were used to make significant improvements to the MLI fragmentation model. In the course of the work indications increased which suggest that the amount of MLI which is released from spacecraft due to deterioration is subordinate to the amount which is created in fragmentations. For this reason it was decided to rely exclusively on the updated fragmentation model as source for MLI debris. Additional simulations were performed to better understand uncertainties in the orbit prediction of MLI objects due to simplifying assumptions primarily regarding the shape of the objects. A validation of the new model outputs was performed against survey data of the geosynchronous and geotransfer orbit regions which has been obtained using the ESA Space Debris Telescope (SDT). In the course of this validation, strong evidence was found that non-MLI debris created in explosions of Ariane H-10 upper stages between 1984 and 2002 has previously been under-predicted. Specifically the fragmentation cloud of the upper stage with the international designator 1989-006B which exploded on January 1st 2001 could be unmistakably identified in the SDT's data. The simulation results for MLI and non-MLI debris presented in this thesis show good agreement with published observations of the geosynchronous and geotransfer region, supporting the validity of the updated debris population modeling.

Zusammenfassung

Das Hauptthema dieser Dissertation ist die Modellierung von Mehrschichtisolationsfolie (MLI) als potentieller Beitrag zum Weltraummüll. Messdaten, die auf die speziellen Eigenschaften von Mehrschichtisolationsfolie zutreffen, existieren fast ausschließlich für die Gruppe der geosynchronen Bahnen. Aus diesem Grund wird insbesondere dieser Bahnbereich untersucht. Das Referenzmodell zur Beschreibung der terrestrischen Weltraummüllumgebung (MASTER-2009) der europäischen Weltraumbehörde ESA beinhaltet die letzten umfassenden Simulationsergebnisse von Mehrschichtisolationsfolie als Beitrag zum Weltraummüll. Die Modelle auf denen diese Ergebnisse basieren beruhen auf einer Reihe von Annahmen, die durch publizierte Untersuchungen zu den Eigenschaften von Mehrschichtisolationsfolie gestützt sind. Die getroffenen Annahmen führen jedoch in ihrer Summe dazu, dass die Zahl der sich in Umlaufbahnen befindlichen Mehrschichtisolationsfolieobjekte, in der Zeit nach der validierten Referenzepoche 1. Mai 2009, scheinbar unrealistisch schnell ansteigt. Neue Erkenntnisse aus Boden- und In-Situ-Messungen wurden im Rahmen der aktuellen Arbeit genutzt, um Verbesserungen am Modell zur Simulation von MLI Trümmern vorzunehmen, die in Fragmentierungsereignissen erzeugt werden. Im Verlauf der Untersuchungen vermehrten sich die Indizien dafür, dass die Zahl der MLI Objekte, die auf Grund von Degenerationsprozessen freigesetzt werden, der in Fragmentierungen erzeugten untergeordnet ist. Aus diesem Grund wurde die Modellierung der Freisetzung von MLI im weiteren Verlauf auf den fragmentierungsbasierten Prozess beschränkt. Darüber hinaus wurde der Einfluss von Vereinfachungen der Geometrie von MLI-Fragmenten auf die Entwicklung der Umlaufbahn um die Erde in weiteren Simulationen untersucht. Die Ergebnisse des neuen MLI Modells wurden zur Validierung mit Beobachtungsdaten des geostationären- und Geotransferbahnbereichs verglichen, die mittels des Weltraummüllteleskops (SDT) der ESA erzielt worden sind. Während dieser Untersuchungen wurden Hinweise gefunden, die darauf hindeuten, dass die Zahl der nicht-MLI Trümmer, die in Explosionen von Raketenoberstufen des Typs H-10

der Arianeträgerrakete zwischen den Jahren 1984 und 2002 entstanden sind, bislang deutlich unterschätzt worden ist. Besonders hervorzuheben ist hierbei die Explosion der Oberstufe mit der internationalen Bezeichnung 1989-006B am 1. Januar 2001. Es konnte eindeutig gezeigt werden, dass die hierbei entstandene Trümmerwolke durch das Weltraummüllteleskop (SDT) der ESA in demselben Jahr beobachtet wurde. Die Simulationsergebnisse, die in dieser Dissertation präsentiert werden, weisen gute Übereinstimmung mit publizierten Daten aus Beobachtungen des geostationären und geotransferbahnbereichs auf, wodurch die Validität der Modellierung bestärkt wird.

Chapter 1

Introduction

In early 2012, more than 16,000 objects larger then 10 cm were known to orbit Earth. About 3,500 of these were classified as satellites and less than 1,000 of these were thought to be active. In total, over 93 % of objects which were contained in the largest publicly available catalog were defined as *space debris*. This term describes all "*man made objects including fragments and elements thereof, in Earth orbit or re-entering the atmosphere, that are non functional.*" (IADC 2002) The largest space debris objects are satellites and rocket bodies which remained on orbit after their mission had been completed. Up to May 2009, fragments from over 230 explosion and collision events had been released, making up well more than half of all known Earth orbiting objects larger than 10 cm. Spacecraft which were returned from orbit reveal that the number of objects around Earth increases quickly towards smaller sizes. Among the known debris sources are Sodium-Potassium Droplets located primarily at around 900 km altitude at inclinations near 63 degrees, slag and dust from solid rocket motor firings and surface degradation products such as paint flakes and ejecta.

An unexpected space debris population was discovered during surveys of the geostationary transfer orbit region which were initiated in 1999. The observations were performed using the European Space Agency's 1 m Ritchey-Chrétien **S**pace **D**ebris **T**elescope (ESA-SDT) which is located in Tenerife. Disovery of the new population was first published in 2004 by (Schildknecht et al. 2004). The objects had mean motions similar to GEO but generally exhibited high eccentricities and quickly changing orbit parameters and brightness levels. Since the start of these surveys the source has been confirmed by other observations by the ESA-SDT (Schildknecht et al. 2010, 2008b) and also with other systems such as the **I**nternational **S**cientific **O**ptical **N**etwork known as 'ISON' (Molotov et al.

2008, Agapov et al. 2009). An idea had been that if an object with a very high area-to-mass ratio were released in GEO, radiation pressure could potentially force it into orbits similar to those seen during the surveys. This hypothesis has since been investigated and confirmed by independent groups (Kelecy and Jah 2009a). A likely source for these objects is **M**ulti-**L**ayer **I**nsulation (MLI) foil which is used for thermal insulation on almost all satellites and some apogee kick motors. Although this material is the favored candidate today, no direct proof could be obtained yet. MLI has very high area-to-mass ratios of up to $115\,m^2/kg$ (Sheldahl 2012) and employs thin metallic coatings which make the material highly reflective. These two features lead to high susceptibility to radiation pressure effects.

Although **H**igh **A**rea-to-**M**ass **R**atio (HAMR) objects have high reflectivity and can be detected easily with today's telescopes, their orbit parameters often change quickly and cannot yet be predicted accurately. The main danger resulting from this is that even very large HAMR objects are difficult to catalog and collisions can therefore not be predicted reliably. The largest publicly available catalog of objects includes both active and passive objects and contained more than 16,000 objects in spring 2012. Responsibility for this catalog, referred to as "Satellite Situation Report," resides with the United States Strategic Command (USSTRATCOM). The orbit data is provided by the Space Surveillance Network (SSN), which is subcontracted by JSpOC (**J**oint **S**pace **O**perations **C**enter) USSTRATCOM (Johnson et al. 2007). This catalog however does not contain any of the objects under consideration here. In the aftermath of the 1999 observations by ESA's SDT, two catalogs have been created mostly for scientific purposes which track some HAMR objects. These are maintained through the ISON, the **A**stronomical **I**nstitute of the **U**niversity of **B**ern (AIUB) and ESA (Agapov et al. 2008, Schildknecht et al. 2010).

The capability to predict the orbit evolution of any object is based on having a sufficient understanding of the related orbit perturbations. In addition, software is required which can accurately calculate these orbits. Different approaches exist by which the required quantities can be determined. Methods are being developed which require no a-priori information of the objects' properties and may result in sufficiently accurate parameters resulting in successful re-acquisition (Kelecy et al. 2011, Kelecy and Jah 2011). The approach chosen in this dissertation is based on trying to understand the properties of these objects by studying

their origin. Specifically the possibility is examined that the observed HAMR objects could be fragments of multi-layer insulation. To determine the likelihood of this material contributing to the unknown source, two statistical models were developed for simulating the creation of MLI during fragmentation events and by release of MLI debris as a result of material degradation. It is the subject of the current work to revise, update and validate these models and to gain a better understanding of the orbit evolution of HAMR objects.

1.1 State of the Art

Modeling MLI

ESA's MASTER-2009 is the first model to include multi-layer insulation (MLI) as a debris source for the purpose of estimating the collision risk to spacecraft. The underlying MLI debris population is created through two independent models: MLI objects released during fragmentation events and a continuous source of MLI wherein parts of MLI or even entire blankets may detach from satellites and rocket bodies over time.

The MLI model version included in the MASTER-2009 model has been validated for the years 2001 to 2007 against optical observations of the GEO region. These observations were performed by the Astronomical Institute of the University of Bern (AIUB) using ESA's Space Debris Telescope. The simulated MLI population seemed to explain detections in regions to which no other debris source contributed. Not only did the qualitative results match, but also a quantitative analysis with respect to the number of detections revealed good correlation with the observations (Flegel et al. 2011b).

Projecting these models into the future however revealed a significant shortcoming in that the delamination process lead to an accelerated growth in the MLI population. By 2060, MLI objects had increased unrealistically, outweighing all other debris sources. In the released version of the MASTER-2009 software, the future generation of MLI was therefore omitted.

Orbit Evolution and Observations

The orbit evolution of objects in Earth orbit depends on the type of orbit as well as the object's properties. The quicker the orbit parameters change, the more difficult it is to predict their evolution. The complexity increases when the effect of non-conservative forces such as atmospheric drag, lorentz forces or radiation pressure with eclipse consideration are on the order of or larger than other perturbations. The very high area-to-mass ratio of MLI as well as the high reflectivity result in a high susceptibility to at least the two former effects. As the surfaces of MLI are metalized, also the latter effect may have to be considered for correct modeling.

Tracking of objects with quickly changing orbit parameters is difficult. Propagation techniques and filters must be accurate enough to correctly correlate new detections with known objects. In April 2011, Vladimir Agapov presented at the Inter-Agency Space Debris Coordination Committee (IADC) meeting in Berlin, that 270 objects with apparent area-to-mass ratios above 0.9–1 m^2/kg were being successfully held in the KIAM (**K**eldysh **I**nstitute of **A**pplied **M**athematics) database established and maintained by the ISON. The ISON is a purely scientific project which was initiated by KIAM of the **R**ussian **A**cademy of **S**ciences (RAS) and was later joined by the Pulkovo Astronomical Observatory of the Russian Academy of Sciences.

Accurate initial orbit determination as well as the prediction of the position of such HAMR objects for tracking purposes is also being studied extensively by the AIUB, the Air Force Research Laboratory and The Boeing Company. One of the basic tools for such work is numerical orbit propagation. Due to the dominating acceleration of radiation pressure, studies have been conducted to characterize the influence of object orientation, shape and radiative properties on the position prediction accuracy. It was revealed that the position error due to these affects followed non-gaussian distributions (Kelecy and Jah 2009a,b, DeMars et al. 2009). In further studies, different filters were tested by which the true probability density function (pdf) of the state error could be estimated. Amongh them were Adaptive Gaussian Mixture filters (DeMars et al. 2009), extended Kalman filters (EKF), unscented Kalman filters (UKF), and a Gaussian mixture model (GMM) (Kelecy et al. 2011, DeMars et al. 2011).

HAMR Object Properties

To correctly predict the orbit evolution of HAMR objects requires in-depth knowledge of the fragment properties. The area-to-mass ratio, orientation, three-dimensional shape, absorptivity, diffuse and spectral reflectivity, as well as changes in these properties significantly influence the orbit evolution. Deriving optical properties from observations is the object of current studies (Musci et al. 2010, Früh and Schildknecht 2010, Schildknecht et al. 2008b,c). Until this data can be determined reliably from measurements, only very rough estimates can be made as to the actual size and orientation or tumbling of observed HAMR fragments. Ground based studies help in estimating these properties as well as the effects of deterioration processes on the optical and mechanical properties. Fragment shapes have been characterized in ground tests which were performed at Kyushu University, Japan in cooperation with NASA's Orbital Debris Program Office. In two experiments, small test satellites, covered in MLI, were fragmented and the debris was analyzed (Murakami 2008). Some information on the tumbling motion of observed objects may be derived from fluctuations in the observed magnitude (Schildknecht et al. 2008b,c). Much research is still required in this field and allowances must be made for uncertainties.

1.2 Scope

The first chapter introduces some basic properties of multi-layer insulation. Common materials are researched and the principle parameters required to describe the optical properties of MLI are discussed. This is followed by a definition of common optical property parameters for pristine materials and for the degraded properties resulting from exposure to the space environment. In Chapter 4 the probability functions are derived which were developed for the MLI models and are also used in the updated model presented in later chapters. The MLI model history is briefly described in Chapter 5. Important basic assumptions are outlined and validation results which were attained in the frame of the ESA contract "Maintenance of the ESA *MASTER* Model" are presented. The force model used to predict the orbit evolution of MLI objects assumes all objects to be spheres. Chapter 6 analyzes the influence of the effective area-to-mass ratio as well as the shape and orientation of objects with area-to-mass ratios well above $1\,m^2/kg$ on the medium- and long-term orbit evolution. The chapter also addresses the influence of the assumption of spherical HAMR objects on a large

statistical HAMR object population. The two final chapters deal with fundamental updates to the MLI models (Chapter 7) and a revalidation of the updated MLI population against observations made by ESA's Space Debris Telescope (Chapter 8). A summary and an outlook conclude the thesis.

Chapter 2

Multi-Layer Insulation in Space Applications

Multi-layer insulation (MLI) is a passive means of thermally insulating hardware. Multiple layers of thin, metalized substrate materials are combined to form insulating blankets. Heat transfer is minimized by separating the individual layers either by spatial separation or by insertion of low conductance spacer material. MLI is used to cover all major outer surfaces of typical spacecraft as well as individual internal components. Surfaces which are not covered are those where the functionality would be impaired i.e. solar arrays, radiators. The configuration of an MLI stack varies with the boundary conditions. Sun shields for radio frequency antennae typically consist of less than five layers of MLI, while the satellite bus may be covered by more than 20 layers. The companies Sheldahl and DuPont specialize in manufacturing multi-layer insulation for space applications. However, only Sheldahl provides comprehensive information on their products in the form of the freely available *The Red Book*. Material data will therefore rely heavily on their information. DuPont has registered trademarks on trivial foil names such as *Mylar*®, *Kapton*®and *Teflon*®. In the following, the "®" will be omitted.

The chapter starts out with an overview of foils which are commonly used for MLI. Typical configurations are presented next followed by an introduction into the characterization of optical properties which are relevant to MLI. Finally, two foil types are described which are the main building blocks of MLI.

2.1 Common Materials

Typical substrate materials include polyethylenterephtalat (PET), polyimide (PI) as well as fluorpropylencopolymers (FEP) (Sheldahl 2012). The substrates must be lightweight and flexible, have low outgassing properties under vacuum conditions and must be applicable in a wide range of temperatures. Thermal insulating properties are fashioned through specifically combining substrate materials and vapor depositing aluminum, gold or silver on one or both sides of the substrate. The thickness of the metal layer is on the order of 1000 Å. An overview of common materials is given in Table 2.1. The spacer materials B2A and B4A (also known as *Dacron*) are Polyester nettings with different weaving densities. The thickness is given in *mil* = 0.001 inch = 25.4 μm.

Table 2.1: Multi-layer insulation materials taken from *The Red Book* (Sheldahl 2012)

Material	Density / $\mathrm{g\,cm^{-3}}$	Area loading / $\mathrm{g\,m^{-2}}$			
Spacer Materials					
B2A	–	14.9			
B4A	–	7.1			
Substrate Materials		*Thickness / mil*			
		0.25	0.5	1	5
Mylar (PET)	1.39	8.8	17.7	35.3	176.5
Kapton (PI)	1.42	9.0	18.0	36.1	180.3
Teflon (FEP)	2.15	13.7	27.3	54.6	273.0

2.2 Configurations

The configuration of the passive insulation by thin, metalized foils depends on the design constraints and on the state of the art available at the time when the spacecraft was designed and built. Unfortunately information on the specific MLI design of spacecraft is only rarely published. For this reason, the current section can only give an impression of possible configurations.

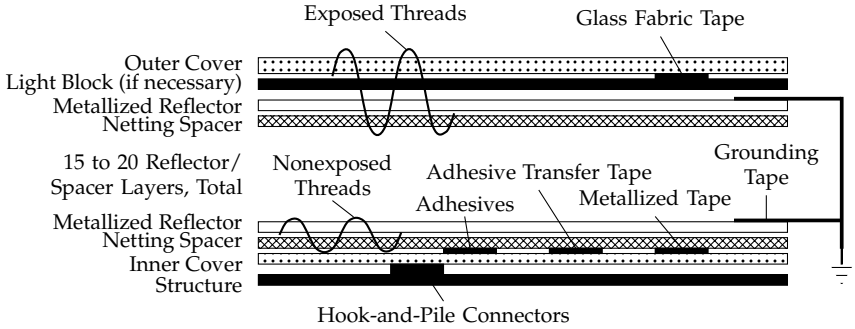

Figure 2.1: Typical MLI configuration reproduced from Finckenor and Dooling (1999) without book sections for better legibility

In 1999, NASA published a technical paper termed *Multilayer Insulation Material Guidelines*, which was a compilation of MLI considerations for future missions based on previous designs such as LDEF or Spacelab (Finckenor and Dooling 1999). In this document, it was stated that 15 to 20 reflector layers are typical for long duration LEO missions. Figure 2.1 shows a common MLI configuration and has been reproduced from Finckenor and Dooling (1999). The outer and inner layers of an MLI stack are typically thicker than the reflector layers in between. According to Sheldahl (2012) common thicknesses are around 5 mil for the outer layers and 0.25 mil for the reflector layers. Material densities range from 1.4 g/cm^3 to 2.2 g/cm^3 (see Table 2.1). Stadermann et al. (1997) and Wright et al. (1995) published additional data concerning the design of the MLI used on the European Retrievable Carrier (EuReCa) spacecraft, which was covered with 22 foil layers. The top layer was a Teflon-coated fiberglass cloth (Beta-cloth) followed by a 3 mil (75 μm) sheet of light-blocking Kapton which was aluminized on one side and had an acrylic overcoat. 19 Kapton reflector layers aluminized on both sides with a thickness of 0.3 mil (7.5 μm) were alternated with 20 Dacron net layers. A 3 mil Kapton film was aluminized on the top side and coated with black paint on the rear as the inner cover layer.

In addition to supplying thermal insulation, MLI can also be used to shield radio frequency (RF) antennae. Such *Sunshields* often consist of only one or two layers of very thin polymeric film on which a semiconducting layer of germanium is

usually vapor deposited. Germanium is transparent to radio frequencies and can limit charge buildup (Sheldahl 2012).

2.3 Characterization of Optical Properties

When an object is irradiated, part of the incident radiation is absorbed, some part may be transmitted and some can be reflected. The relation between these parts depends on the object's properties. These properties will be referred to as the absorptance α, the transmittance τ and the reflectance ρ. All of these are frequency dependent parameters and should therefore correctly be written as $\alpha(\lambda)$, $\tau(\lambda)$ and $\rho(\lambda)$ where λ is the wavelength. Integrating over all wavelengths of the incident radiation, one can describe the relation between these three effects through:

$$\alpha + \tau + \rho = 1 \tag{2.1}$$

If the source for the incident radiation is the Sun, then the wavelengths over which must be integrated are defined by the solar spectrum of electromagnetic waves. In the current thesis, the solar specific values will be termed *solar absorptance*, *solar transmittance* and *solar reflectance* or simply *absorptivity*, *transmissivity* and *reflectivity*. Unless otherwise stated, the parameters then receive the index "$\odot$." For space debris applications it is common to neglect the transmittance, resulting in the simpler relation:

$$\alpha + \rho = 1 \tag{2.2}$$

If the angle of the incident radiation and the reflected radiation to the surface normal are the same, *specular* reflection is taking place. This is similar to a ball bouncing off a wall. This occurs for perfectly smooth surfaces. If the surface is not perfectly smooth, radiation is reflected into random directions and is then called *diffuse*. Real surfaces reflect part of the incident radiation specularly and part of it diffusely so that $\rho = \rho_d + \rho_s$. Integrating the frequency dependent parameters over all relevant wavelengths then leads to:

$$\alpha + \rho_d + \rho_s = 1 \tag{2.3}$$

Solar Absorptance The primary quantities which describe the insulating properties of a material are the solar absorptance $\alpha_\odot$ (or simply *absorptivity*) and the

infrared emittance ϵ_{IR} (or *emissivity*). Both vary with wavelength. Solar absorptance describes how much of the Sun's radiation is absorbed by the object. It is calculated by integrating over all wavelengths while weighting $\alpha_{\odot}(\lambda_i)$ at a given wavelength with the amount of incident radiation generated by the Sun at that wavelength $e_{\odot}(\lambda_i)$. The result is divided by the total radiated energy from the Sun $H_{\odot}$. The solar energy is usually given at 1 AU from the Sun for an area of $1\,\text{m}^2$. The Sun emits 97 % of its radiation between wavelengths $0.25\,\mu$m and $2.5\,\mu$m. In practice, sufficient accuracy can be obtained if the solar absorptance is measured for 50 points between the wavelengths $0.25\,\mu$m and $2.7\,\mu$m and replacing the integration with a summation (Pisacane and Moore 1994):

$$\alpha_{\odot} = \frac{\sum_{i=1}^{n} \alpha(\lambda_i)\, e_{\odot}(\lambda_i)}{H_{\odot}} \tag{2.4}$$

Infrared Emittance The infrared emittance (or *emissivity*) characterizes how much radiation a body emits relative to a black body radiator. It is calculated by integrating the product of emittance at a wavelength $\epsilon(\lambda_i)$ and the power output of a black body radiator at that wavelength $e_{\text{black body}}(\lambda_i)$ over all wavelengths and dividing the result by the total power output of a black body radiator. As with absorptivity, the emitted energy is usually given per unit area. According to Wien's Law, the peak power output of an object at room temperature ($\approx 293\,\text{K}$) has a wavelength of $2.9 \times 10^{-3}\,\text{K/m}\,/293\,\text{K} \approx 10\,\mu$m, which is in the infrared wavelength band of 750 nm to about $350\,\mu$m. In practice, the emittance is thus derived by replacing the integration by a sum and using the wavelength range of the infrared spectrum as limits. Kirchhoff's law of thermal radiation states that the absorptance and emittance at a wavelength must be identical ($\alpha(\lambda) = \epsilon(\lambda)$). This then leads to the following derivation:

$$\epsilon_{\text{IR}} = \frac{\sum_{i=1}^{n} \alpha(\lambda_i)\, e_{\text{black body}}(\lambda_i)}{\sigma T^4} \tag{2.5}$$

Reflectivity Coefficient The largest radiation pressure effect results from direct solar irradiation of the fragments. In the very simplest scalar form, the equation for acceleration due to direct solar irradiation is given by:

$$\boldsymbol{a}_{\text{RP}} = -S_{\odot} \frac{\Phi_{\odot}}{c} C_R \frac{A_{\text{eff}}}{m_{\text{obj}}} \hat{\boldsymbol{s}}_{\odot} \tag{2.6}$$

$\boldsymbol{a}_{\text{RP}}$	radiation pressure acceleration vector	m/s
$S_{\odot}$	shadow function for occultation of Sun by Earth $\in$ [0,1]	–
$\Phi_{\odot}$	electromagnetic radiation flux from Sun at object	W/m^2
c	speed of light	m/s
C_R	reflectivity coefficient $\in$ [1,2]	–
A_{eff}	effective area perpendicular to incident radiation	m^2
m_{obj}	object mass	kg
$\hat{\boldsymbol{s}}_{\odot}$	unit direction vector pointing from the reflection center of the sphere to the sun	–

This equation takes into account *only* the acceleration in the direction of the Sun-object vector at a given point in time. The effective area A_{eff} in this case is simplified as being the area perpendicular to the incident radiation. This formulation is accurate for spherical objects. The reflectivity is expressed in the coefficient

$$C_R = 1 + \rho_{\odot} \tag{2.7}$$

where $\rho_{\odot}$ is the material's solar reflectance. In Section 6.3, an extension of the above equation is given for objects made up of multiple flat surfaces and the reflectivity coefficient is expressed as a function of the diffuse and specular reflectivity.

2.4 First- and Second Surface Mirrors

The thermal insulation properties of MLI are characterized by the absorptivity, emissivity and the ratio of absorptivity over emissivity $\alpha_{\odot}/\epsilon_{\text{IR}}$. Whether a substrate is metalized on one or on both sides thus has an important effect on its insulating properties. This section gives a description of the workings of first and second surface mirrors and typical values are presented.

First Surface Mirrors Figure 2.2 shows a schematic of first and second surface mirrors. Absorptivity and emissivity of the metal coating are typically low. The cheaper aluminum is preferred to gold coatings. Gold, or aluminum coated with a corrosion resistant AOC coating are used when longer periods of time are spent in i.e. salty atmosphere conditions as has been the case for the space shuttle. When coating polymeric films on both sides with low emissivity metals, very low radiative heat transfer rates can be obtained. Double sided aluminum

coating on PET or PI is therefore often chosen for the inner reflector layers in MLI blankets. Values for absorptivity and reflectivity of first surface mirrors are given in Table 2.2.

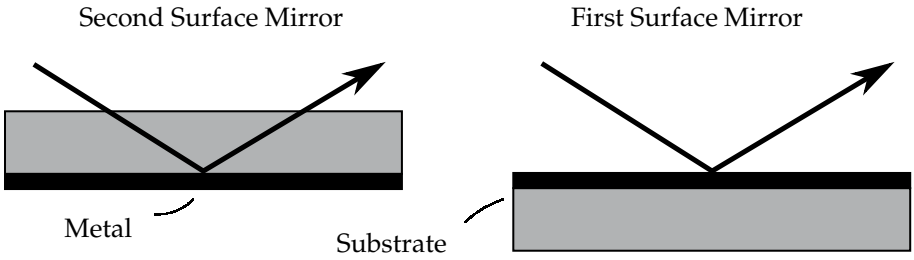

Figure 2.2: Schematic of first and second surface mirrors

Second Surface Mirrors The equilibrium temperature of a surface depends on the ratio of absorbed-to-emitted energy. Decreasing this ratio also lowers the equilibrium temperature. In second surface mirrors, the relatively higher emissivity of the substrate is used to reduce the equilibrium temperature. In this configuration, the emissivity depends on the substrate material and its thickness. Values for absorptivity and reflectivity of first and second surface mirrors are given in Table 2.3.

Table 2.2: First surface mirrors: Absorptivity and emissivity of metal coatings (reproduced from Sheldahl (2012) and Kauder (2005)). Kauder (2005) gives the fraction of IR radiation emitted normal to the surface.

Metal	Sheldahl (2012) Typical Infrared Emittance ϵ_{IR}	Typical Solar Absorptance $\alpha_\odot$	$\alpha_\odot/\epsilon_{IR}$
Gold	0.02	0.28	14
Silver	0.02	0.07	3.5
Aluminum	0.03	0.12	4
	Kauder (2005)		
	Normal Emissivity ϵ_n	Typical Solar Absorptance $\alpha_\odot$	$\alpha_\odot/\epsilon_n$
Aluminum on Black Kapton	0.03	0.12	4.0
Chromium on 5-mil Kapton	0.24	0.57	2.4

Table 2.3: Second surface mirrors: Absorptivity of coatings and emissivity of polymer films (reproduced from Sheldahl (2012)). Inconel® is a registered trademark of international Nickel Company.

Solar Absorptance		*Infrared Emittance*			
Metal	$\alpha_\odot$	Film Thickness		ϵ_{IR}	
		mil	μm	FEP	Polyimide
Silver	0.06 - 0.09	0.5	12.7	0.41	0.52
Aluminum	0.10 - 0.14	1	25.4	0.52	0.64
Copper	0.20 - 0.30	2	50.8	0.65	0.76
Germanium	0.50 - 0.70	5	127.0	0.79	0.85
Inconel®	0.60 - 0.70	10	254.0	0.86	–

Chapter 3

Defining Common Optical Property Parameters

MLI is designed so that most of the incident radiation is reflected away from the spacecraft. Since acceleration due to radiation pressure is directly proportional to the flux of electromagnetic radiation, it follows that this is the primary source for radiation pressure induced orbit perturbations. Good knowledge of realistic reflectivity values is therefore paramount to correctly estimating the resulting acceleration. Due to the relation given in Equation 2.2, also publications which only take into account absorptivity can be used. In the current section, published data from ground tests and in-situ measurements will be used to estimate initial reflectivity values and deterioration progression of typical MLI materials.

Initially, a definition of *Equivalent Solar Hours* is given as this is a common parameter by which the exposure to the space environment is measured. This is followed by an overview of publications which give resilient data of optical properties of materials used for MLI. A mean value is then derived for the reflectivity of pristine foils from the presented data. The deterioration progression found by various authors is compared and a plausible common progression is defined. The chapter closes by an estimation of the deterioration rate for different orbit regimes and mission types and of the penetration depth of some radiation types into MLI foils.

3.1 Equivalent Solar Hours

Ultraviolet radiation is typically measured in equivalent solar hours (ESH). A definition is given by Pisacane and Moore (1994): "equivalent hours normal to the Sun's rays at 1 AU." Table 3.1 gives a reference for average ESH per year for on-orbit time for GEO and LEO orbits.

Table 3.1: Estimated values for equivalent solar hours on selected surfaces of a GEO spacecraft and LEO SSO spacecraft on 12:00 LST orbit and on 6:00 LST orbit. N/S - North/South. E/W - East/West. N/Z - Nadir/Zenith. Sun - Cross track, towards Sun. Derivation of the values is given in Appendix A.

	GEO		SSO 12:00	SSO 6:00
	N/S	E/W & N/Z	N/Z	Sun
ESH per year	886	2712	2790	8522

3.2 Overview of Published Results

Marco and Remaury (2004) studied the effect of UV radiation, electron (e^-) and proton (p^+) radiation on thermal control coatings in a simulated GEO environment. In-situ measurements have been made on LEO by the THERME experiment which was developed by CNES and has flown on several satellites. THERME is a simple low-cost experiment aimed at measuring the aging of solar absorptance $\alpha_\odot$ of thermal coatings. Remaury et al. (2011) evaluated the results retrieved from the experiments located on the three satellites SPOT 5, HELIOS-2A and DEMETER. Mission parameters are listed in Table 3.2.

The initial and degraded absorptivity as well as the absorbed ESH and atomic oxygen from the GEO simulations (Marco and Remaury 2004) and LEO in-situ measurements (Remaury et al. 2011) are listed in Table 3.3. Uncertainties are given for the initial conditions obtained in ground measurements. The initial absorptivity values from the in-orbit measurements are higher than those taken on the ground. No definitive cause was stated by the authors. In Table 3.3, the connotations "V+" and "V–" refer to the satellite sides which were facing in- and

opposite the flight direction. "Sky" denotes the space facing surface. The spacecraft's motion relative to the atmosphere causes the atomic oxygen flux on the trailing surface to be negligible. The conditions on this side are therefore most similar to those found in GEO. Significant differences arise from different e^- and p^+ fluxes and possibly due to differences in solar irradiation.

Table 3.2: Overview of satellites carrying THERME experiment discussed by Remaury et al. (2011)

Name	Int. Desig.	Launch Date	Type	Altitude	Inclination
SPOT 5	2002-021A	05/04/2002	22h30m SSO	820 km	98.7 °
HELIOS-2A	2004-049A	12/18/2004	13h15m[1] SSO	688 km	98.1 °
DEMETER	2004-025C	06/29/2004	22h25m SSO	710 km	98.2 °

3.3 Reflectivity of Pristine Material

The solar absorptance of first and second surface mirror MLI depends for the most part on the metal coating (Compare Tables 2.2 and 2.3 for values of first- and second surface mirrors.). Due to relation 2.2, this also means that the solar reflectance is the same for first- and second surface mirrors. According to Sheldahl (2012), the most common metal coating is aluminum. Solar absorptance for pristine aluminum covered polymers range from 0.10 to 0.14 (Sheldahl 2012, Kauder 2005). In-situ measurements at BOL performed for SPOT 5, HELIOS-2A and DEMETER by Remaury et al. (2011) for second surface mirrors using aluminum/silver on PTFE range from 0.10 to 0.17 (see Table 3.3). For the simulations, a mean reflectivity value is used. It is assumed that all fragments have an initial reflectivity $\rho_0 = 1 - \alpha_0 = 0.87$.

3.4 Deterioration Progression

The test samples studied by (Remaury et al. 2011) exhibit varying trends in deterioration rate. At ESH values between 9,000 and 14,000 hours, all of the alu-

[1] Approximated from orbit data

Table 3.3: Selected results from Marco and Remaury (2004) and Remaury et al. (2011). "V+" and "V–" refer to samples located on the in-flight surface and trailing surface while "Sky" denotes the space facing surface. All samples were second surface mirrors. The absorptivity $\alpha_{\odot,\text{ground}}$ was measured on the ground while the beginning-of-life (BOL) are in-situ measurements. The end-of-life (EOL) values for the GEO case are ground measurement results while all other cases are in-situ measurements. Atomic oxygen fluence is given in atoms per centimeter squared (at cm^{-2}). Atomic oxygen fluence for "V–" sides was negligible and is indicated by "–."

Name	Side	Material Type	$\alpha_\odot$			UV	AO
			Ground	BOL	EOL	/ ESH	/ at cm^{-2}
GEO	–	Al (FEP)	0.08 ± 0.01	–	0.180	3336	–
GEO	–	Al (FEP), ITO	0.08 ± 0.01	–	0.140	3336	–
SPOT 5	V–	Al (PTFE)	0.11 ± 0.04	0.15	0.195	14000	–
SPOT 5	V+	Al (PTFE)	0.11 ± 0.04	0.15	0.240	14000	2.10e+20
SPOT 5	Sky	Al (PTFE)	0.11 ± 0.04	0.17	0.294	18200	1.40e+19
HELIOS-2A	V+	Al (PTFE)	0.11 ± 0.04	0.15	0.185	9000	1.35e+20
HELIOS-2A	Sky	Al (PTFE)	0.11 ± 0.04	0.14	0.231	11700	9.10e+18
HELIOS-2A	V+	Ag (PTFE)	0.09 ± 0.04	0.10	0.121	9000	1.35e+20
HELIOS-2A	V–	Ag (PTFE)	0.09 ± 0.04	0.10	0.140	9000	–
DEMETER	V+	Ag (polymer), ITO	0.11 ± 0.02	0.14	0.180	10800	1.60e+20
DEMETER	V–	Ag (polymer), ITO	0.11 ± 0.02	0.15	0.207	10800	–

minum or silver second surface mirrors seem to follow a rather linear trend. Most other surfaces such as Kapton, Mapatox K, SG121FD and PCBE however exhibit a visible slowing in deterioration rate within the studied range of up to 19,200 ESH. According to Kelecy and Jah (2011), optical properties of MLI asymptotically approach an end-of-life value. They give an initial value of $\rho_\odot = 0.63$ which deteriorates to 0.38 at end-of-life, resulting in a $\Delta\rho_\odot$ of 0.25. Unfortunately the authors do not give any information on the type of the MLI or the method by which their values were obtained. Fischer (2011) also assumed an asymptotic deterioration which stagnates after 15 years of in-orbit time. Using an initial reflectivity of 0.65 he estimated the change from beginning to end of life in solar absorptance to $\Delta\rho_\odot = 0.37$. The latter value relies on equations which were fitted to extremely sparse data for proton, electron and UV induced deterioration. The obtained results must therefore be treated with utmost care.

Since the absorptivity cannot exceed the value 'one' it seems reasonable that also those second surface mirror samples which showed a linear increase in absorptivity should asymptotically approach an end-of-life value. In the following, the average of the values proposed by Kelecy and Jah (2011) and Fischer (2011) will be used as an estimate of the end-of-life value of metalized foils from MLI which is $\rho_{\text{degraded}} = 0.33$.

3.5 Deterioration Rate

The change in absorptivity from Table 3.3 has been normalized for 10,000 ESH and plotted in Figure 3.1. The different materials and orientation of the studied surfaces make a comparison of the results rather challenging. Per 10,000 ESH, the overall change ranges from 0.032 to 0.300. The simulated GEO environment causes the highest change in solar absorptance and is more than twice as high as the highest value observed in the LEO missions. Between surfaces with the same material on one satellite, significant differences are observed for the different sides. Apart from the difference between GEO and LEO results, no definitive trend is observed: The V– side on SPOT 5 exhibited a lower increase than the other two sides. while on HELIOS-2A and DEMETER, the V+ side was the more robust one. The much higher deterioration rate for the GEO samples may be related to the different substrate material, the differences in the charged particle fluences or the fact that the GEO environment was simulated in a ground test.
To gain a rough estimation for the time which is required for the solar reflectance to degrade completely some simplifying assumptions are made. First, a constant degradation rate is assumed starting at the initial value of 0.87 and terminating at the end value of 0.33. Secondly, ESH are assumed to be the sole influencing parameter for the deterioration rate. The degradation rates presented in Figure 3.1 can now be combined with the ESH for significant spacecraft surfaces from Table 3.1. For each case, the time can be calculated which it would take for the optical properties to attain the final value. Table 3.4 shows the resulting time in years for each case. GEO and LEO spacecraft are kept separate to allow for variations in the degradation process due to the different environments.

For GEO, the listed surfaces should adequately represent a typical 3 axis stabilized spacecraft. For LEO, the SSO cases do not cover all surfaces of a LEO

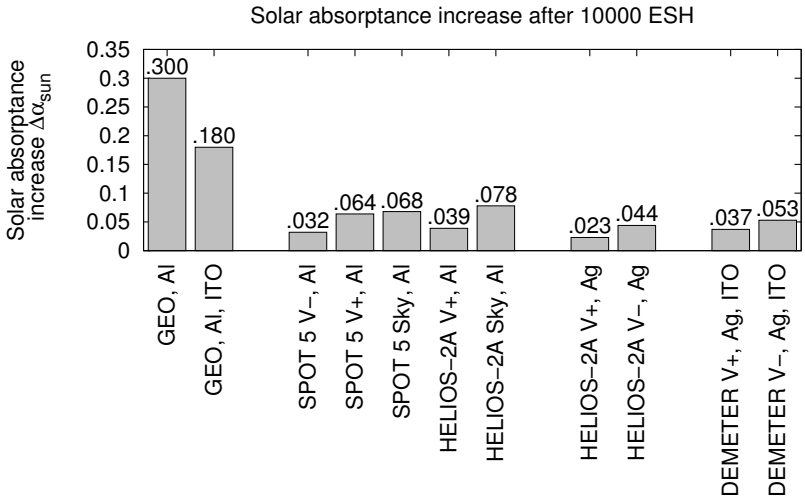

Figure 3.1: Increase in solar absorptance $\alpha_{\odot}$ normalized to 10,000 ESH. Data reproduced from Marco and Remaury (2004) and Remaury et al. (2011)

mission. A line has been added with the ESH of a randomly tumbling plate ($1/4 \cdot 8766\,\mathrm{h/a}$) without occultation of the Sun by the Earth. This should give a better approach to obtaining average results. For GEO, ITO finishing is typically not used (Marco and Remaury 2004) since its prime purpose is to shield against atomic oxygen. Only the results for the simple "GEO Al" case are used for which the end values would be achieved after six to 20 years depending on the surface. GEO spacecraft are typically designed for a 15 year mission lifetime. A degradation time of six years therefore seems unrealistically short. The average of the two given values is 13.5 years. Allowing for a slowing of the deterioration rate towards the end, a value between 15 and 20 years may be more realistic.

LEO missions show a spread between 31 and 107 years with results aggregating between 30 and 80 years for the randomly tumbling plate. The median value is 46.5/56.0 depending on whether or not the highest value of 107.1 is included or not.

Table 3.4: Years until the reflectivity of a spacecraft side will degrade by 0.54 for LEO and GEO orbits. A constant degradation rate is assumed. Values are derived by combining data from Table 3.1 and Figure 3.1. RT Plate = Randomly Tumbling Plate.

	GEO Al	GEO Al, ITO	SPOT 5 V–, Al	SPOT 5V+, Al	SPOT 5 Sky	HELIOS-2A V+, Al	HELIOS-2A Sky, Al	HELIOS-1A V+, Ag	HELIOS-2A V–, Ag	DEMETER V+, Ag, ITO	DEMETER V–, Ag, ITO
GEO N/S	20.3	33.9	–	–	–	–	–	–	–	–	–
GEO E/W	6.6	11.1	–	–	–	–	–	–	–	–	–
SSO N/Z	–	–	60.5	30.2	28.5	49.6	24.8	84.2	44.0	52.3	36.5
SSO SUN	–	–	19.8	9.9	9.3	16.2	8.1	27.6	14.4	17.1	12.0
RT Plate	8.2	13.7	77.0	38.5	36.2	63.2	31.6	107.1	56.0	66.6	64.5

3.6 Penetration Depth

Marco and Remaury (2004) studied the effect of UV radiation, electron (e^-) and proton (p^+) radiation on some thermal control coatings in a simulated GEO environment. The exposure on the north/south faces of a three axis stabilized, geostationary spacecraft over a time frame of three years was simulated. The equivalent sun hours for UV radiation was 3336 ESH. The penetration depth of electrons and protons was looked at for a reference material with a density of $1.5\,\mathrm{g/cm^3}$ which is similar to that of Kapton and Mylar (see Table 2.1). The energy of the electron radiation was 400 keV at a flux of $2.22 \times 10^{10}\,e^-\,\mathrm{cm^{-2}\,s^{-1}}$. Protons were tested for two energy levels: 240 keV and 45 keV at $1.25 \times 10^{11}\,p^+$ $\mathrm{cm^{-2}\,s^{-1}}$ each. The deepest penetration depth was observed for electrons at 400 μm followed by the higher energy proton radiation (3 μm) and the lower energy proton radiation (0.8 μm). Interestingly however, the radiation dose which was absorbed at the different depths was two orders of magnitude lower for the electron radiation ($1 \times 10^{15}\,e^-$ $\mathrm{cm^{-2}}$) than for the low energy proton radiation ($2 \times 10^{15}\,p^+$ $\mathrm{cm^{-2}}$) while the actual fluence was only two times higher from the

low energy proton radiation. While cover layers may have thicknesses on the order of five to 10 mil (127 to 254 μm), the lower reflector layers are typically on the order of 0.5 mil (12.5 μm). The simulated proton radiation would therefore be absorbed by the top cover layer while electron radiation would penetrate several layers.

Chapter 4

Probability Distributions

A simple representation of a model which tries to mimic real life processes requires three components: 1) an input, 2) an output and 3) a model which creates the output based on the given input. When working with unknown factors, i.e. not all input parameters can be obtained or the relation between the input and the output has not been understood completely, these unknowns may be described through probability distributions which are a measure for the likelihood of a certain outcome based on a given input. In theory such models however only give correct results if the outcome of an infinite number of tests is evaluated. Only by chance will individual simulations match a single observed process perfectly. In practice, the number of tests which are performed vary depending on the required precision.

Typically, the probability distributions call for a non-uniform distribution of numbers. In a computational environment, such tests can be simulated by mapping uniformly distributed random numbers onto a probability distribution. Figure 4.1 shows how such a distribution can be obtained. Initially, a *probability density function* is defined. This function approximates the occurrence of different outcomes of a real life process. The area enclosed by this function within defined limits is equal to one. Integrating this equation within these limits produces the *probability function*. This function returns 'zero' for the lower limit and 'one' for the upper limit. Finally, the function is inverted, resulting in the *inverted probability function*. Inserting uniformly distributed values between zero and one into this function will return values between the previously defined model limits. The occurrence of the values from this inverted function will reproduce the initially defined probability density function.

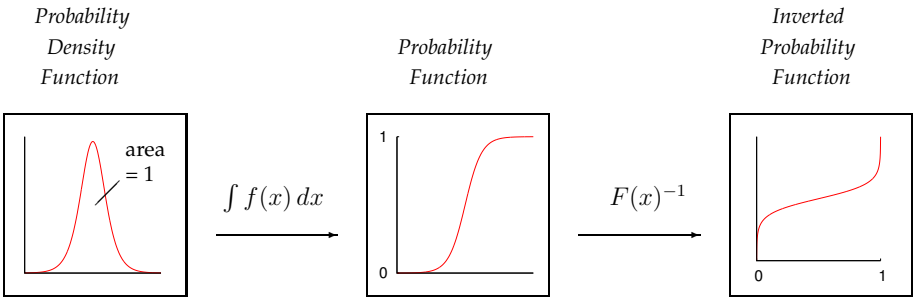

Figure 4.1: Converting probability density functions for software applications

Since very little is known of the mechanisms behind the creation of MLI debris, a major requirement was that the probability distributions needed to be as freely adjustable as possible. The probability density distribution was therefore split into three sections:

1. Zero probability density section
2. Increasing probability density section
3. Decreasing probability density section

This approach requires that the following conditions are met by the derived functions:

- The area under a *probability density function* must be equal to 'one'
- The *probability density function* and its first derivative must be continuously differentiable for the entire non-negative range of the distribution
- The *probability density function* must be integratable, yielding the *probability function*
- The *probability function* must be invertible

A 'zero probability density section' may be required when modeling the time after which parts of MLI start to detach from a parent object. Two interchangeable distributions are derived for the increasing and decreasing density sections respectively. One approach is based on a $1/\cosh^2$ relation. It is roughly bell shaped

and asymptotes to zero at $\pm\infty$. The second approach is simpler and is based on a sin relation. It has a real start and end value where it intersects the x-axis. The current section presents these solutions. The following text including Sections 4.1 to 4.4 have been published in Flegel et al. (2011b) and are reproduced here without alteration.

The surface under a probability density distribution, such as a gaussian distribution, is equal to one. For the set of equations proposed here, a scaling parameter α is introduced which ensures that any combination of increasing and decreasing distributions adheres to this requirement. Figure 4.2 contains the most important elements of the probability density equations. Equation 4.1 is the condition by which α is calculated:

$$\begin{aligned} P_1(\alpha) + P_2(\alpha) &= \int_{\Delta x_0+\delta x_1}^{\Delta x_0+\Delta x_1} p_1(x)\,dx + \int_{\Delta x_0+\Delta x_1}^{\Delta x_0+\Delta x_1+\delta x_2} p_2(x)\,dx \\ &= 1 \end{aligned} \tag{4.1}$$

α	Scaling parameter
P_1	Increasing prob. distribution
P_2	Decreasing prob. distribution
p_1	Increasing prob. density distribution
p_2	Increasing prob. density distribution

The equations needed for the determination of α are given in Table 4.1. The most important parameters used by the equation presented in this section are visualized in Figure 4.2.

4.1 Increasing Section: sin – Approach

In Oswald (2001), a trigonometric equation is used as a probability distribution for modeling space debris. The probability $P(x)$ is defined as

$$P(x) = \frac{1}{2}\left[1 - \cos(\pi\, x)\right] \qquad for\ 0 \leq x \leq 1 \tag{4.2}$$

The probability density $p(x)$ is the derivative of the probability distribution and is the basis for the sin–approach of this study:

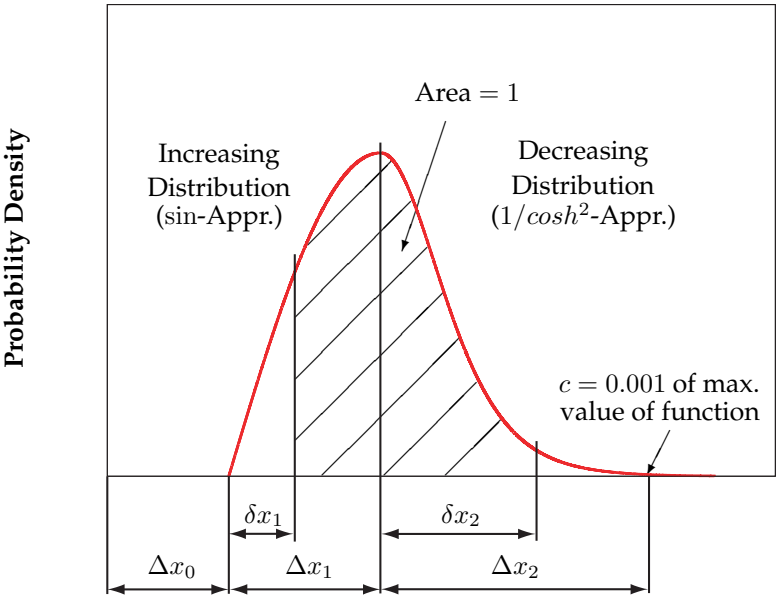

Figure 4.2: Schematic of an arbitrary probability density.

$$\frac{dP(x)}{dx} = p(x) = \frac{\pi}{2} \sin[\pi\, x] \qquad for\ 0 \leq x \leq 1 \tag{4.3}$$

For our case, the probability density, probability distribution and inverse probability distribution are presented in eq. (4.4), (4.5) and (4.6) respectively:
For $\Delta x_0 + \delta x_1 \leq x \leq \Delta x_0 + \Delta x_1$:

$$p_1(x) = \alpha\, A'\, \pi\, \sin[A'\, \pi\, (x - \Delta x_0)] \tag{4.4}$$

$$P_1(x) = \alpha \left(\cos[A'\, \pi\, \delta x_1] - \cos[A'\, \pi\, (x - \Delta x_0)] \right) \tag{4.5}$$

For $0 \leq P_1(x) \leq P_1(\Delta x_0 + \Delta x_1)$:

$$x = \frac{1}{A'\, \pi} \arccos\left[\cos[A'\, \pi\, \delta x_1] - \frac{P_1}{\alpha} \right] + \Delta x_0 \tag{4.6}$$

This increasing probability density distribution starts out with a positive gradient and increases to a local maximum at $\Delta x_0 + \Delta x_1$. Δx_0 is the length of the zero probability section. Δx_1 is the section length from the function's intersection with the abscissa to its maximum. A parameter δx_1 is chosen to offset the start of the distribution density (see Figure 4.2). The parameter A' is chosen such that p_1 has a local maximum at $\Delta x_0 + \Delta x_1$:

$$A' = \frac{1}{2\,\Delta x_1} \tag{4.7}$$

Its function is to ensure that the probability density and gradient are the same for the increasing and decreasing probability density distributions at their joining point. In order to determine α, we need the total area under the probability density distribution given by (4.4) as a function of α:

$$\begin{aligned} P_1(\alpha) &= \int_{\Delta x_0+\delta x_1}^{\Delta x_0+\Delta x_1} p_1(x)\,dx \\ &= \begin{cases} \alpha & : \quad \delta x_1 \le 0 \\ \alpha\,\cos\left[A'\,\pi\,\delta x_1\right] & : \quad 0 < \delta x_1 \le \Delta x_1 \end{cases} \end{aligned} \tag{4.8}$$

4.2 Increasing Section: $1/cosh^2$ – Approach

This increasing probability density distribution asymptotes to $+0$ for $-\infty$ and has a local maximum at the defined value $\Delta x_0 + \Delta x_1$. Equations (4.9), (4.10) and (4.11) are based on the $1/\cosh^2$ term and contain the probability density, probability and inverse probability distributions, respectively. As in the sin–approach, we introduce δx_1 to offset the onset of the increasing probability density distribution.

For $\Delta x_0 + \delta x_1 \le x \le \Delta x_0 + \Delta x_1$:

$$p_1(x) = \frac{\alpha\,A'\,\pi}{\cosh^2\left[A'\,\pi\,(x - (\Delta x_0 + \Delta x_1))\right]} \tag{4.9}$$

$$\begin{aligned} P_1(x) &= \alpha\left\{\tanh\left[A'\,\pi\,(x - (\Delta x_0 + \Delta x_1))\right]\right. \\ &\quad \left. - \tanh\left[A'\,\pi\,(\delta x_1 - \Delta x_1)\right]\right\} \end{aligned} \tag{4.10}$$

For $0 < P_1(x) \leq P_1(\Delta x_0 + \Delta x_1)$:

$$\begin{aligned} x &= \frac{1}{A'\,\pi} \cdot \operatorname{artanh}\left[\frac{P_1}{\alpha} + \tanh\left[A'\,\pi\ (\delta x_1 - \Delta x_1)\right]\right] \\ &\quad +(\Delta x_0 + \Delta x_1) \end{aligned} \tag{4.11}$$

where Δx_0 is the equivalent length of the zero probability section. Since the function described here asymptotes to zero for $x = -\infty$, it never completely reaches zero probability. The value at $x = \Delta x_0$ is arbitrarily set to $c = 0.1\% = 0.001$ of the function's maximum at $x = \Delta x_0 + \Delta x_1$. Δx_1 is user defined and determines the equation's parameter A' according to the following equation:

$$A' = \frac{1}{\pi\,\Delta x_1}\ \operatorname{arcosh}\left(\sqrt{1/c}\right) \tag{4.12}$$

To determine α, we need the total area under the probability density distribution given by (4.4) as a function of α:

$$\begin{aligned} P_1(\alpha) &= \int_{\Delta x_0 + \delta x_1}^{\Delta x_0 + \Delta x_1} p_1(x)\,dx \\ &= \alpha\ \tanh\left[A'\,\pi\,(\Delta x_1 - \delta x_1)\right] \quad : \quad -\Delta x_0 \leq \delta x_1 \leq \Delta x_1 \end{aligned} \tag{4.13}$$

4.3 Decreasing Section: sin – Approach

The density distribution starts out with a local maximum and decreases to zero for $\Delta x_0 + \Delta x_1 + \Delta x_2$. The gradient at the intersection with the abscissa is negative. The probability density, probability and inverse probability distribution are given in equations (4.14), (4.15) and (4.16), respectively. The parameter δx_2 is introduced to offset the termination of the decreasing probability density distribution.

For $\Delta x_0 + \Delta x_1 \leq x \leq \Delta x_0 + \Delta x_1 + \Delta x_2$:

$$p_2(x) = \alpha\,A'\,\pi\ \sin[B'\,\pi\,(x - (\Delta x_0 + \Delta x_1 - \Delta x_2))] \tag{4.14}$$

$$\begin{aligned} P_2(x) &= 1 + \alpha\frac{A'}{B'} \cdot \Big\{ \cos\left[B'\,\pi\,(\Delta x_2 + \delta x_2)\right] \\ &\quad - \cos[B'\,\pi\,(x - (\Delta x_0 + \Delta x_1 - \Delta x_2))]\Big\} \end{aligned} \tag{4.15}$$

For $P_2(\Delta x_0 + \Delta x_1) \leq P_2(x) \leq 1$:

$$\begin{aligned} x &= \frac{1}{B'\,\pi} \arccos\left[\cos\left[B'\,\pi\,(\Delta x_2 + \delta x_2)\right] - \frac{B'}{A'}\left(\frac{P_2 - 1}{\alpha}\right)\right] \\ &\quad +(\Delta x_0 + \Delta x_1 - \Delta x_2) \end{aligned} \tag{4.16}$$

where Δx_0 is the length of the zero probability section. Δx_1 is the section length from the function's intersection with the abscissa to its maximum.

Δx_2 is the section length from the function's maximum until return to zero probability density. The parameter B' is calculated according to the following equation:

$$B' = \frac{1}{2\,\Delta x_2} \tag{4.17}$$

The area enclosed by the probability density equation (4.14) and the abscissa is calculated as follows, where $\delta x_2 \geq 0$:

$$\begin{aligned} P_2(\alpha) &= \int_{\Delta x_0 + \Delta x_1}^{\Delta x_0 + \Delta x_1 + \delta x_2} p_2(x)\,dx \\ &= \begin{cases} -\alpha\,\frac{A'}{B'}\,\cos\left[B'\,\pi\,(\Delta x_2 + \delta x_2)\right] & : \quad 0 \leq \delta x_2 < \Delta x_2 \\ \alpha\,\frac{A'}{B'} & : \quad \delta x_2 \geq \Delta x_2 \end{cases} \end{aligned} \tag{4.18}$$

4.4 Decreasing Section: $1/\cosh^2$ – Approach

This decreasing probability density distribution based on $1/\cosh^2$ starts out with a local maximum and asymptotes to zero for increasing values of x. The variable c defines the probability value at $\Delta x_0 + \Delta x_1 + \Delta x_2$. The probability density, probability and inverse probability distribution are given in equations (4.19), (4.20) and (4.21) respectively. As in the $\sin$–approach, we introduce δx_2 to offset the termination of the decreasing probability density distribution.

For $\Delta x_0 + \Delta x_1 \leq x < \infty$:

$$p_2(x) = \frac{\alpha\, A'\, \pi}{\cosh^2\left[B'\,\pi\,(x - (\Delta x_0 + \Delta x_1))\right]} \tag{4.19}$$

$$\begin{aligned} P_2(x) &= 1 + \alpha \frac{A'}{B'} \cdot \Big\{ \tanh[B'\,\pi\,(x - (\Delta x_0 + \Delta x_1))] \\ &\quad - \tanh\left[B'\,\pi\,\delta x_2\right] \Big\} \end{aligned} \tag{4.20}$$

For $P_2(\Delta x_0 + \Delta x_1) \leq P_2(x) < 1$:

$$\begin{aligned} x &= \frac{1}{B'\,\pi}\ \mathrm{artanh}\left[\frac{B'}{A'}\left(\frac{P_2 - 1}{\alpha}\right) + \tanh\left[B'\,\pi\,\delta x_2\right]\right] \\ &\quad + (\Delta x_0 + \Delta x_1) \end{aligned} \tag{4.21}$$

where Δx_0 is the equivalent length of the zero probability section. Since the function described here asymptotes to zero for $x = +\infty$, it never completely reaches zero probability. The value at $x = \Delta x_0 + \Delta x_1 + \Delta x_2$ is arbitrarily set to $c = 0.001$ of the function's maximum at $x = \Delta x_0 + \Delta x_1$.

Δx_2 is user defined and determines the equation's parameter B' according to:

$$B' = \frac{1}{\pi\,\Delta x_2}\ \mathrm{arcosh}\left(\sqrt{1/c}\right) \tag{4.22}$$

The area enclosed by the probability density (4.19) and the abscissa is calculated as follows, where $\delta x_2 \geq 0$.

$$\begin{aligned} P_2(\alpha) &= \int_{\Delta x_0 + \Delta x_1}^{\Delta x_0 + \Delta x_1 + \delta x_2} p_2(x)\, dx \\ &= \alpha\, \frac{A'}{B'}\ \tanh\left[B'\,\pi\,\delta x_2\right] \quad : \quad \delta x_2 \geq 0 \end{aligned} \tag{4.23}$$

Table 4.1: Summary of equations required for the determination of the parameter α.

Approach	*Scaling Parameter*	*Increasing Probability Denisty Distribution*
sin	$A' = \frac{1}{2\,\Delta x_1}$	$P_1(\alpha) = \begin{cases} \alpha & : \quad \delta x_1 \leq 0 \\ \alpha\,\cos\left[A'\,\pi\,\delta x_1\right] & : \quad 0 < \delta x_1 \leq \Delta x_1 \end{cases}$
$1/\cosh^2$	$A' = \frac{1}{\pi\,\Delta x_1}\,\operatorname{arcosh}\left(\sqrt{1/c}\right)$	$P_1(\alpha) = \alpha\,\tanh\left[A'\,\pi\,(\Delta x_1 - \delta x_1)\right] \quad : \quad -\Delta x_0 \leq \delta x_1 \leq \Delta x_1$
Approach		*Decreasing Probability Denisty Distribution*
sin	$B' = \frac{1}{2\,\Delta x_2}$	$P_2(\alpha) = \begin{cases} -\alpha\,\frac{A'}{B'}\,\cos\left[B'\,\pi\,(\Delta x_2 + \delta x_2)\right] & : \quad 0 \leq \delta x_2 < \Delta x_2 \\ \alpha\,\frac{A'}{B'} & : \quad \delta x_2 \geq \Delta x_2 \end{cases}$
$1/\cosh^2$	$B' = \frac{1}{\pi\,\Delta x_2}\,\operatorname{arcosh}\left(\sqrt{1/c}\right)$	$P_2(\alpha) = \alpha\,\frac{A'}{B'}\,\tanh\left[B'\,\pi\,\delta x_2\right] \quad : \quad \delta x_2 \geq 0$

Chapter 5

MLI Model History

When the very first version of the models for MLI debris were developed, only limited information was available which could be used to derive relevant parameters. Information which could be drawn upon mainly consisted of literature discussing ground tests of the degradation process of commonly used MLI material and some knowledge of MLI configurations. All other information such as fragment size, release velocity and direction as well as deterioration related ejection rate was either derived by combining information from different sources or by making plausible initial assumptions. The benchmark for the models were the observations of high area-to-mass ratio objects in the GEO region by Schildknecht et al. (2004).

The fundamentals for the MLI models were initially layed out in a student research paper (Flegel 2006). Two mechanisms for the potential release of MLI as debris were identified for which models were created. One model simulated the disintegration of MLI during fragmentation events while another took into account an aging related process in which low numbers of MLI would separate from the parent object in a continuous process. The initial model check consisted of comparing simulated object orbit parameters and number of objects larger than 10 cm to observation results. This comparison did not employ any model for simulating the actual measuring telescope which had yielded the observation data. Krag et al. (2008) conducted the first validation by using ESA's tool PROOF-2005 to simulate the observation campaigns which had been performed by AIUB with ESA's Space Debris Telescope (SDT). *PROOF* is ESA's **P**rogram for **R**adar and **O**ptical **O**bservation **F**orecasting. Detailed parameters for the performance of the employed system are fed into a so called 'optical performance model.' This model is applied to the simulated debris population of MLI and

calculates which objects could have been detected by the telescope on a case-by-case basis. Results showed that for 2005, the modeled GEO detections came within 10 % of the uncorrelated measured detections. A significant drawback of the model was that educated guesses had to be used to define the shape and number of MLI debris released during a spacecraft fragmentation. This approach was made necessary because no data was available at the time which could be used to derive this important information.

The initial MLI models were changed in some aspects when they were integrated into the MASTER-2009 software. For the first time, fragment size distribution data was available from ground tests which had been performed at Kyushu University, Japan (Murakami 2008). The user defined fragment number was therefore replaced by a model based on these tests. In this model version, the fragment size probability distribution was identical for all events. As the satellite mock-ups from the tests had a cube shape with a side length of 20 cm, fragment sizes always remained below this threshold. A remediation of this will be discussed in Chapter 7.3. Other changes were made to the continuous source model. In the new model, independent probability distributions were introduced for the time of release of cover layer and reflector layer MLI. For validation, the modeled population was compared to observation data from ESA's SDT from the years 2004 to 2007.

The current chapter details the MLI models as implemented into MASTER-2009 which is the state of the last release of the model. Section 5.1 presents general information on the use and application of MLI on spacecraft. The tumbling motion and deformation of MLI debris effect the net acceleration due to solar radiation pressure. Section 5.2 discusses how this is taken into account in the modeling. Sections 5.3 and 5.4 describe the fragmentation and continuous source models respectively. Large parts of the following chapter have been published in Flegel et al. (2011a) and Flegel et al. (2011b).

5.1 MASTER-2009 MLI Applications on Spacecraft

The following applications of MLI are taken into account in the MASTER-2009 model:

1. Thermal insulation on the outside of the main body of three-axis stabilized spacecraft.
2. MLI covering radio-frequency antennae.

The total area of MLI used for these two applications must be estimated as well as the area-loading of the materials used. The total area represents the upper limit in total debris area which is available to the models. The area-loading is key to deriving realistic area-to-mass ratios of MLI debris objects. Both applications are treated separately in the following.

5.1.1 MLI on Satellite Buses

In the current work, the term *satellite bus* is used to describe the spacecraft structure without protrusions such as extended solar arrays. It is assumed that all three-axis stabilized satellites are roughly box shaped. The dimensions in length, height and depth are extracted from the **D**atabase and **I**nformation **S**ystem **C**haracteri-sing **O**bjects in **S**pace (DISCOS) which is maintained and kindly made available by the European Space Operations Centre (2010). A simple dependency for the ratio of surface area of the satellite bus ($A_{\text{satellite bus}}$) vs. satellite beginning-of-life mass ($m_{\text{satellite}}$) was derived based on data from DISCOS (Flegel 2006):

$$\frac{A_{\text{satellite bus}}}{m_{\text{satellite}}} = 0.5 \left(0.01 + \frac{20}{m_{\text{satellite}} + 2000} \right) \tag{5.1}$$

As an example, according to Stadermann et al. (1997) and Wright et al. (1995), much of the European Retrievable Carrier (EuReCa), was covered with an MLI blanket with a total of 22 layers (see Section 2.2 for details). The bus structure had dimensions of $4.6 \times 2.6\,\text{m}$ (ESA 2008) and the spacecraft mass at launch was 4490 kg. Due to the box shape geometry, the MLI covered surface can be estimated to $61.36\,\text{m}^2$. The two radiators and some boxes on the underside were not covered by MLI. The radiators were placed on the surfaces from which the solar arrays protruded and covered almost the entire side (Figure 5.1). The remaining surface area which could be covered by MLI would be roughly $37.44\,\text{m}^2$. The

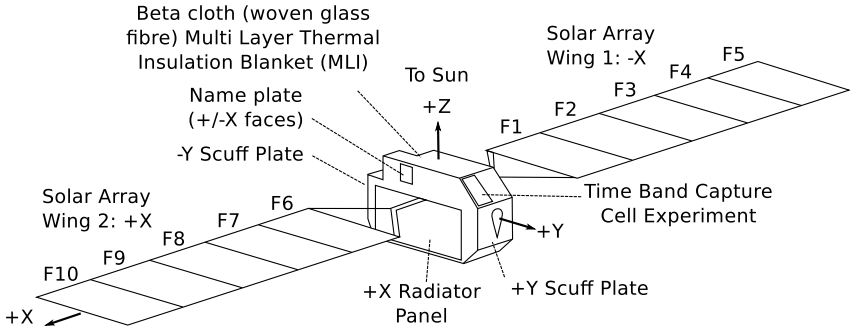

Figure 5.1: Sketch of European Retrievable Carrier (EuReCa) showing location of radiator panels reproduced from ESA (2008)

area could also be estimated by using other values which were given by ESA (2008). The total exposed surface area was allegedly about $140\,\mathrm{m}^2$, including $99\,\mathrm{m}^2$ of solar array area. Subtracting $99\,\mathrm{m}^2$ from the $140\,\mathrm{m}^2$ leaves $41\,\mathrm{m}^2$ for the satellite bus. Removing $4.6 \times 2\,\mathrm{m}$ twice for the radiator panels and another square meter for boxes on the underside which were not covered by MLI, the remaining area is slightly more than $20\,\mathrm{m}^2$. This is substantially less than the previously estimated $37.44\,\mathrm{m}^2$. Using Equation 5.1, the estimated total surface area for MLI is $29.37\,\mathrm{m}^2$. The estimated value is in between the values derived from online sources.

The total number of layers for the MASTER-2009 model was set to 12 for a conservative model. Of these layers, the outer and inner most layer are the *cover layers* while the 10 remaining intermediate layers are so called *reflector layers*. A mean thickness of the outer and inner layers of 5 mil[1] is selected. The lowest area loading advertised by Sheldahl (Sheldahl 2006) was 0.25 mil. This was assumed to be the lowest as well as the most common thickness of the inner reflector layers. The material densities for all layers range from $1.4\,\mathrm{g/cm}^3$ to $2.2\ \mathrm{g/cm}^3$ depending on the material used. Spacer material which is often used to separate the individual layers was not taken into account here.

[1] 1 mil = 0.001 inch $\approx 25.4\,\mu$m

5.1.2 Radio Frequency (RF) Antennae Sun Shields

Performance of RF-antennae is inhibited by signal noise which may be introduced through different sources. Sun shields are used to decrease noise by preventing buildup of static charge and to shield the antennae from direct solar irradiation. The number of layers used in this model is set to one.

However, not all satellites use parabolic antennae. Iridium satellites as well as the GPS, GLONASS and Globalstar satellites were assumed to have no RF Sun shields. Due to the high altitude of GEO satellites, it was assumed that parabolic antennae with Sun shields were used on all such satellites for communication with ground stations. In contrast, the LEO satellites are low enough for parabolic antennae are not to be necessarily required. It was arbitrarily assumed that only half of the LEO satellites employ parabolic antennae with Sun shields. For the model, the diameter of all RF-antennae is set to 2.4 m. This is about the size of the C- and Ku-band antennae of the Boeing built Intelsat IS-22, IS-21 and IS-27 of which four antennae with diameters of 2.25 m each are used (Boeing 2013).

5.1.3 Area Loading

The area loading is defined through the material and the layer thickness used for the foils. It can be expressed in mass per area. For objects with low area loadings such as HAMR objects, it is easier to work with the inverse factor, the area-to-mass ratio. Independent probability distributions for the cover layer MLI (one outer and one inner layer), the intermediate reflector layers and RF-antenna Sun shield foils were created. The material area loading was inferred from vendor information (Sheldahl 2009) and the NASA Multilayer Insulation Material Guidelines (Finckenor and Dooling 1999). The chosen distributions with limiting and mean area loading factors are given in Table 5.1. A graphic description of the variables can be found in Figure 4.2.

5.2 Effective Area

MLI fragments can have different shapes. The orbit evolution depends on an object's orientation and cross section with respect to the incident radiation (see Chapter 6). The orbit propagation for these models assumes all fragments to be spheres while the models produce fragments with more plate like features.

Table 5.1: MASTER-2009 area loading parameters.

Distribution	Area Loading $(A/m)_{\text{loading}}$ / m^2/kg		
Parameter	*Cover*	*Reflector*	*RF-Antennae*
c	0.0001	0.001	0.001
Approach Onset	sin	$1/\cosh^2$	sin
Δx_0	0.3	50	0.1
$\Delta x_0 + \delta x_1$	2	60	0.3
$\Delta x_0 + \Delta x_1$	6	110	3
Approach End	$1/\cosh^2$	$1/\cosh^2$	$1/\cosh^2$
$\Delta x_0 + \Delta x_1 + \delta x_2$	15	111	15
$\Delta x_0 + \Delta x_1 + \Delta x_2$	15	115	15

To remediate this initial incompatibility, it is assumed that a tumbling motion allows a time averaged mean cross section to be derived from the object's initial area and deformation relative to an initially flat plate. As a solution to this issue, the current section introduces a simple equation for the estimation of this *effective* area:

$$A_{\text{eff}} = A_{\text{flat}} \cdot F_{\text{reflectivity}} \cdot F_{\text{deformation}} \cdot F_{\text{tumbling}} \tag{5.2}$$

Herein, the area of a flat plate A_{flat} is multiplied by reduction factors F for the three main influencing parameters. In the following, estimations for the deformation $F_{\text{deformation}}$, the tumbling motion F_{tumbling} and the reflectivity $F_{\text{reflectivity}}$ are given. The relations presented in the current chapter were applied in the MASTER-2009 model. A revision of the approach is discussed in Chapter 7.2.

5.2.1 Deformation

A core question is how much a single layer of MLI may be expected to deform at all. Research revealed only two basic modes of deformation. Mode one is given by the observed fragments from the ground tests. Here, only slight crumpling was found in most cases. The second mode was observed during Hubble Space Telescope (HST) servicing missions. The top layer of some insulation blankets

partially delaminated and curled upwards (Dever et al. 1998). This curling behavior may be specific to the aluminum coated FEP material exposed to the LEO space environment. Pisacane and Moore (1994) states that Teflon-based materials show a significant change in optical properties after a certain dose of electrons/protons at certain energies has been absorbed. While atomic oxygen is known to be highly corrosive to some materials, it is stated that loss of material strength leading to disintegration appears most prominently with Kapton and Mylar. These findings are supported by more recent on-orbit studies where 38 polymers and pyrolytic graphites were tested on the ISS. The rate of deterioration varied substantially among materials (Banks et al. 2011). As the cause for the curling behavior observed on HST service missions could not be pinpointed, it was decided to adopt this mode as the strongest deformation effect independently of the material and orbit. The smallest estimated projected area due to curling was roughly estimated to 0.2 times the original area. $F_{\text{deformation}}$ is a value uniformly distributed between 0.2 (curling) and one (no deformation). It is expressed as a function of the uniformly distributed real number κ:

$$F_{\text{deformation}} = (F_{\text{defo,min}} - F_{\text{defo,max}}) \cdot \kappa_{\text{defo}} + F_{\text{defo,max}} \tag{5.3}$$

$$\begin{array}{rcll} F_{\text{defo,min}} & = & 0.2 & \qquad \kappa_{\text{defo}} \in [0,1] \\ F_{\text{defo,max}} & = & 1 & \end{array}$$

5.2.2 Tumbling

Tumbling can reduce the time averaged illuminated area which decreases the *effective* area. The maximum possible value is one. For plate like objects, this occurs if the fragment is always oriented perpendicular to the Sun. For spherical objects, rotation has no effect on the illuminated area. For MASTER-2009, the lowest value was assumed to be $1/2$. This value results from a flat plate spinning at equal angular rates about two orthogonal axes. For the model, it is assumed that the maximum deformation into a curled up tube is close to a sphere where tumbling has no effect. This is a drastic over-simplification but is used nevertheless due to the high uncertainty in the basic assumptions made. F_{tumbling} is a uniform distribution between the highest value, 'one,' which is independent of the object's shape, and the lowest value which changes according to the object's shape i.e. The lowest value for a flat plate is set to $1/2$, for the maximum curling shape, the lower value is set to 1. For intermediate deformations, the lower value

changes linearly with the deformation factor. It is expressed as a function of the uniformly distributed real number κ:

$$F_{\text{tumbling}} = F_{\text{tumb,max}} - \kappa_{\text{defo}} \cdot \kappa_{\text{tumb}} \left(F_{\text{tumb,max}} - F_{\text{tumb,min}}\right) \tag{5.4}$$

$$\begin{array}{rcll} F_{\text{tumb,min}} & = & 0.5 & \kappa_{\text{defo}} \in [0,1] \\ F_{\text{tumb,max}} & = & 1.0 & \kappa_{\text{tumb}} \in [0,1] \end{array}$$

If the object is a tube, tumbling should have no effect. In this case, $\kappa_{\text{defo}} = 0$ and F_{tumbling} becomes $F_{\text{tumb,max}}$. For a plate like object, $\kappa_{\text{defo}} = 1$ and tumbling can lead to any value between full reduction ($F_{\text{tumbling}} = F_{\text{tumb,min}}$) and no reduction in case of a Sun-oriented fragment ($F_{\text{tumbling}} = F_{\text{tumb,max}}$).

5.2.3 Reflectivity

For MASTER-2009, the reflectivity coefficient C_R was fixed at 1.3. The effect of reflectivity lower than 'one' was modeled by reducing the effective area by a factor which is the reflectivity of the material. The reflectivity of aluminum at room temperature for visible light was chosen with an approximated constant value of 0.95 = $F_{\text{reflectivity}}$. This is a very crude first assumption which was later revised by Fischer (2011).

5.3 MASTER-2009 MLI Fragmentation Model

The data flow within the MLI fragmentation model is depicted in Figure 5.2. Given data is shown on the left while derived values are presented on the right.

5.3.1 Total MLI Area

The sum of the area of all fragments created by the MLI fragmentation model is equal to 5 % of the total area of insulation material as given by Equation 5.1 and multiplied by the number of available cover and reflector layers. Ground tests evaluated by Murakami (2008) indicate that a large amount of MLI area may be 'hidden' in so called *complex fragments*. Complex fragments may consist of completely or partially intact blankets of MLI, in which several layers of insulation are interconnected (i.e. through seams at the edges). For MASTER-2009, modeling of these fragments was not included. Their equivalent mass is processed

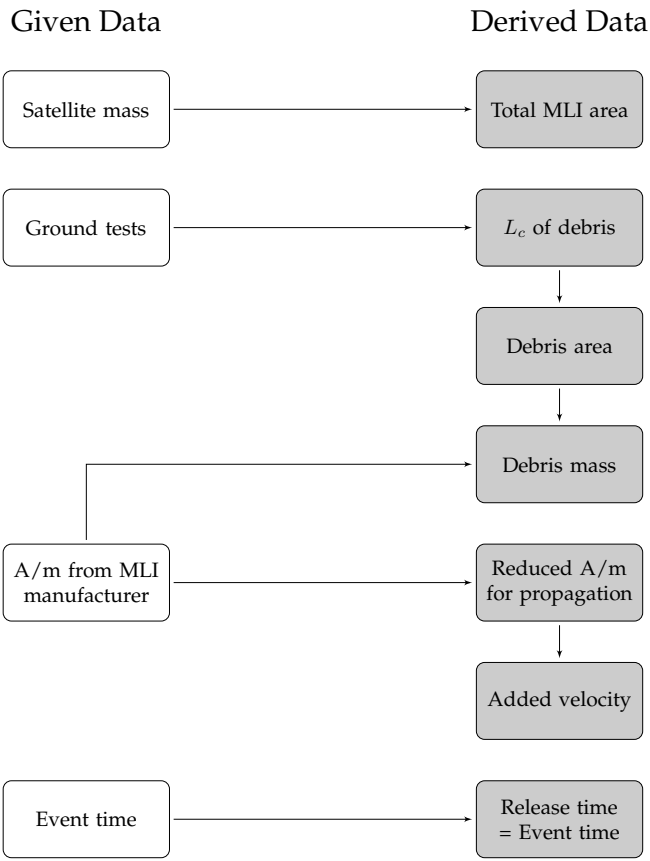

Figure 5.2: Structure of MLI fragmentation model.

along with the rest of the object by the modified NASA Breakup Model for standard fragmentations (Flegel et al. 2011a). For MASTER-2009, 10 reflector layers and two cover layers were simulated in fragmentations. Using Equation 5.1, the

total area of reflector-/cover-layer foil $A_{\mathrm{r/c}}$ is given by:

$$A_{\mathrm{r/c}} = n_{\mathrm{layers}} \cdot \left(1 - F_{\mathrm{complex}}\right) \cdot \left[0.5 \left(0.01 + \frac{20}{m_{\mathrm{satellite}} + 2000}\right) \cdot m_{\mathrm{satellite}}\right]$$

$$n_{\mathrm{layers}} = \begin{cases} 2 & : \text{ cover layers} \\ 10 & : \text{ reflector layers} \end{cases} \qquad F_{\mathrm{complex}} = 0.95 \tag{5.5}$$

5.3.2 Debris (Fragment) Characteristic Length

The MLI fragmentation model parameters were based upon two ground tests which were performed at Kyushu University, Japan, in cooperation with NASA's Orbital Debris Program Office (Murakami 2008). In both tests a cube shaped satellite mockup, was shot at. The impact energy was about 40 J/g in each test, leading to the complete fragmentation of the model. The size of the mockup was 20x20x20 cm, a solar panel approximately 20x20 cm was mounted flat to one side. All remaining sides were covered by six layers of MLI. In the test termed 'Shot F', the satellite was shot at from the side of the solar array, in 'Shot R', the projectile penetrated the satellite from the opposite side. In both cases, the impact was perpendicular to the surface. The characteristic length L_c of the fragments was derived using three orthogonal dimensions of the objects:

$$L_c = \frac{1}{3}\left(X + Y + Z\right) \tag{5.6}$$

For plates with complex shapes, X is the largest dimension and Y is the second largest dimension. For oblong plates X and Y are calculated from the length and width (Murakami 2008). The applied methods were the same as those which were used in analyzing the fragments from the SOCIT-4 tests. The data from the SOCIT-4 test results made up the basis for the small particle size regime of the NASA breakup model (Johnson et al. 2001). Figure 5.3 shows the reverse cumulated number of MLI fragments versus the characteristic length from the two ground tests. A mean fit of the two data curves is shown in Figure 5.4. The derived parameters of this distribution are given in Table 5.2. The major draw-back of the MASTER-2009 model implementation is that the distribution of characteristic lengths among the simulated fragments are applied to all spacecraft fragmentations equally. The size of the fragments produced by a satellite with a 4 m x 4 m x 5 m will therefore produce fragments of the same size as a satellite with a side length of just a few centimeters.

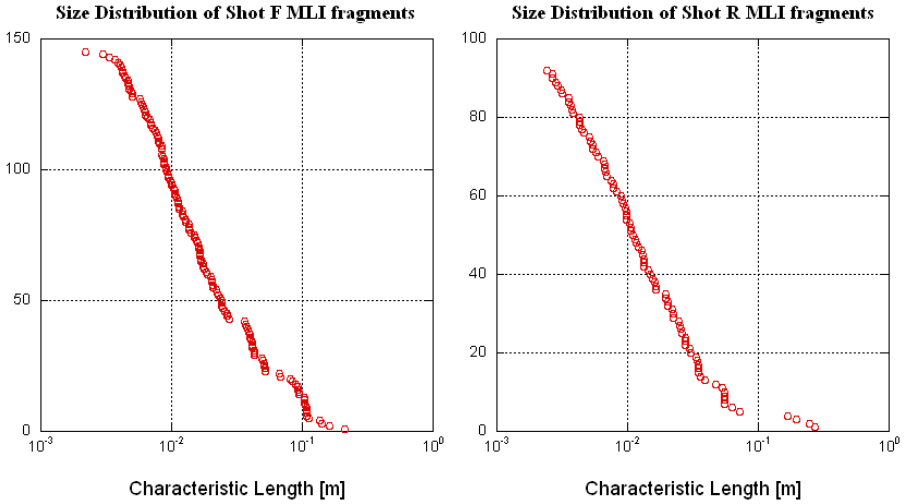

Figure 5.3: Characteristic length L_c of MLI fragments from ground tests at Kyushu University. In 'Shot F,' the satellite was shot at from the side of the solar array. In 'Shot R,' the satellite was shot at from the side opposite the solar array. The y-axis shows the total number of MLI fragments which are larger than the given characteristic length. Both plots were supplied by J. Murakami in personal communication (Murakami 2009).

5.3.3 Debris Fragment Area

The sum of the areas of all fragments must in the end be equal to the total available MLI area derived by Equation 5.5. Therefore, the actual area of the piece of MLI must be known within the model. So far, the only known parameter relating to the size is the characteristic length which takes into account 3-dimensional deformation. A relation must therefore be found between the characteristic length and the actual area of the MLI piece. One possibility is to assume initially that the true area of the fragment is close to the square of the characteristic length. Deviations from this assumption can then be accounted for by including a correction factor $F_{\text{conversion}}$:

$$A_{\text{flat}} = L_c^2 \cdot F_{\text{conversion}} \tag{5.7}$$

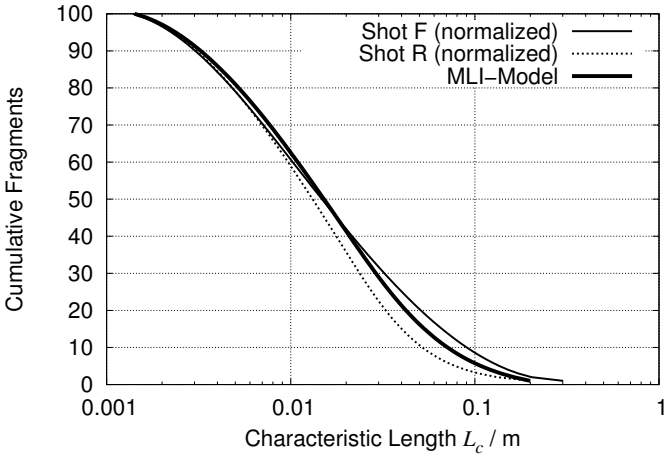

Figure 5.4: Derived fits for characteristic length of shots F and R and of the mean fit used in the MLI model.

The index *flat* indicates that the actual area of the smoothed out piece of MLI is meant and not the projected area of the 3-dimensionally deformed fragment. The area A_{flat} can be calculated if the area loading of the material and the object's mass are known:

$$A_{\text{flat}} = \left(\frac{A_{\text{flat}}}{m}\right) \cdot m \tag{5.8}$$

In the ground tests, the cover layers had a loading of $A_{\text{flat}}/m = 0.035\,\text{kg/m}^2$ and the reflector layers had a value of $0.008\,\text{kg/m}^2$. The mass was given in terms of mass vs. characteristic length plots. Combining equations 5.7 and 5.8 results in:

$$m = L_c^2 \cdot F_{\text{conversion}} \cdot \left(\frac{A_{\text{flat}}}{m}\right)^{-1} \tag{5.9}$$

This relation can now be fitted to the given data via the sought correction factor $F_{\text{conversion}}$. This value was found to be almost identical to one. This is a good indication for the applicability of the method which was used to derive the characteristic length of the fragments in the first place. Equation 5.7 thus simplifies

Table 5.2: MASTER-2009 MLI Fragmentation Model: Distribution parameters for characteristic length L_c. A graphic description of the variables can be found in Figure 4.2.

Distribution Parameter	*Characteristic Length L_c / $\log_{10}(m)$*
c	0.0001
Approach Onset	sin
Δx_0	-3
$\Delta x_0 + \delta x_1$	-3
$\Delta x_0 + \Delta x_1$	-1.7
Approach End	$1/\cosh^2$
$\Delta x_0 + \Delta x_1 + \delta x_2$	1.5
$\Delta x_0 + \Delta x_1 + \Delta x_2$	-0.7

to the term also applied in the model:

$$A_{\text{flat}} = L_c^2 \tag{5.10}$$

5.3.4 Debris Fragment Mass

Having established the area for each fragment, the object's mass is simply given by:

$$m = A_{\text{flat}} \cdot \left(\frac{A_{\text{flat}}}{m} \right)^{-1} \tag{5.11}$$

For each fragment, the area loading (A_{flat}/m) is precisely defined through the used material. For modeling purposes, this ratio is determined based on the probability distributions for different MLI types. The required values have been derived in the previous section and are presented in Table 5.1. At this stage, the characteristic length L_c, the mass m and the area of the smoothed out fragment A_{flat} are known.

5.3.5 Added Velocity

At the time of the model release, no data was known to the author explicitly detailing the velocity transferred to MLI debris during a fragmentation. In the initial attempt to simulate this process, the velocity distribution from the NASA-Breakup model was used.

5.3.6 Release Time

In the current MLI fragmentation model, MLI debris is only produced at the time of the fragmentation event. In reality, complex fragments are created which consist of several layers of MLI. These are in essence blankets which have lost some of their structural integrity. Such fragments may dissolve over time leading to 'post fragmentation delamination.' The MASTER-2009 MLI model does not taken this into account.

5.4 MASTER-2009 Continuous MLI Source Model

The continuous MLI debris source model tries to account for deterioration of MLI which can lead to slow disintegration of the thermal insulation whereby individual fragments are released. Satellites are designed for a specific operating environment and mission duration where ageing processes, especially of optical properties, are taken into account. The current model was based on the idea that material deterioration may accelerate quickly after mission end. Once the active part of the thermal control subsystem as well as the attitude control subsystem has been powered down, temperature gradients and amplitudes will increase. Thermal cycling is one effect known to degrade mechanical and optical properties of common MLI materials (ESA-ESTEC 2009).

Only the release of single layer debris is simulated. This is thought to occur when deterioration causes the insulating material to lose part of its structural integrity, making it susceptible to tearing. Detachment of interconnected layers or entire MLI blankets is not taken into account. Based on this premise, three stages are identified leading up to the release of MLI fragments:

1. tear initiation,
2. tear propagation and
3. foil separation.

This chapter gives only a brief overview of some important factors concerning these stages. For a detailed account, the reader is referred to Flegel (2006). **Tear initiation** occurs in regions of highest stress and is enhanced by material degradation (de Groh and Smith 1997). Regions of increased stress may be locations where the MLI blankets are attached to the spacecraft structure, places in which the layers are bonded to one another (i.e. by being sown together), in corners or around cutouts. This was also observed for instance during inspections of Teflon® FEP returned from the Hubble Space Telescope from the first and second service missions (Dever et al. 1998). Tearing can be started by external or internal forces. External forces are incurred for instance during spacecraft maneuvering, during launch or when particles impact the insulation. MASTER-2009's intrinsic calculation of the flux vs. ballistic limit reveals that for the year 2009 on the order of 440 particles could penetrate one square meter of a wall with a thickness of 100 μm on a LEO Sun-synchronous orbit and about 140 on a GEO orbit. Pre-launch damaging of the MLI could also lead to detaching of MLI during or after launch, if gone undetected. The Cassini Huygens launch, for instance, was postponed when pre-launch tests on the launch pad revealed ruptured MLI (ESA 1997). The Venus Express launch was also delayed when pieces of MLI from the Fregat upper stage were found in the rocket fairing and on the Venus Express spacecraft (ESA 2005). Thermal cycling is an important internal force which can cause tear initiation (de Groh et al. 1998, Townsend et al. 1998). Samples of Aluminum-FEP which were retrieved from the Hubble Space Telescope, exhibited cracks near the seams of the blankets (Dever et al. 1998). Similar to tear initiation, **tear propagation** requires the presence of stresses which can be caused either by external or internal forces. Cyclic loading, for instance, through thermal cycles can weaken a material and lead to crack propagation even if the material's ultimate tensile strength is not exceeded. Once a crack has exceeded a critical, material and load type dependent length, the remaining material will fail quickly. **L**inear **E**lastic **F**racture **M**echanisms (LEFM) is one of the most important theories on crack propagation for rigid materials describing this effect. The major difference between rigid materials and foils is that foils will not crinkle under pressure loads. Differently from tear initiation and tear propagation,

internal forces dissappear once the foil is held in place at only a few remaining points. **Foil separation** can therefore only be induced through external forces.

The data flow of the continuous MLI debris source model is similar to that of the fragmentation model (see Figure 5.5). The most prominent differences are the time of release of the fragments and the data underlying the derivation of the characteristic fragment length.

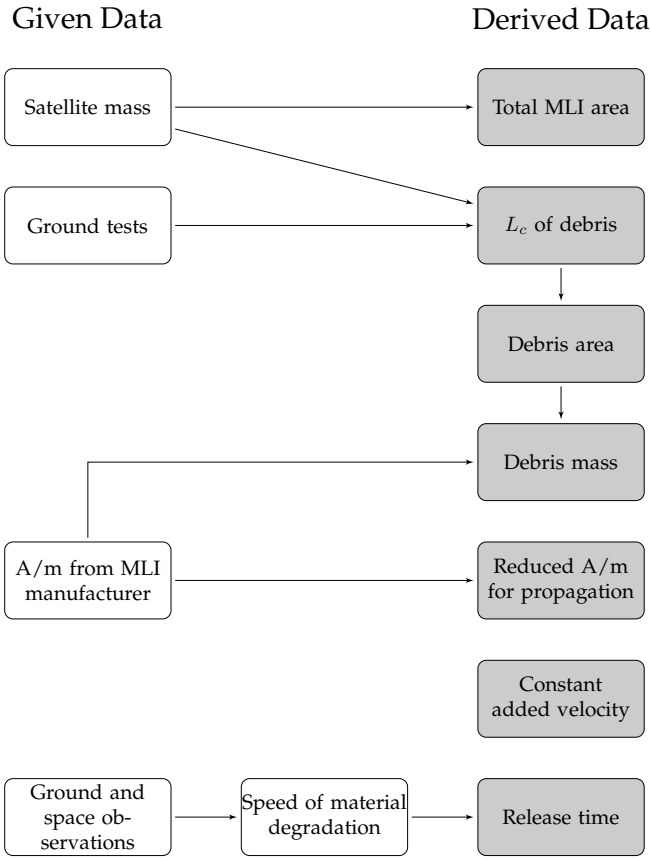

Figure 5.5: Structure of MLI continuous source model.

5.4.1 Debris Object Characteristic Length

No ground tests were known which detailed possible fragment sizes resulting from the mechanism under discussion. The characteristic length was therefore estimated based on plausible assumptions alone. A differentiation was made between MLI used on the satellite bus and RF-antennae sun shields. In both cases, generic distributions were defined in the interval [0..1]. The resulting value was then multiplied by the derived maximum value for L_c for each parent object. MASTER-2009 parameters of this distribution are given in Table 5.3.

For **satellite buses**, the longest possible characteristic length is given through the available coherent area. The definition of this area is based on equation 5.1. The rationale behind choosing this value arises from the knowledge that most surfaces of satellite buses are interrupted by protrusions such as sensors or solar panels. Based on the hypothesis that crack propagation is related to areas with high stress, it is assumed that tears will continue along the MLI blanket edges and travel to the nearest protruding instrument. The approximated distance between a protrusion and an MLI edge is 15 % of the satellite side length. The minimum and maximum values are set to 0 % and 100 % of a satellite side with the value of highest probability being 15 %. The probability density distribution is completely defined through the $1/\cosh^2$ approach.

Also for **RF-antennae sun shields**, regions of highest stress will be the edges, where the foil is fastened to the structure. The shields differ from MLI on the satellite bus in that they are often installed tautly over the antennae, increasing the overall level of stress in the material. The largest pieces of debris are assumed to be produced in the case that a crack propagates not along the edge, but across the center region to the opposite side. This could lead to pieces with sizes on the order of half of the area of the sun shield. The minimum, mean and maximum values for the probability distribution for characteristic lengths were set to 0 m, 0.9 m and 2 m. The standard diameter of an RF-antennae was found to be 2.4 m (see Section 5.1.2). Again, the $1/\cosh^2$ approach is chosen for the probability density distribution.

Table 5.3: MASTER-2009 Continuous MLI Source: Distribution parameters for characteristic length L_c. A graphic description of the variables can be found in Figure 4.2.

Distribution	Characteristic Length L_c		
Parameter	*Cover*	*Reflector*	*RF-Antenna*
Unit	%	%	m
c	0.001	0.001	0.001
Approach Onset	$1/\cosh^2$	$1/\cosh^2$	$1/\cosh^2$
Δx_0	0	0	0
$\Delta x_0 + \delta x_1$	0	0	0
$\Delta x_0 + \Delta x_1$	0.15	0.15	0.9
Approach End	$1/\cosh^2$	$1/\cosh^2$	$1/\cosh^2$
$\Delta x_0 + \Delta x_1 + \delta x_2$	1	1	2.06
$\Delta x_0 + \Delta x_1 + \Delta x_2$	1	1	2.06

5.4.2 Total MLI Area, Debris Object Area and Debris Object Mass

The total MLI area processed by the model is given by Equation 5.5. The area of each debris object is estimated based on the characteristic length using Equation 5.10. The mass of the individual objects is then obtained using Equation 5.11.

5.4.3 Added Velocity

The forces exerted on MLI are small compared to the fragmentation mechanism (Flegel 2006). In NASA's History of On-Orbit Fragmentations (Johnson et al. 2008), small release velocities for debris are documented. Whenever small numbers of trackable objects are observed to drift away from a parent object, these events are termed 'anomalous.' For the continuous debris source MLI model, a constant delta velocity of one meter per second is assigned to all fragments.

The direction is assigned in such a way that a uniform distribution is achieved in Cartesian coordinates. The equation proposed by Oswald (2001) is used. The

direction of the release velocity is defined in spherical coordinates by right ascension and declination. In right ascension, a value uniformly distributed between 0 and $2\,\pi$ can be used. The declination δ must take into account the increasing density of the meridians around the poles. A value κ is therefore introduced which maps a uniform distribution between 0 and 1 to a non-uniform distribution between $-\pi$ and $+\pi$ for δ:

$$\begin{aligned} \kappa_{\text{sph}} &= \frac{\arccos\left(1-2\kappa\right)}{\pi} \qquad ; 0 \leq \kappa \leq 1 \\ \delta &= \pi \cdot \kappa_{\text{sph}} - \frac{\pi}{2} \end{aligned} \tag{5.12}$$

5.4.4 Release Time

The continuous MLI debris source model is based on the premise that mechanical material properties degrade to the point where given external or internal forces finally cause parts of MLI to detach from the parent object. The time of 'release' therefore basically depends on the rate of deterioration and the acting forces.

Individual distributions were defined for the outer two layers of MLI and RF-antenna sun shields. The concept used to estimate the key parameters of the probability distribution starts out with the hypothesis that in the event that all MLI on a spacecraft were perfectly homogeneous, that all material properties along with the rate of deterioration and all external and internal forces and stresses were identical, that all of the MLI would fail simultaneously. Differences in the initial material properties, the rate of deterioration and acting forces cause different parts of MLI to fail at different times. Estimating the effect that these differences have on the time of release then becomes the key to obtaining realistic probability distributions for the time of release. In the first model, values were estimated using educated guesses (Flegel 2006). In total, such effects were assumed to cause a difference of 55 years between delamination of the first and last fragment from the top most layer of MLI on a spacecraft bus.

Influences which affect thermal insulation material properties were researched extensively. Onset of delamination was finally estimated using equivalent solar hours (ESH). This was based in part on findings from ground tests, but mostly through analysis of results from Hubble-Space Telescope (HST) service missions.

During the second servicing mission, the thermal insulation system was found to have cracked severely. At this time, the material had absorbed approximately 19,300 ESH. By the third servicing mission, the new thermal protection had been exposed to about 13,600 ESH and the amount of cracking was far less. A single side of a three axis stabilized satellite in GEO accumulates similar amounts of ESH after about six to seven years. Of course the space environment in GEO is completely different from that in LEO. The corrosive atomic oxygen which is abundant in the vicinity of the HST but does not exist in GEO is but one example. This value was nevertheless used as an initial estimate of the order of magnitude in which deterioration could lead to release of MLI fragments. The values chosen for MASTER-2009 are given in Table 5.4.

Table 5.4: MASTER-2009 Continuous MLI Source: Distribution parameters for release time. A graphic description of the variables can be found in Figure 4.2.

Distribution	Time of Release		
Parameter	*Cover*	*Reflector*	*RF-Antennae*
Unit	years	years	years
c	0.001	0.001	0.001
Approach Onset	$1/\cosh^2$	$1/\cosh^2$	$1/\cosh^2$
Δx_0	0	0	0
$\Delta x_0 + \delta x_1$	7	14	15
$\Delta x_0 + \Delta x_1$	21	36	25
Approach End	$1/\cosh^2$	$1/\cosh^2$	$1/\cosh^2$
$\Delta x_0 + \Delta x_1 + \delta x_2$	200	200	50
$\Delta x_0 + \Delta x_1 + \Delta x_2$	100	100	100

5.5 MASTER-2009 MLI Population

The model validation was performed by comparing *PROOF* simulations of the 2004 to 2007 ESA-SDT campaigns to the actual detections. Results were filtered so that only detections with magnitudes between +14 and +20 were taken into account. The limit of +20 magnitude is given by the instrument's sensitivity

which starts to tail off around +19 to +20. The upper value of +14 magnitude was chosen for the validation of all GEO space debris objects of the *MASTER* population. Observations brighter than +14 magnitude can usually be attributed to spacecraft or rocket bodies. Since the comparison was aimed primarily at validating the debris source models, only objects fainter than +14 magnitude were looked at. This threshold is reviewed in Chapter 8 as publications show that objects which can not be correlated with any objects in the Satellite Situation Report exist at all visible magnitudes (Schildknecht et al. 2010). The validation result is shown in Table 5.5. For the chosen magnitude range, the simulated data lies within 6 % of the measurements for all years prior to 2007. For 2007 the deviation is 26 %. A steady increase in the detected objects is seen for the years 2004 to 2006. From 2006 to 2007, the number of detections drops by 42 %. This drop is also reflected in the simulation but at a lower rate. In the simulations, MLI contributes up to 45 % of the detected objects.

Table 5.5: Number of objects with magnitudes between +14 and +20 magnitude. Comparison of simulation with ESA-SDT measurements taken from Flegel et al. (2011b).

Data Source	2004	2005	2006	2007
ESA-SDT (Total: +14 - +20 magnitude)	464	625	726	422
PROOF- (Total: +14 - +20 magnitude)	465	661	702	533
PROOF- (MLI only: +14 - +20 magnitude)	182	177	319	229
PROOF- (MLI only: all magnitudes)	215	321	364	284

Table 5.6 shows the dominance of MLI fragments from the continuous debris source model in the 10 cm population for the reference epoch of May 2009. Figures 5.6 compare the ESA-SDT detections for the years 2004 to 2007 to the *PROOF* simulations. The term *tracklets* in the figures presenting the ESA-SDT measurements is synonymous to the term *detections* in the *PROOF* results. A tracklet describes a short arc of the orbit of an observed object. Tracklets are typically constructed from consecutive observations of an object. One object may produce multiple tracklets if it is observed at different times. The figures show the inclination versus right ascension of ascending node (*RAAN*) distribution of the objects. Third body perturbations from the Sun and Moon cause the inclination

Table 5.6: Simulated number of in-orbit objects for May 1st, 2009 (Flegel et al. 2011b).

Size range	Fragmentation debris	Continuous Source objects
$> 1\,\mu$m	16,908	5,333
> 1 mm	16,908	5,333
> 1 cm	10,457	5,333
> 10 cm	831	4,919

of GSO objects with area-to-mass ratios below about 1 m^2/kg to increase to about 16 degrees and to decrease again to 0 degrees before restarting the cycle. In the same time frame, the *RAAN* decreases from around +180 degrees at 0 degrees inclination to about -180 degrees. The time period is 53 years. HAMR objects are subjected to the same cycle, but amplified by radiation pressure. This leads to larger inclinations and a reduced cycle period. In addition HAMR objects from the continuous source model especially seem to exhibit variations in this behavior, causing them to occupy areas in the inclination vs. *RAAN* representation where other objects are much less abundant. These areas include non-zero inclinations around 180 degrees *RAAN* and inclinations below 15 degrees around 0 degrees *RAAN*. An explanation of this behaviour is given in Section 7.4.

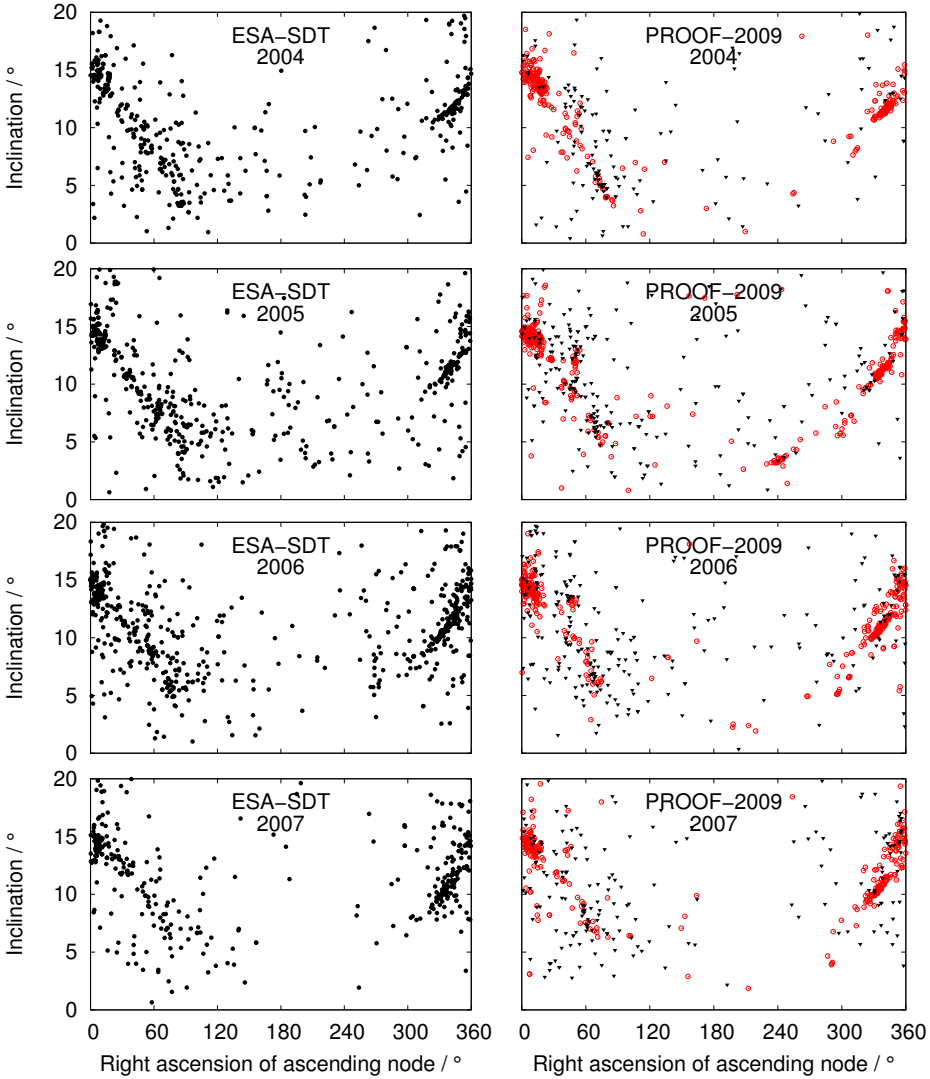

Figure 5.6: Tracklets from ESA-SDT surveys (left). *PROOF* detections for MASTER-2009 MLI population (right). The red circles and black triangles in the simulation results represent non-MLI and MLI debris respectively.

Chapter 6

Orbit Prediction of HAMR Objects

The current section expands on the results which were presented at the Advanced Maui Optical and Space Surveillance Technologies Conference in 2012 and are published in the conference proceedings (Flegel et al. 2012). The perturbation acceleration of electromagnetic radiation which is absorbed or reflected by an object increases linearly with the effective area of the object over its mass (see Sections 6.2 and 6.3). Since this force is applied over a non-zero surface area the common terminology for this effect is *radiation pressure*. Multi-layer insulation typically consists of a stack of thin, metalized foils separated by light-weight spacer material. The outer and inner cover foil are typically thicker than the inner reflector layers. Although the unit of the area loading of a material is identical to that of the area-to-mass ratio, the area loading does not take into account the orientation with respect to the radiation source or the deformation. The area loading of the cover layers is expected to be on the order of $6\,\mathrm{m}^2/\mathrm{kg}$ while that of the reflector layers can reach values of up to $115\,\mathrm{m}^2/\mathrm{kg}$ (Section 5.1).

Figure 6.1 shows the relation of major acceleration forces over distance from the Earth's center. In terms of radiation pressure perturbations, only the direct solar radiation pressure (SRP) for spherical objects is shown. The accelerations were determined using the numerical propagator *ZUNIEM* which is described in Section 6.2. Accelerations are averaged over several revolutions and are calculated for circular orbits in the equatorial plane. Atmospheric drag acceleration is calculated but not applied so that data for objects in LEO is not skewed by orbital decay. Non-spherical Earth effects are modeled up to degree and order

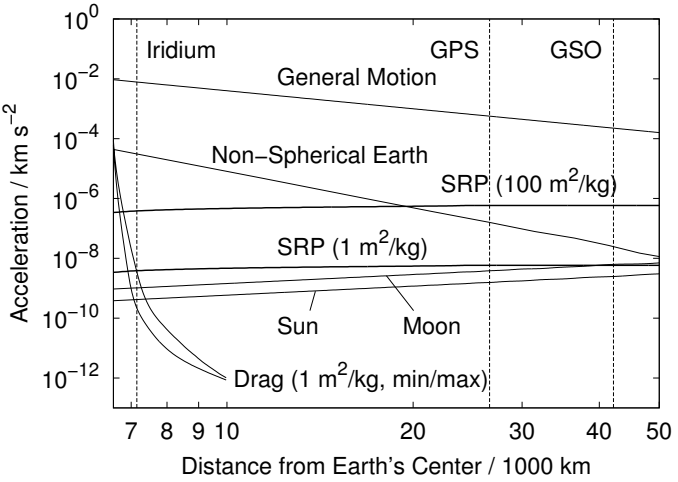

Figure 6.1: Order of magnitude of selected accelerations on objects orbiting Earth versus distance from the Earth's center. Direct solar radiation pressure (SRP) accelerations are given for area-to-mass ratios of $1\,\mathrm{m}^2/\mathrm{kg}$ and $100\,\mathrm{m}^2/\mathrm{kg}$.

12. For area-to-mass ratios of $1\,\mathrm{m}^2/\mathrm{kg}$, the solar radiation pressure accelerations are on the order of the solar and lunar perturbations. At $100\,\mathrm{m}^2/\mathrm{kg}$, the direct solar radiation pressure acceleration becomes the dominant perturbation at GEO altitudes. For these very high area-to-mass ratios it stands to reason that other influences such as object shape and orientation as well as weaker radiation sources such as radiation reflected or emitted from the Earth can have non-negligible effects.

It is the aim of this chapter to gain some insight into the orbit prediction errors of large HAMR object populations which may result from simplified radiation pressure models. Orbit evolution will be modeled using a special perturbations based propagator. Initially an overview is given of sources of potential errors in radiation pressure modeling. This is followed by a short description of the special perturbations propagator as well as adaptations which were made in order to account for some additional radiation pressure effects. The influence of these effects is exemplified through comparison to spherical HAMR objects

which are perturbed only by direct solar radiation pressure and taking into account the Earth's shadow. The orbit evolution of individual objects and larger HAMR object populations is looked at. The chapter finishes with a summary of the findings.

6.1 Overview of Effects

For the case of HAMR objects, the effect of different physical models on the object position prediction accuracy is discussed for instance by Kelecy and Jah (2009a), Kelecy and Jah (2009b) and DeMars et al. (2011). Vallado (2005) gives a list of some common simplifications in modeling approaches and in the computations and compares their effects on the orbit evolution. Accurately calculating the influence of non-conservative forces such as radiation pressure with eclipse periods or atmospheric drag is a difficult task. It becomes even more challenging when abrupt changes in the perturbations occur as, for example, when an object crosses into or out of the Earth's shadow. This especially is an issue for numerical integrators. The accuracy of the orbit prediction is therefore increasingly affected by the methods which are used to solve the equations of motion. Statistical populations try to describe the distribution and the evolution of a group of objects *as a whole*. For this case it may therefore be possible to give up some precision for individual objects while retaining sufficient accuracy for describing the behavior of the group. This approach has been chosen for many major space debris models including ESA's Meteoroid and Space Debris Terrestrial Environment Reference (*MASTER*).

Table 6.1 summarizes the deviations in position prediction accuracy as found by different authors. The error arising from not propagating to the exact points of the Earth's shadow boundary are also listed for comparison as *shadow boundary mitigation*. The results presented by Kelecy and Jah (2009a) and in Kelecy and Jah (2009b) use objects in the GEO region while Vallado (2005) presented the results for a GPS type orbit. All authors use a Monte-Carlo approach to define the initial orbit conditions. The limits for the orbit parameters defined by Kelecy and Jah for GEO are typically 38,000-46,000 km for the semi-major axis, 0.0-0.4 for eccentricity and 0-10 degrees for inclination. Area-to-mass ratio values are uniformly distributed between 0.1 and 20 m^2/kg, unless stated otherwise. The presented numbers published by Vallado are based on a single GPS satellite with an un-

specified area-to-mass ratio. His results show that the accuracy of a numerical propagator may depend more on the correct treatment of the transition into and out of the Earth's shadow than the use of a high fidelity shadow model.

Table 6.1: Overview of some results of different radiation pressure models on the position prediction accuracy. The average deviation is given in kilometers after a fixed time frame presented in brackets.

Model	*Baseline*	*Average Influence*
Fixed Plate vs. Rotating Cube[1]	GEO	200 – 300 km (7 days)
30 % change in Diffuse- and Specular Reflectivity and Absorption[1]	GEO	50 – 100 km (7 days)
1 % change in $(A/m)_{\text{eff}}$ [1]	GEO	10 – 20 km (7 days)
Cylindrical vs. Physical Shadow Model[1]	GEO	1 – 2 km (7 days)
Thermal Emission Dynamic Temperature vs. Constant Temperature (fixed orientation)[2]	GEO	60 – 80 km (1 day)
Thermal Emission Fixed Orientation vs. Random Rotation (constant temperature)[2]	GEO	40 – 60 km (1 day)
No Shadow vs. Dual-Cone Shadow Model[3]	GPS	10^{-2} – 10^{-1} km (4 days)
Shadow Boundary Mitigation[3]	GPS	10^{-3} – 10^{-2} km (4 days)
Cylindrical vs. Dual-Cone Shadow Model[3]	GPS	ca. 10^{-3} km (4 days)
Light delay from Sun to central body vs. Sun to satellite[3]	GPS	10^{-4} – 10^{-3} km (4 days)
No light delay from Sun vs. light delay from Sun to satellite[3]	GPS	10^{-4} – 10^{-3} km (4 days)
Increased effective Earth radius vs. Attenuation from Atmosphere[3]	GPS	10^{-5} – 10^{-4} km (4 days)

Thermal emissions seem to have the highest influence followed by fixed plate vs. rotating cube. Cylindrical vs. dual-cone shadow model is the only effect taken into account by both Kelecy and Vallado although implementations differ. For the current work, it is decided to concentrate on the effect of oriented and rotating objects.

[1] Kelecy and Jah (2009a)
[2] Kelecy and Jah (2009b)
[3] Vallado (2005)

6.2 Special Perturbations Model

The current section gives an overview of the numerical propagator *ZUNIEM* (**Zu**schlag **N**umerical **I**ntegration of the **E**quations of **M**otion) which is being developed at the Institute of Aerospace Systems of the Technische Universität Braunschweig. This propagator is expanded in the current work to analyze the effects of perturbative forces specific to HAMR objects.

Integrating equations of motion The equation of motion of an arbitrary object in Earth orbit is given by:

$$\ddot{\boldsymbol{r}}(t) = -\frac{\mu}{r^3} \cdot \boldsymbol{r}(t) + \boldsymbol{f}(t) \tag{6.1}$$

In this equation, $\boldsymbol{r}$ is the time variant position of the object, μ is the Earth's gravity constant and $\boldsymbol{f}$ is the sum of all time dependent perturbing acceleration. Introducing a state-vector $\boldsymbol{X}$ and its time derivative $\dot{\boldsymbol{X}}$ (Equation 6.2) allows to reformulate the three second-order differential equations from Equation 6.1 into six coupled first-order differential equations. The advantage of this variation of **Cowell's formulation** is that more integration methods exist for solving of first-order differential equations than exist for second-order differential equations. *ZUNIEM* in the current version uses the Shampine-Gordon multi-step, single integration technique.

$$\boldsymbol{X} = \begin{pmatrix} \boldsymbol{r} \\ \dot{\boldsymbol{r}} \end{pmatrix} \qquad \dot{\boldsymbol{X}} = \begin{pmatrix} \dot{\boldsymbol{r}} \\ -\frac{\mu}{r^3} \cdot \boldsymbol{r}(t) + \boldsymbol{f}(t) \end{pmatrix} \tag{6.2}$$

Earth geopotential Acceleration due to the non-spherical Earth gravity field are modeled by calculating the partial derivatives of Earth's potential in the Geocentric Celestial Reference Frame (GCRF) (Vallado and McClain 2007). The Earth's potential is described through the deviation from a spherical one. Using *spherical harmonics*, this is done through Legendre polynomials which are weighted by numerical coefficients $C_{n,m}$ and $S_{n,m}$. The indices n and m are integers which dictate the degree and order of the variations. Setting n and m to zero returns the spherical potential. Low non-zero values describe the primary deformation of the Earth. As an example, $n = 2$ and $m = 0$ give a relation for the Earth's flattening which results from its rotation. This deformation causes a secular drift in the right ascension of the ascending node of orbiting objects. It is

especially important to account for this perturbation when predicting the evolution of low Earth orbits. In general, zonal harmonics ($m = 0$) describe how the Earth's potential changes between latitudes. Sectoral harmonics ($m = n$) model changes in longitude and tesseral harmonics ($m, n \neq 0$ and $m \neq n$) try to reproduce changes in specific regions of the Earth. With increasing values of n and m, the modeled zones become smaller.

The major deformations create the largest orbit variations. Only zonal harmonics with even values for n produce secular changes. At geosynchronous altitudes, deformations of the Earth's equator which are described through sectoral and tesseral harmonics cause the objects to librate about two stable points on opposite sides of the Earth. Which harmonics are required to adequately describe the orbital evolution of an object thus depends on the initial orbit and especially the orbit altitude. Absolute values of acceleration stemming from the Earth's gravity decrease with the square of the distance (compare Equation 6.1 and Figure 6.1). Semi-analytic models typically try to capture secular, long-periodic, and sometimes also major resonance effects on the orbit evolution. Most of these are accounted for by harmonics up to degree and order 6 (Vallado and McClain 2007, Klinkrad and Martin 2006). For the current study harmonics up to $n = m = 12$ are simulated.

Direct solar radiation pressure In the current section, radiation pressure is modeled for a body with a finite number of flat surfaces and the Sun as the only radiation source (see Equation 6.3). Self radiation is not taken into account. A generic formulation for multiple sources of radiation is given in Appendix D. The bi-conic Earth shadow model according to Montenbruck and Gill (2000) is used. Figure 6.2 shows the definition of the relevant vectors.

$$\boldsymbol{a}_{\mathrm{RP}} = -\frac{\Phi_{\odot}\, S_{\odot}}{m_{\mathrm{obj}}\, c} \sum_{i=1}^{n} \left[\boldsymbol{R}_{i,\odot} \frac{(\boldsymbol{s}_{i,\odot} \circ \boldsymbol{n}_i)}{\|\boldsymbol{s}\|_{i,\odot} \cdot \|\boldsymbol{n}\|_i} A_i \right] \; ; \forall \; (\boldsymbol{s}_{i,\odot} \circ \boldsymbol{n}_i) > 0 \qquad (6.3)$$

n	total number of surface elements of object	–
$\boldsymbol{a}_{\mathrm{RP}}$	radiation pressure acceleration	m/s
m_{obj}	object mass	kg
c	speed of light	m/s
A_i	area of flat surface element i	m^2
$\Phi_{\odot}$	electromagnetic radiation flux from Sun	$\mathrm{W/m}^2$

$S_\odot$	shadow function for occultation of Sun by Earth	$\in [0,1]$
$\boldsymbol{R}_{i,\odot}$	reflectance vector for flat surface element i relative to Sun	$\|\boldsymbol{R}\| \in [1,2]$
$\boldsymbol{s}_{i,\odot}$	vector pointing from surface element i to Sun	m
$\boldsymbol{n}_i$	surface element i normal vector	m

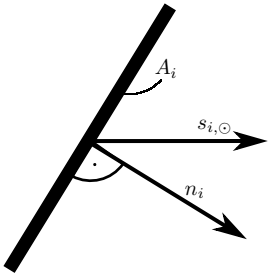

Figure 6.2: Vector definition for incident radiation on surface i from the Sun ($\odot$).

Atmosphere The NRLMSISE-00 (NRL Mass Spectrometer and Incoherent Scatter Radar) model is used to determine atmospheric density. The model inputs are daily as well as 81-day centered values of the 10.7-cm solar radio flux ($F_{10.7}$) and 3-hour geomagnetic activity index values (A_p) along with the daily average value (Picone et al. 2002). Parameters are provided via `www.celestrak.com` which are updated every 3 hours. Additionally historic data starting from January 1962 and predictions for $F_{10.7}$ values are provided for 10 years.

Sun and Moon gravity Gravitational attraction from Sun and Moon are modeled based on the assumption of point masses. The rotation of Earth and Moon around a common center of mass is taken into account.

6.3 Extending the Special Perturbations Model

Radiation pressure acting on single surface elements of debris fragments will result in a translational acceleration and a rotational acceleration. In order to model this effect, a six degrees-of-freedom (DOF) model must be constructed. The performance of such a model has been demonstrated by DeMars et al. (2011) for instance. Such a model requires a detailed understanding of the fragment shapes

to be modeled. In the current study, it will be assumed that all MLI fragments consist of flat plates with homogeneous optical properties over the two surfaces. For this case, rotational acceleration due to radiation pressure exists only in special cases such as during transit of the Earth's shadow boundary. In the current work the effect of the orientation, as well as the optical properties of the two opposing sides is modeled using a three DOF model for the translational accelerations alone.

In this section the mathematical ground work is initially presented which is required for the implementation of oriented and rotating objects into the software *ZUNIEM*. The section closes with an investigation of the influence of orientation and rotating motion on the orbit evolution of single objects and on a statistical HAMR object population.

6.3.1 Inertially Fixed and Rotating Plates

The current section gives the formulations required to describe a surface which is defined in a body frame which in turn has a known orientation within an inertial frame. Finally, the approach chosen to simulate a rotating motion is described.

Object Surfaces in Body Frame Surface normal vectors $\boldsymbol{n}_i$ define the orientation of each external surface i within a body fixed frame (index B):

$$\boldsymbol{n}_i^B = \underline{n}_i^T \cdot \underline{\boldsymbol{e}}^B \tag{6.4}$$

where the basis of the right-handed orthonormal body frame is given by:

$$\underline{\boldsymbol{e}}^B = \begin{pmatrix} \boldsymbol{e}_{xB} \\ \boldsymbol{e}_{yB} \\ \boldsymbol{e}_{zB} \end{pmatrix} \tag{6.5}$$

Object Surfaces in Inertial Frame Within ZUNIEM, all translational accelerations are calculated in the *Earth Centered Inertial* (ECI) reference frame. As such, Equation 6.3 is also given in ECI coordinates. The orientation of a surface normal vector $\boldsymbol{n}_i^B$ expressed in the ECI frame (index E) can be obtained through a rotation. This is done by multiplying the vector with the so called *direction-cosine* matrix $\underline{\underline{T}}_E^B$:

$$\boldsymbol{n}_i^E = \underline{\underline{T}}_E^B \cdot \boldsymbol{n}_i^B. \tag{6.6}$$

In the current form, the direction-cosine matrix contains the three axes $\boldsymbol{e}_{xE}$, $\boldsymbol{e}_{yE}$, $\boldsymbol{e}_{zE}$ of the ECI frame expressed in the body frame [1]:

$$\underline{\underline{T}}_E^B = \begin{pmatrix} \boldsymbol{e}_{xE} \\ \boldsymbol{e}_{yE} \\ \boldsymbol{e}_{zE} \end{pmatrix}^B . \tag{6.9}$$

The direction-cosine matrix may be derived using different approaches. A common method is by performing three *successive* rotations about the ephemeral axes of the body frame. The three angles used in this process are called *Euler angles*. Another method is possible by rotating the body frame only once by an angle $\mu = \|\boldsymbol{\mu}\|$ about a vector $\boldsymbol{\mu}$ with fixed orientation in the ECI frame. This latter option is the basis of the quaternions which were introduced by Hamilton (1848). A quaternion $\boldsymbol{q}$ is basically a vector with *four* elements:

$$\boldsymbol{q} = \begin{pmatrix} q_1 \\ q_2 \\ q_3 \\ q_4 \end{pmatrix} = \begin{pmatrix} \frac{\boldsymbol{\mu}}{\|\boldsymbol{\mu}\|} \cdot \sin\frac{\mu}{2} \\ \cos\frac{\mu}{2} \end{pmatrix} = \begin{pmatrix} \frac{\mu_x}{\|\boldsymbol{\mu}\|} \cdot \sin\frac{\mu}{2} \\ \frac{\mu_y}{\|\boldsymbol{\mu}\|} \cdot \sin\frac{\mu}{2} \\ \frac{\mu_z}{\|\boldsymbol{\mu}\|} \cdot \sin\frac{\mu}{2} \\ \cos\frac{\mu}{2} \end{pmatrix} \tag{6.10}$$

Because a quaternion uses four elements to describe a three-dimensional problem, one additional constraint must be given:

$$q_1^2 + q_2^2 + q_3^2 + q_4^2 = 1. \tag{6.11}$$

A special case exists for zero rotation angle quaternion: $\boldsymbol{q}^T = (0,0,0,1)$. The direction cosine matrix in Equation 6.6 can be expressed through Euler angles

[1] For clarification: If the ECI frame were rotated about the $\boldsymbol{e}_{xB}$ axis of the body frame by an angle α, then the representation of these axes in the body frame would be:

$$\boldsymbol{e}_{xE}^B = \begin{pmatrix} 1 \\ 0 \\ 0 \end{pmatrix}^T \qquad \boldsymbol{e}_{yE}^B = \begin{pmatrix} 0 \\ \cos\alpha \\ \sin\alpha \end{pmatrix}^T \qquad \boldsymbol{e}_{zE}^B = \begin{pmatrix} 0 \\ -\sin\alpha \\ \cos\alpha \end{pmatrix}^T \tag{6.7}$$

and the resulting direction-cosine matrix:

$$\underline{\underline{T}}_E^B = \begin{bmatrix} 1 & 0 & 0 \\ 0 & \cos\alpha & \sin\alpha \\ 0 & -\sin\alpha & \cos\alpha \end{bmatrix} . \tag{6.8}$$

as well as quaternions. Two major advantages of quaternions over Euler angles surface when changes in the object's angular velocity vector are accounted for; the kinematic equations will be presented in the following paragraph. For one, the computation time is shorter when using quaternions. More importantly however, the kinematic equations for the Euler angles have a singularity which requires a workaround and which does not appear when using quaternions. For the current work it is therefore decided to use quaternions.

Typically, the orientation of the *body frame* within the ECI frame is given as a starting point. The above quaternion would therefore be given as

$$\boldsymbol{q} = \boldsymbol{q}_B^E \tag{6.12}$$

which would lead to $\underline{\underline{T}}_B^E$ instead of the sought $\underline{\underline{T}}_E^B$ (Equation 6.6). Due to the orthonormality of the basis, the two matrices can however easily be translated into one another:

$$\underline{\underline{T}}_E^B = \left(\underline{\underline{T}}_B^E\right)^{-1} = \left(\underline{\underline{T}}_B^E\right)^T . \tag{6.13}$$

The direction-cosine matrix thus becomes:

$$\underline{\underline{T}}_E^B\left(\boldsymbol{q}_B^E\right) = \begin{bmatrix} q_1^2 - q_2^2 - q_3^2 + q_4^2 & 2\cdot(q_1\cdot q_2 - q_3\cdot q_4) & 2\cdot(q_1\cdot q_3 + q_2\cdot q_4) \\ 2\cdot(q_1\cdot q_2 + q_3\cdot q_4) & -q_1^2 + q_2^2 - q_3^2 + q_4^2 & 2\cdot(q_2\cdot q_3 - q_1\cdot q_4) \\ 2\cdot(q_1\cdot q_3 - q_2\cdot q_4) & 2\cdot(q_2\cdot q_3 + q_1\cdot q_4) & -q_1^2 - q_2^2 + q_3^2 + q_4^2 \end{bmatrix} . \tag{6.14}$$

Rotating Motion All rotating objects are gyroscopes. The motion of a gyroscope can be modeled using Euler's equations of motion. These equations allow for external moments to influence the rotation of an object. Appendix D.2 contains these equations for the current case using simplifications for the shape of the objects. The orientation of a HAMR object has significant influence on the radiation pressure effect and thus on its orbit evolution. It follows that a realistic description of the rotating motion is essential to being able to track individual objects. Unfortunately the computational effort is high since integration is required to solve these equations. Especially when propagating large numbers of objects over extended time frames, this is an important aspect. Since the population which will be looked at with respect to its overall evolution is statistical in nature, simplifications are admissible as will be seen. Currently, plate-like objects

are assumed with a rotation axis fixed in ECI and constant rotation rate. Nutation, precession and unstable rotations are thus neglected here. The magnitude of a quaternion is equivalent to the rotation angle about the rotation axis. The new orientation at each time step in the simulation can therefore simply be obtained by multiplying the magnitude with the time elapsed since the beginning of the simulation:

$$\mu = \mu_0 \cdot \Delta t_{\text{sim}} \quad . \tag{6.15}$$

The new values for the four elements of the new quaternion are then calculated using Equation 6.10. The initial orientation and rotation axis are treated independently of one another. The rotation axis can therefore be oriented at any angle with respect to the surface normal vector.

6.3.2 Reflectivity Coefficient

The reflectivity coefficient is often denoted as C_R or c_R in the literature and is the equivalent of the magnitude of the reflectance vector $\boldsymbol{R}$. According to (Marshall and Luthcke 1994), (Vallado and McClain 2007), the reflectance vector can be expressed as function of specular reflectivity ρ_s, diffuse reflectivity ρ_d and the orientation of the surface $\boldsymbol{n}_i$ with respect to the position of the radiation source $\boldsymbol{s}_{i,\odot}$:

$$\boldsymbol{R}_{i,\odot} \quad = \quad (1-\rho_{s,i}) \cdot \hat{\boldsymbol{s}}_{i,\odot} + 2 \cdot \left[\frac{(\boldsymbol{s}_{i,\odot} \circ \boldsymbol{n}_i)}{\|\boldsymbol{s}\|_{i,\odot} \cdot \|\boldsymbol{n}\|_i} \rho_{s,i} + \frac{1}{3}\rho_{d,i} \right] \cdot \hat{\boldsymbol{n}}_i \tag{6.16}$$

where $\|\boldsymbol{R}\|_{i,\odot} \in [1,2]$. For a homogeneous sphere, the surface normal vector $\boldsymbol{n_i}$ and the vector pointing from the surface to the radiation source $\boldsymbol{s}_{i,\odot}$ in Equation 6.16 are parallel to one another and their unit vectors are therefore identical $\hat{\boldsymbol{s}}_{i,\odot} \equiv \hat{\boldsymbol{n}}_i$:

$$\boldsymbol{R}_{i,\odot} = \left(1 + \rho_{s,i} + \frac{2}{3}\rho_{d,i}\right) \cdot \hat{\boldsymbol{s}}_{i,\odot} \tag{6.17}$$

The same conditions also apply to plates which are oriented normal to the radiation source. Table 6.2 summarizes the corner values which the reflectivity coefficient can take on for these objects. The absorptivity $\alpha = 1 - (\rho_s + \rho_d)$ is included for completeness.

Table 6.2: Range of reflectivity coefficient $C_R \equiv \|\boldsymbol{R}\|$ values for a sphere or flat plate oriented normal to the incident radiation according to Equation 6.17. α is the amount of incident light which is absorbed, ρ_s is the amount which is reflected specularly and ρ_d the amount which is reflected diffusely.

α	ρ_s	ρ_d	C_R
1	0	0	1
0	1	0	2
0	0	1	$1\frac{2}{3}$

6.4 Orbit Evolution of HAMR Objects

This section gives an overview of the evolution of geosynchronous HAMR objects. Specifically the influence of the area-to-mass ratio and the effect of the object shape on the orbit are investigated. The influence of the area-to-mass ratio on the orbit is evaluated for spherical objects by varying the ratio between 1 and 51 m^2/kg in steps of 1 m^2/kg. The effect of plate-like objects compared to spherical objects is inspected by considering two cases: In the first case the orientation of the plates is kept inertially fixed. This allows to characterize the effect of different orientations on the orbit evolution. In a second case, an inertially fixed axis of rotation is defined. In this scenario, the effect of the inertial orientation of the rotation axis as well as the rate of rotation on the orbit is evaluated. The plates have a constant area loading of $A/m = 27.8\,\mathrm{m}^2/\mathrm{kg}$ which corresponds to that of aluminized polyimide with a thickness of 1 mil (= 25 μm) (Sheldahl 2012). Since only the influence of direct solar radiation pressure is taken into account, the index $\odot$ will be omitted. As a matter of convention, the terms describing the reflective properties with respect to the Sun will be used (i.e. reflectivity = solar reflectance).
The aim of the current section is to highlight, through examples, main characteristics which are pertinent to the understanding of the behavior of larger populations of HAMR objects. To start out, parameters which are common to all simulations in this section are detailed. This is followed by independent discussions of the orbit evolution of spherical HAMR objects and inertially fixed and rotating HAMR plates.

6.4.1 Common Simulation Parameters

The initial orbit, simulation start epoch and reflectivity values as presented in Table 6.3 are used for all cases in the current section. Keeping the simulation start epoch fixed removes the influence of the initial position of the Sun, the Moon and the location of the Moon's ascending node. Rosengren and Scheeres (2008) showed that a resonance with the Saros occurs for HAMR objects released on GEO which have an effective area-to-mass ratio $(A/m)_{\text{eff}} = (A/m) \cdot C_R$ of around $20\,\text{m}^2/\text{kg}$. The Saros is a cycle with a period of about 6585.3213 days after which the orientation of the Moon's nodes with respect to the location of the Sun reoccurs. In their simulations, this caused variations in the the orbit evolution which are on the order of the effect of the effective area-to-mass ratio which will be discussed here. The reflectivity of aluminized Kapton (= aluminized polyimide) as derived by Fischer (2011) is applied ($\rho = 0.626 = \rho_s + \rho_d$). It is assumed that specular ρ_s and diffuse ρ_d reflectivity take on equal parts.

Table 6.3: Initial orbit, simulation start epoch and optical properties for orbit evolution analysis of spheres and plates.

Singly averaged orbit elements		Optical Properties	
Semi-major axis	42164 km	ρ_s	0.313
Eccentricity	1.d-5	ρ_d	0.313
Inclination	1 °		
Right ascension of ascending node (RAAN)	180 °		
Argument of perigee	90 °		
Mean anomaly	90 °		
Start epoch	March 21, 2009		

6.4.2 Spherical Objects

This section treats the orbit evolution of spherical object with initial orbits and reflective properties as shown in Table 6.3. Inserting the specular and diffuse reflectivity into Equation 6.17 gives an estimation of the reflectivity coefficient for spherical objects: $C_{R\,\text{sphere}} = 1.522$ which is used for the optical properties in all simulations involving spherical objects. To obtain insight into the effect of area-

to-mass ratio on the eccentricity-, inclination- and semi-major axis evolution, the area-to-mass ratio is varied in steps of $1\,m^2/kg$ between 1 and $51\,m^2/kg$.

Eccentricity

The eccentricity oscillates with a period of about a year (see top plot in Figure 6.3). At $1\,m^2/kg$, the maximum eccentricity is roughly 0.02. The maximum peak-to-peak eccentricity increases with higher area-to-mass ratios while the period at which it changes decreases (lower plot in Figure 6.3). Upwards of an effective area-to-mass ratio of about $48\,m^2/kg$, the eccentricity increases to the point where objects interact with the upper atmosphere causing them to deorbit within a few years. The eccentricity period plotted in Figure 6.3 is a fit to the actual data. The data points along with the fit and the respective equation are presented in Appendix C. For spherical objects, the eccentricity seems to return to near zero at the end of every annual cycle. This evolution is supported by e.g. Anselmo and Pardini (2010). For oriented objects a superimposed change in the eccentricity may occur. It should be noted that publications by other groups who are also using numerical propagators exist in which such superimposed beats are also observed for spherical objects (Anselmo and Pardini 2005, Schildknecht et al. 2008b).

Inclination

The top plot in Figure 6.4 shows the inclination evolution over time of three exemplary objects with area-to-mass ratios of 1, 10 and $28\,m^2/kg$. At $1\,m^2/kg$, solar radiation pressure acceleration is on the order of the Sun's and the Moon's (compare Figure 6.1) so that the orbit evolution is similar to that of uncontrolled satellites. The orientation of a satellite's orbit in the ECI system can be described simply by an orbit normal vector or by its inclination and right ascension of ascending node. The orbit normal vector of uncontrolled objects in near circular geosynchronous orbits precesses about a pole which is oriented at an angle to the Earth's rotation axis. The plane normal to this vector is called the *Laplace* plane. For non HAMR objects the offset angle of the Laplace plane is approximately $7.5\,°$. This pole is independent of the initial orbit orienation. Unlike to the orientation of the Laplace plane, the precession period varies depending on the inital orbit. For objects originating in the equatorial plane the precession period is about 53 years. Especially for orbits with initial right ascension of ascending node around $180\,°$ an non zero inclination the precession period increases. The

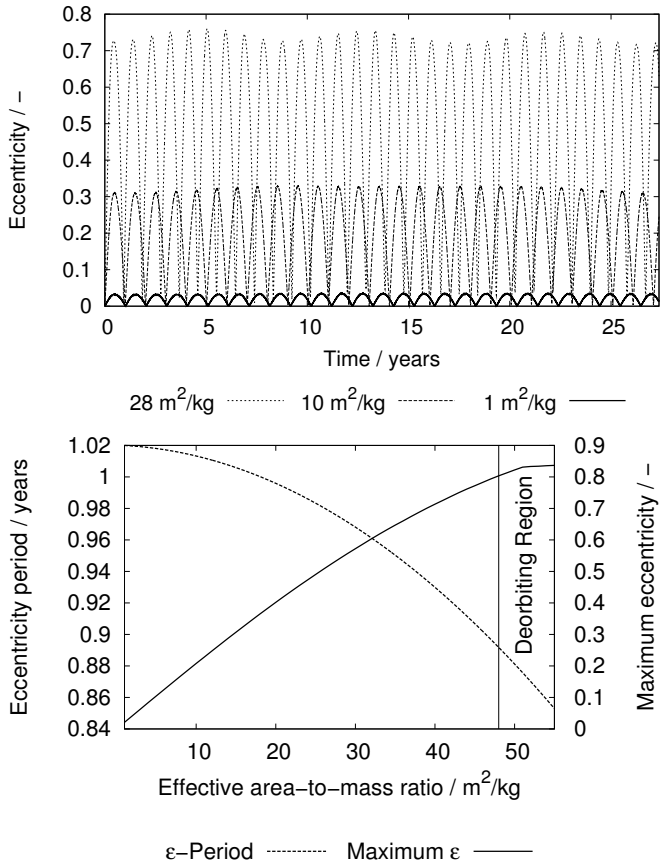

Figure 6.3: Spheres. Top: Exemplary eccentricity evolution for area-to-mass ratios 1, 10 and 28 m^2/kg with $C_{R\,\mathrm{sphere}} = 1.522$. Bottom: Dependency of maximum eccentricity and eccentricity oscillation period on effective area-to-mass ratio ($A/m \cdot C_R$).

pole of the precession wanders slightly as a result of the precession of the Moon's orbit about the pole of the ecliptic (Allan and Cook 1963). The maximum inclination for orbits which start out within the equatorial plane and for which Luni-

solar perturbations are prevalent thus is limited to about 15°. HAMR objects undergo a similar precession about an altered Laplace plane where the offset of the precession pole increases with the area-to-mass ratio. The relation between area-to-mass ratio and maximum attained inclination is depicted by the solid line in the lower plot in Figure 6.4. The broken line in the plot demonstrates the sensitivity of the precession period to the area-to-mass ratio. As a first order approximation, the maximum inclination increases linearly with the effective area-to-mass ratio for spherical objects. The precession period decreases quickest at ratios between 10 and 20 m^2/kg. This decrease approaches a linear trend in a log-lin representation above 15 m^2/kg (not shown here).

The maximum inclination of spherical objects is attained at RAAN values close to zero degrees and is independent of an object's area-to-mass ratio. If one were to describe the orientation of the Laplace plane using terms applied to Keplerian orbits, its right-ascension of ascending node would be about 90° and its inclination would be 7.5° for objects with low area-to-mass ratios. While an increased area-to-mass ratio would effect the inclination of this plane, its right-ascending of ascending node would remain unaltered.

Semi-major axis

The semi-major axis shows how the orbit energy is influenced by the radiation pressure. For most cases, spherical objects retain no secular changes in orbit energy. Short- and long-periodic beats are however observed spanning several years. Figure 6.5 shows semi-major axis evolutions for three area-to-mass ratios. For objects with very low area-to-mass ratios (1 m^2/kg), the deformation of the Earth's equator dominates the evolution of the semi-major axis causing the object to librate about a stable point (see also Section 6.2). This well behaved evolution breaks up between *effective* area-to-mass ratios of 5 to 8 m^2/kg. Up to an effective area-to-mass ratio of about 25 m^2/kg, secular effects may change the mean semi-major axis by more than 100 km. Beyond 28 m^2/kg, a recurring superimposed beat with a period of about 8 to 9 years is fully developed, and no further secular orbit changes are observed. The libration period is on the order of a few years. Above 8 m^2/kg, an annual variation replaces this oscillation which coincide with the two phases in which the orbit intersects the Earth's shadow. The relation between maximum deviation in semi-major axis over a 27 year simulation period from the original 42,164 km is shown in Figure 6.6. Even through the region in

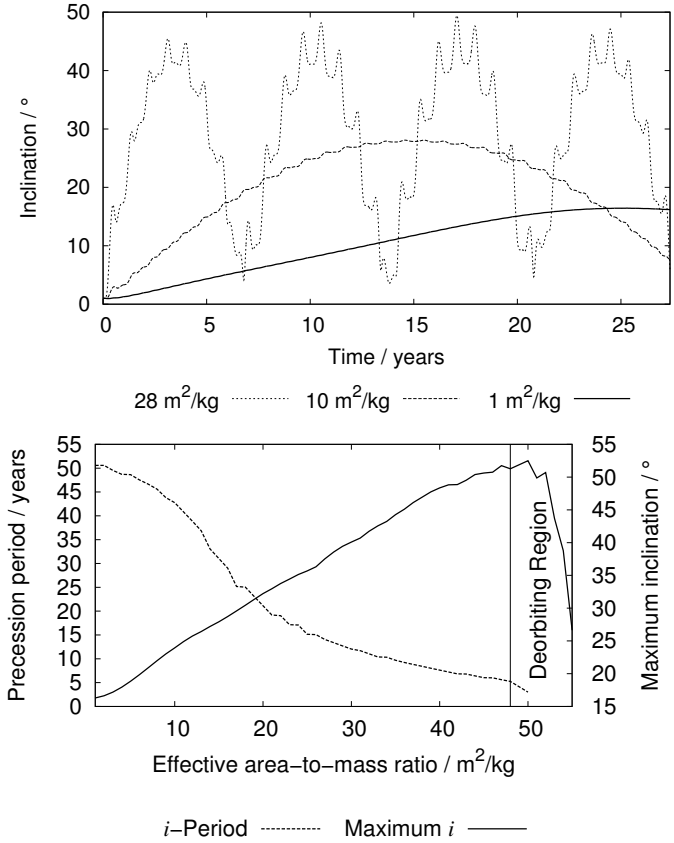

Figure 6.4: Spheres. Top: Exemplary inclination evolution with $C_{R\,\mathrm{sphere}} = 1.522$. Bottom: Dependency of maximum inclination and precession period on effective area-to-mass ratio ($A/m \cdot C_R$).

which secular changes in the mean semi-major axis are seen, an overall trend can be observed.

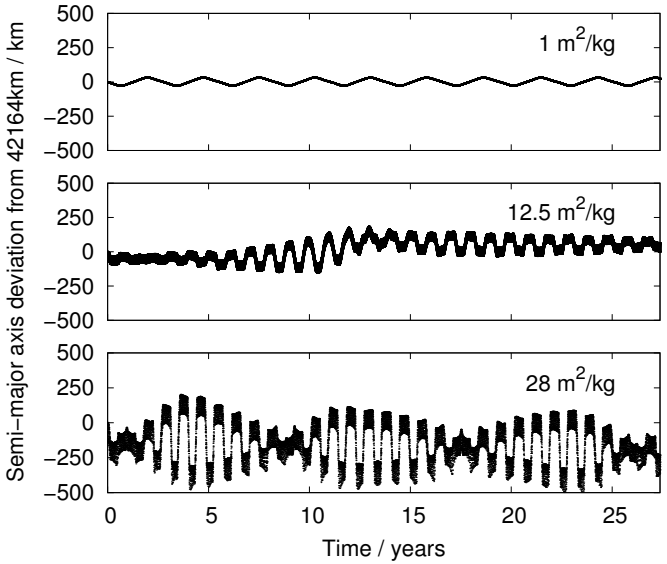

Figure 6.5: Spheres. Exemplary semi-major axis evolution with $C_{R\,\mathrm{sphere}} = 1.522$

6.4.3 Plates with Inertially Fixed Orienation

In this section the objects are assumed to be flat plates with inertially fixed orientation. Diffuse and specular reflectivity from Table 6.3 are used. The aim is to gain insight into how the direction of the acceleration vector influences the orbit evolution. The major difference to the case of spherical objects is that the direction of the SRP induced acceleration now depends on the orientation of the plates in addition to the position of the object relative to the Sun.

The orientation of the objects is described in the inertial system $\hat{\boldsymbol{I}}'\hat{\boldsymbol{J}}'\hat{\boldsymbol{K}}'$ as depicted in Figure 6.7. The prime marks ($'$) indicate that the orientation of this system is identical to the Earth Centered Inertial (ECI) system $\hat{\boldsymbol{I}}\hat{\boldsymbol{J}}\hat{\boldsymbol{K}}$ except that its origin resides in the center of mass of the orbiting Object. The unit vector $\hat{\boldsymbol{I}}$ of the ECI frame points in the direction of the vernal equinox Υ while $\hat{\boldsymbol{K}}$ is parallel to the Earth's rotation axis so that $\hat{\boldsymbol{I}}$ and $\hat{\boldsymbol{J}}$ are in the equatorial plane.

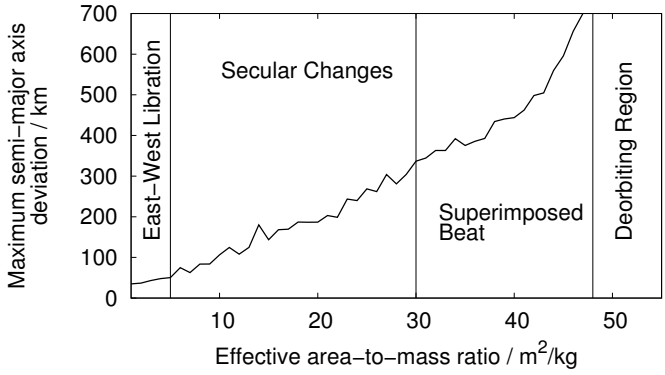

Figure 6.6: Spheres. Dependency of maximum deviation in semi-major axis from initial orbit on effective area-to-mass ratio ($A/m \cdot C_R$).

In the following section, two cases will be explored regarding the initial orientation. In both cases, the starting condition is that the surface normal vector $\boldsymbol{n}$ points along the unit vector $\hat{\boldsymbol{I}}'$ as shown in Figure 6.7. For the simulation start epoch of March 21, 2009, $\hat{\boldsymbol{I}}$ points towards the Sun so that the object's surface is perpendicular to the incident radiation from the Sun and all offset angles are zero. In the two cases addressed in this section, the effect of changing the initial object orientation by rotating about $\hat{\boldsymbol{K}}'$ and about $\hat{\boldsymbol{J}}'$ are treated separately. No mixed rotations are taken into account. In the former case, the plate's surface normal vector always remains in the $\hat{\boldsymbol{I}}' - \hat{\boldsymbol{J}}'$ plane. In the latter case the normal vector is rotated out of the $\hat{\boldsymbol{I}}' - \hat{\boldsymbol{J}}'$ plane. The $\hat{\boldsymbol{I}}' - \hat{\boldsymbol{J}}'$ plane will be termed the *equatorial plane* or simply *plane* in the following. *In-plane* rotations thus describe rotations about $\hat{\boldsymbol{K}}'$ while *out-of-plane* rotations are into rotations about $\hat{\boldsymbol{J}}'$.

For the two cases, offset angles (-90,-60,-30, 0, 30, 60, 90) have been simulated. The rotation arrows in the Figure depict the direction of positive offset angles. Short-term simulations over 1,000 days provide an initial understanding of the basic mechanisms governing the orbit evolution. Simulations over 10,000 days give insight into the long-term behavior.

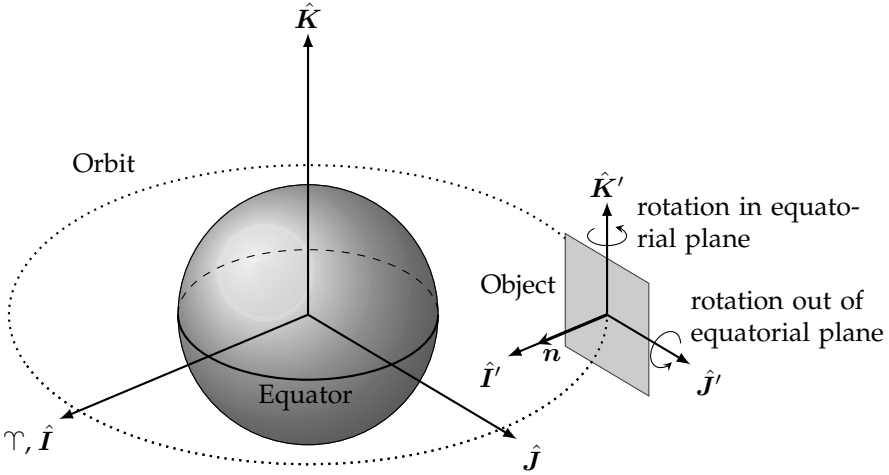

Figure 6.7: Definition of the reference frame for the description of the plates' orientation within the Earth Centered Inertial (ECI) reference frame. The unit vector $\hat{I}$ points towards the vernal equinox Υ. The rotation vectors indicate the direction of positive offset angles.

Short-term evolution

The boundaries of the effect of an oriented surface in ECI coordinates are studied here. Out of all simulated cases, the largest secular changes have been found to occur for $\pm 60\,^\circ$ in- as well as out-of-plane orientations. The $0\,^\circ$ orientation case is used as reference and is identical in both scenarios. The results for the complete range of simulations between $\pm 90\,^\circ$ are shown in Appendix E. It must be born in mind that the orbit evolution is heavily dominated by the geometric relations between the objects' surface and orbit orientation, the position of the Sun and the orbit intersections with the Earth's shadow. The initial conditions therefore have a strong influence on the orbit evolution.

Semi-major axis change Exemplary orbits are shown in Figure 6.8. The resulting solar radiation pressure for the plate with $-60\,^\circ$ in-plane orientation primarily has acceleration components in the orbital plane, affecting semi-major axis and eccentricity. Semi-major axis exhibits a pronounced step-like evolution.

Quick orbit changes are apparent during those periods in which the orbit passes through the Earth's shadow. This occurs approximately every half year. The secular westerly drift of the right-ascension of ascending node causes the time between shadow passes to be slightly less than half a year. The step-evolution is observable for oriented surfaces as well as in the results for the sphere (see Section 6.4.2). Secular effects for semi-major axis become small, if the object's surface is oriented perpendicular to the incident solar radiation during shadow passes or if it is rotated out of the equatorial plane. In the latter case, a larger orbit normal component is created.

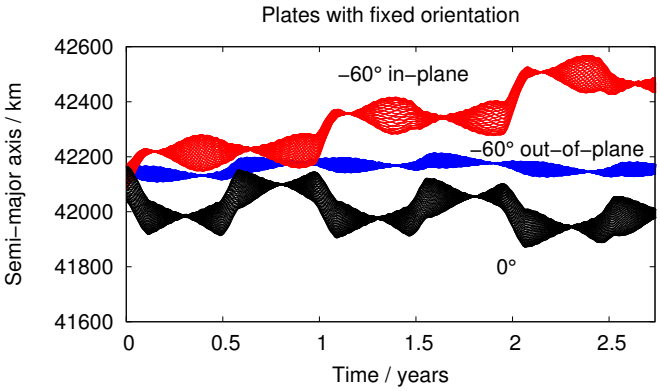

Figure 6.8: Fixed plates: Change in semi-major axis over 1,000 days for exemplary orientations.

Eccentricity change The eccentricity returns to a value near zero after slightly less than one year. Where the eccentricity evolution of spherical objects resembled an inverted parabolic which repeated itself after approximately one year, oriented objects are capable of undergoing two phases within a year in which eccentricity increases and decreases again. On average, an in-plane orientation creates larger annual eccentricity variations than an out-of-plane orientation (see Figure 6.9).

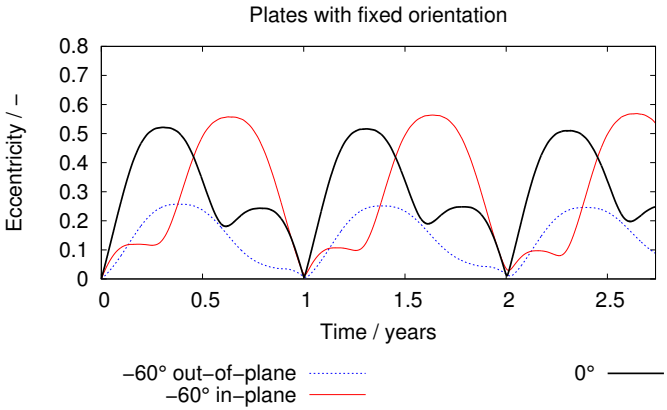

Figure 6.9: Fixed plates: Change in eccentricity over 1,000 days for exemplary orientations.

Long-term evolution

This section gives an overview of long-term trends which did not become apparent in the analysis of the short-term effects.

Semi-major axis Complex behaviors in semi-major axis evolution are observed for oriented objects with in- and out-of-plane orientation. In the time-frame of 10,000 days, in-plane orientation changes lead to an average maximum deviation from the initial semi-major axis of 2,000 km. Out-of-plane orientation changes result in 1,100 km average maximum deviation. The lower graph in Figure 6.10 compares the maximum deviation from the initial orbit for the studied orbits. The top plot in this figure shows the orbits for an object which is oriented perpendicular to the incident radiation at simulation start, and objects with -60 ° orientation change in- and out-of-plane respectively. These orbits exemplify the complexity of the evolution in semi-major axis. The simulation results of the other orbits are appended in Figure E.2.

Eccentricity change Figure 6.11 shows three evolution cases of eccentricity vs. time along with a plot of the maximum attained values in the simulations. The eccentricity of plates with out-of-plane orientation seems to always return to near

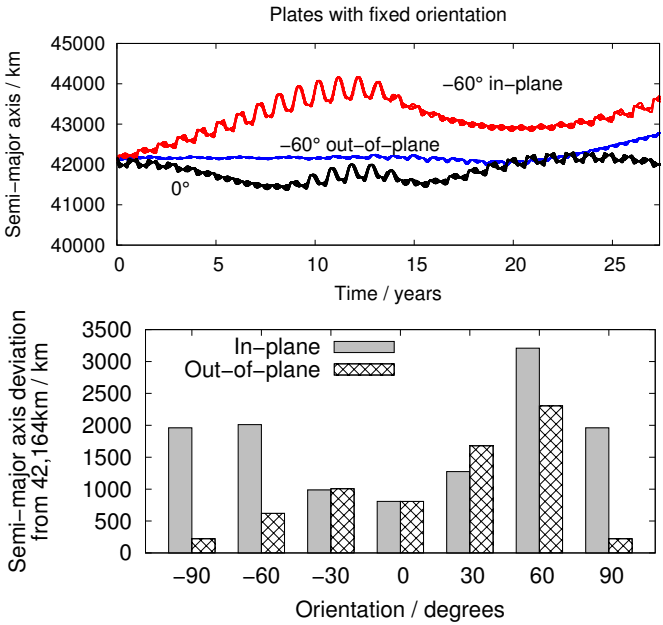

Figure 6.10: Fixed plates: Top: Change in semi-major axis over 10,000 days for selected cases. Bottom: Maximum deviation from initial semi-major axis.

zero at the end of one cycle. The maximum occurring eccentricity decreases if the object is tilted out of the orbit plane, decreasing the along-track acceleration component. Plates with different in-plane orientations exhibit a 'detaching' of the minimum eccentricity, thus undergoing long-term changes which depend on the initial orientation. The maximum attained eccentricity for this latter case remains fairly constant for all orientations.

Inclination change The orbit normal acceleration component of plates with out-of-plane orientation affects the precession period of the orbit plane. Since the orbit normal acceleration remains similar over a year for objects with in-plane orientation offset, their precession period remains constant. For both cases, the maximum inclination is highest for offset angles near zero and decreases for higher angles (top plot in Figure 6.12). Maximum inclination of plates with 90 °

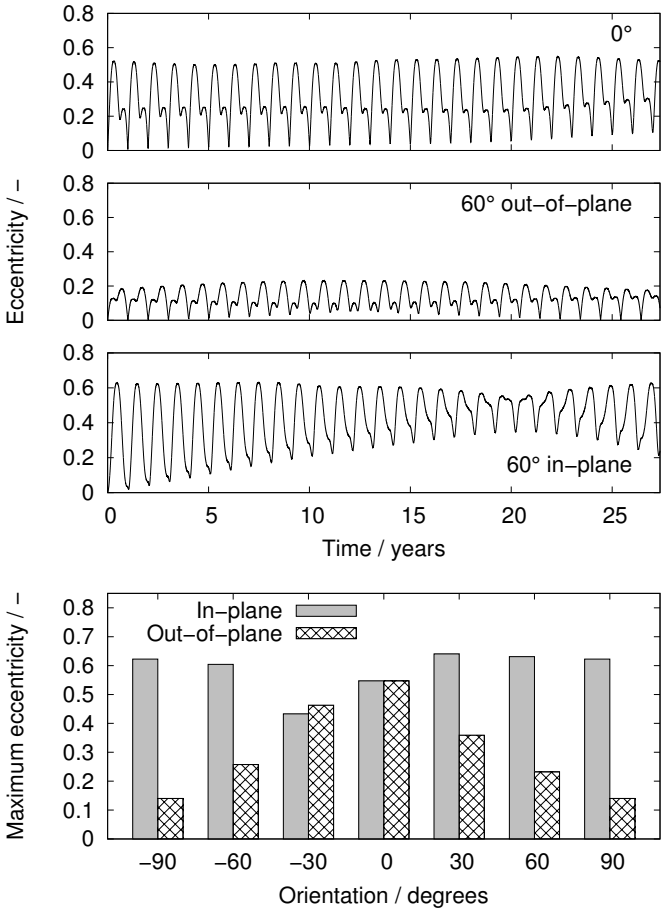

Figure 6.11: Fixed plates: Eccentricity change over 10,000 days for 0 °, 60 ° out-of-plane and 60 ° in-plane orientation. Bottom: Maximum eccentricity

in-plane orientation approaches that of objects with low area-to-mass ratios. In Section 6.4.2, the precessing of the orbit about the Laplace plane was described with terms used for keplerian orbits. For spherical HAMR objects, the inclination

of this plane increased significantly while its RAAN value however remained constant. Although this remains true for plates with in-plane orientations, out-of-plane orientation creates an offset in the RAAN of the modified Laplace plane. For plates with a positive offset angle the RAAN value is slightly lower than 90 ° and slightly higher for negative offset angles. This becomes apparent in the angular momentum unit vector plot in Figure 6.13.

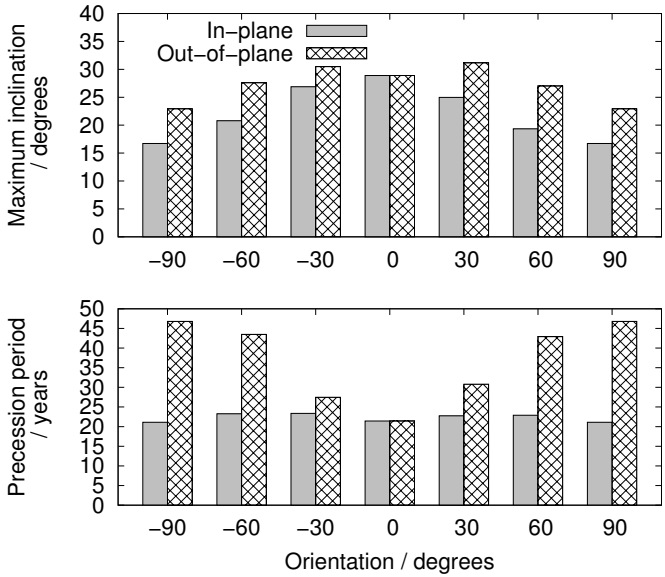

Figure 6.12: Fixed plates: Inclination evolution results for 10,000 days. Top: Maximum inclination. Bottom: Inclination period.

6.4.4 Plates with Inertially Fixed Rotation Axis

In the current section, plates are assigned inertially fixed rotation axes. The effect of the inertial orientation of this axis as well as the effect of constant rotation rates on the orbit evolution is investigated. Initially, all plates are orientated with their normal vector pointing along the unit vector $\hat{\boldsymbol{I}}'$ (see Figure 6.7). Two different orientations for the rotation axis are examined. In one case, the rotation axis

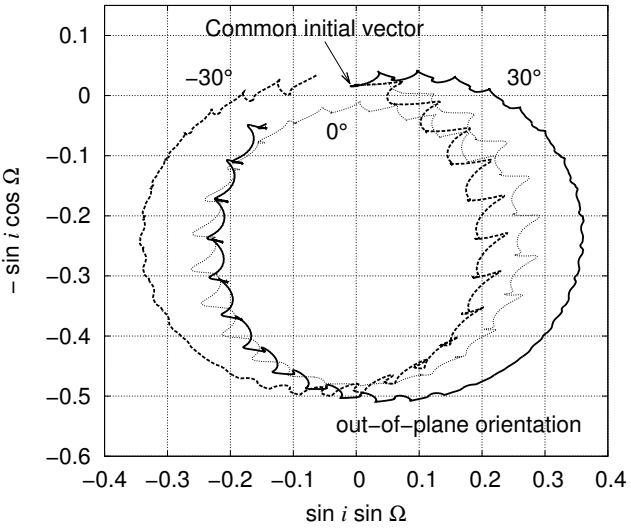

Figure 6.13: Fixed plates: Evolution of two-dimensional angular momentum unit vector for out-of-plane orientations -30, 0 and 30 °. Simulation time frame is 10,000 days.

is parallel to the unit vector $\hat{\boldsymbol{K}}'$ leading to so called in-plane rotations. In the other case, the rotation axis is parallel to the unit vector $\hat{\boldsymbol{J}}'$ whereby out-of-plane rotations are created. The term 'plane' refers to the plane described by the two unit vectors $\hat{\boldsymbol{I}}'$ and $\hat{\boldsymbol{J}}'$ which is parallel to the equatorial plane. The considered rates of rotation are 1, 10^{-1}, 10^{-2}, 10^{-3}, 10^{-4} and $1.14\times10^{-5}\,°$/s. The lowest rotation rate corresponds to the Earth's motion around the Sun. For the in-plane rotation case, the direction of rotation was chosen so that at this particular rate, the object always exhibits the same side to the Sun which leads to a resonance effect. Other resonance cases are possible such as a rotation rate corresponding to the orbit period. Since only a subset of all HAMR objects will be subject to such resonance cases, these will not be studied in detail.

Semi-major axis change Figure 6.14 shows that rotation rates which do not correspond to resonance cases have limited secular changes in orbit energy in

comparison to i.e. oriented flat plates. Rotation rates 1 and $10^{-4}\,^{\circ}/\mathrm{s}$ have almost identical long-term trends for in- and out-of-plane rotation for which reason only the $1\,^{\circ}/\mathrm{s}$ results are shown. For the in-plane rotation resonance case, the semi-major axis decreases to 28,000 km in 30 years while the perigee remains above 4000 km. For the non-resonance cases, an in-plane rotation leads to larger *annual* variations. This is consistent with the view that larger acceleration components co-planar to the orbit plane are responsible for changes in orbit energy. For the long-term evolution however, the trend reverses. Here, an out-of-plane rotation may cause the semi-major axis to build up a larger deviation from the initial GSO orbit than the in-plane rotation. This effect is currently not fully understood and should be investigated in future work.

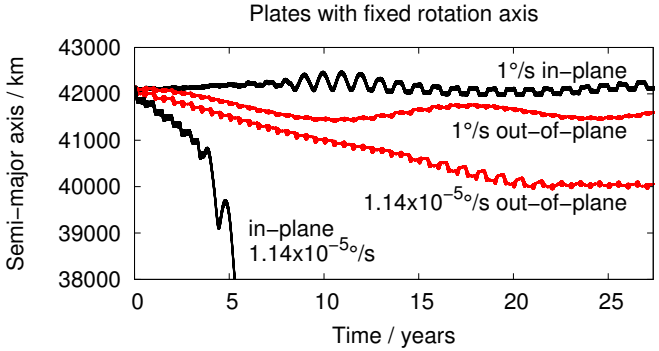

Figure 6.14: Rotating plates: Change in semi-major axis over 10,000 days.

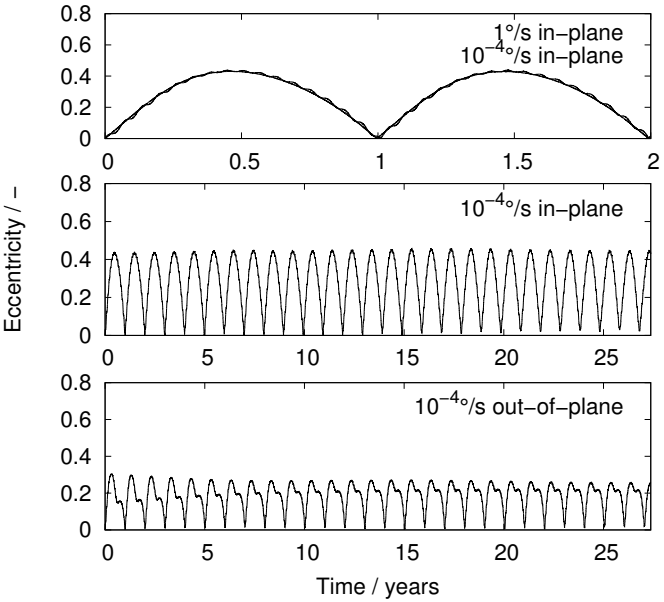

Figure 6.15: Rotating plates: Change in eccentricity over time. Top: short-term effect of rotation rate. Middle: long-term effect for in-plane rotation. Bottom: long-term effect for out-of-plane rotation.

Eccentricity change The short-term evolution is effected by the rotation rate only in that a superimposed oscillation occurs when the rotation rate approaches the resonance case. This is displayed in the top plot of Figure 6.15. Other effects stemming from rotation rate are not observed. The direction of rotation however has significance (see middle and lower plot in Figure 6.15). The maximum attainable eccentricity varies with rotation direction. Similar to the oriented objects, in- or out-of-plane rotation creates accelerations which have larger components in or normal to the orbit plane.

Inclination Inclination evolution is influenced only marginally by rotation rate. Rotation direction however has a significant effect on the maximum inclination and long-term oscillation period. In comparison, in-plane rotation causes a lower

maximum inclination and a shorter oscillation period than an out-of-plane rotation (Figure 6.16).

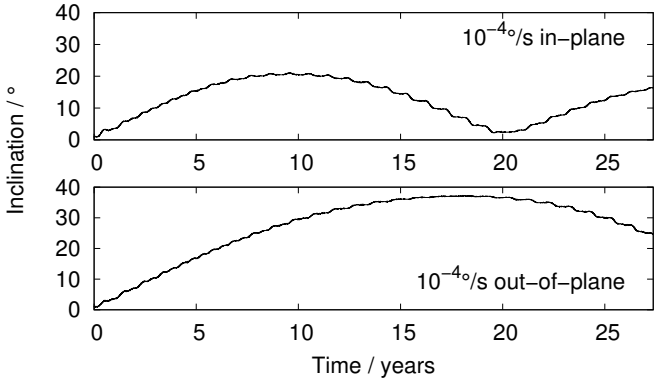

Figure 6.16: Rotating plates: Change in inclination over time. Top: long-term effect for in-plane rotation. Bottom: long-term effect for out-of-plane rotation.

6.5 Population Evolution

The evolution of a HAMR object population wherein all objects have initial orbits in GSO is looked at. An initial population is defined based on a subset of the MASTER-2009 MLI population. The objects are propagated from 2009 to 2059 using three different assumptions for the shape and orientation of the objects which are similar to the cases regarded in Section 6.4. In the first scenario, all objects in the population are simulated as spheres. In the second scenario, all objects are plates with random, but inertially fixed orientation. In the final scenario the objects have random initial orientations and random but inertially fixed rotation axes with constant rotation rates. Assuming the same area loading for spheres and plates leads to lower average effective areas for plates than for spheres. This results from the fact that the magnitude of the radiation pressure acceleration depends on the cross sectional area normal to the incident radiation. To make the evolution of a population of spheres comparable to that of a population of plates, the area-to-mass ratio for spheres is scaled down. The scaling factor will

be estimated following the definition of the initial population. The propagated populations are then evaluated with respect to their distribution in inclination vs. right-ascension of ascending node and in eccentricity vs. semi-major axis at the end of the simulation period.

6.5.1 Initial population

A subset of the objects of the MASTER-2009 MLI population from the snapshot of May 1^{st}, 2009 is used as initial population. GEO and GTO surveys performed with ESA's SDT since 2004 consistently revealed HAMR objects of which most exhibited mean motions concentrated around that of GSO objects (Schildknecht et al. 2005, 2010, Schildknecht 2007). To better understand the observations made by Schildknecht et al., only objects from the population are considered which have a characteristic length larger than 10 cm and whose semi-major axis is within 1,000 km of the GSO altitude of 42,164 km. The distribution of initial orbit parameters of the 148 objects which satisfy these criteria in the initial population is shown in the top two plots in Figure 6.17. The lower plot shows the area loading in terms of area versus mass. The two distributions for cover layer MLI and reflector layer MLI as described in the previous sections are clearly visible.

6.5.2 Average Illuminated Area

The magnitude of the acceleration due to solar radiation pressure depends on the projected area of the object which is perpendicular to the incident light from the Sun. In order to be able to compare the evolution of spherical and plate-like objects, the average illuminated cross sectional areas must be similar. It is decided to derive the size of the spherical objects from the area of the plates by multiplying their area by a scaling factor F_{tumbling}. For the MASTER-2009 MLI model the plates were assumed to rotate at identical rates about two perpendicular axes. This resulted in $F_{\text{tumbling}} = 0.5$ (see Section 5.2). In actuality the reduction factor may take on any value between 0 and 1 and depends on the orientation and the rotating motion. Here, the factor is derived for the case of plates with inertially fixed orientation and for the case of inertially fixed rotation axes. For the first case, all objects in a population are assigned random orientations which are inertially fixed. For the second case, the objects have random initial orientations and random inertially fixed rotation axes with constant rotation rates. The average

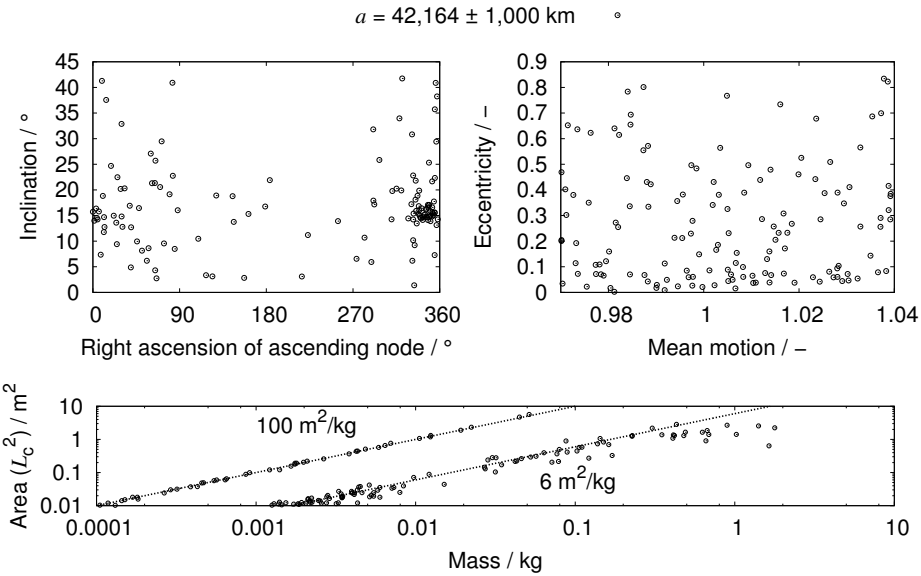

Figure 6.17: Orbit and area loading distribution of initial statistical HAMR object population. The objects centered on an area loading of $6\,\mathrm{m}^2/\mathrm{kg}$ are cover layer MLI while objects with an area loading around $100\,\mathrm{m}^2/\mathrm{kg}$ are reflector layer MLI.

projected area is then calculated over one year. The reduction factor F thus is simply the ratio of the average projected area and the area of the plate.

As initial population, all MLI objects larger than 10 cm from the snapshot May 1^{st} 2009 from MASTER-2009 is used leading to a total of 5750 objects. Figure 6.18 shows the distribution of $F_{\text{fixed plate}}$ and $F_{\text{rotating plate}}$ respectively. Both distributions are very similar. The reason for this is that within the simulation time span of one year, inertially fixed plates perform one complete rotation relative to the Sun-object line of sight. With respect to the illumination source, these objects therefore behave similar to other rotating plates. Most objects have an average illuminated area which is smaller than $2/\pi$. This value is attained for instance by objects which rotate about an axis which is normal to the ecliptic and is in the object's surface plane. A derivation of this factor is given in Appendix F. The

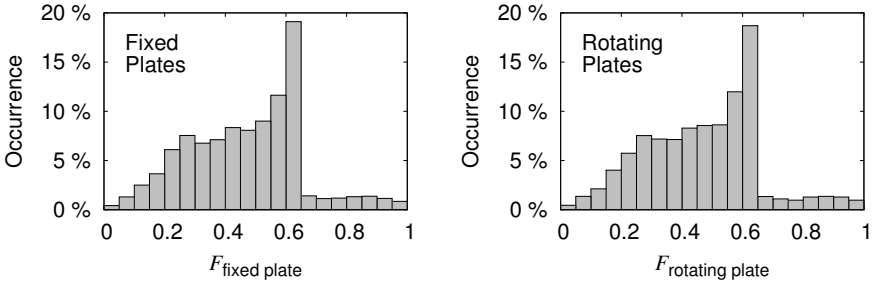

Figure 6.18: Relation of average annual illuminated area to single side surface area. Left: plates with inertially fixed orientation. Right: plates with random initial orientation and inertially fixed rotation axes.

overall mean value is identical for both scenarios: $\bar{F}_{\text{plate}} = 0.47$ which is very similar to the value which was used for the MASTER-2009 models. In the following section, the area-to-mass ratio (which is proportional to the area) of all spherical objects is calculated by multiplying the area of the flat plates by this factor. In the upgraded MLI model discussed in Section 7.2, a more accurate description will be used however.

6.5.3 Comparison of simulation results

The objects from the initial population of cover and reflector foils presented in Section 6.5.1 are propagated from 2009 to 2059 using spheres and plates as previously outlined. For estimating the effect of tumbling objects, constant rotation rates are applied which are distributed uniformly on a logarithmic scale between $10^{-5}\,^{\circ}$/s and $1\,^{\circ}$/s. Although $1\,^{\circ}$/s may seem slow, it was shown in Section 6.4 that discernible variations in the orbit evolution actually become apparent only below rates of $10^{-4}\,^{\circ}$/s. The specular and diffuse reflectivity of all plates is assumed to be identical at $\rho_s = \rho_d = 0.313$. The reflectivity coefficient for spherical objects is derived according to Equation 6.17 using the same values: $C_{R\,\text{sphere}} = 1.522$.

The quarterly population snapshots from the years 2049 to 2059 are overlaid. This was done primarily due to the low number of objects in the initial pop-

ulation. As a result the plots not only show the distribution of objects at the end of the propagation but also include some information on the orbit evolution of individual objects. Data points belonging to the same object create tracks in the graphs as long as orbit changes remain similar over several snapshots. Simulations are evaluated with respect to eccentricity versus semi-major axis and inclination versus right ascension of ascending node.

Eccentricity vs. Semi-major axis The eccentricity versus semi-major axis simulation results for the three scenarios are presented in Figure 6.19. Eccentricities below 0.4 are dominated by objects with area-to-mass ratios lower than $5\,\mathrm{m}^2/\mathrm{kg}$ which corresponds to cover layer MLI. Higher eccentricities are mainly represented by reflector layer MLI with area-to-mass ratios in the region of 30 to $50\,\mathrm{m}^2/\mathrm{kg}$. The top graph shows the simulation results for spherical objects. Cover layer MLI creates vertical tracks which illustrates that direct solar radiation pressure has little effect on the orbit energy as long as the acceleration vector always points away from the Sun. The initial population exhibited the same general distribution between high and low eccentricity objects. With the transition to plate-like objects, a changed behavior in semi-major axis and eccentricity is observed. The resulting mix of vertical, horizontal and curving streaks are visualizations of the change in orbit energy.

More interestingly for the overall distribution is the fact that at the high eccentricity end, the distribution of objects seems to differ between the studied cases (compare Figure 6.20). While the overall distribution in eccentricity is the same, fewer objects attain eccentricities above 0.5 ($10^{-0.3}$) while more objects have eccentricities around 0.3 ($10^{-0.5}$) compared to spherical objects. From the figure it becomes apparent that this is caused primarily by reflector layer MLI. Plate-like reflector layer MLI exhibit more circular orbits than spherical objects of the same class. This effect was also seen in Section 6.4 for objects with out-of-plane orientation components (Figure 6.11).

Inclination vs. RAAN Figure 6.21 compares the distribution of the spherical, the oriented and the rotating objects in inclination and RAAN. The number of objects located near $0\,^\circ$ RAAN at inclinations near $15\,^\circ$ is similar for all studied cases. The two graphs in Figure 6.22 show that this region is dominated by cover layer foils. For the relatively low area-to-mass ratios of these objects, the SRP accelerations are on the same order of magnitude as Luni-solar perturbations. Dif-

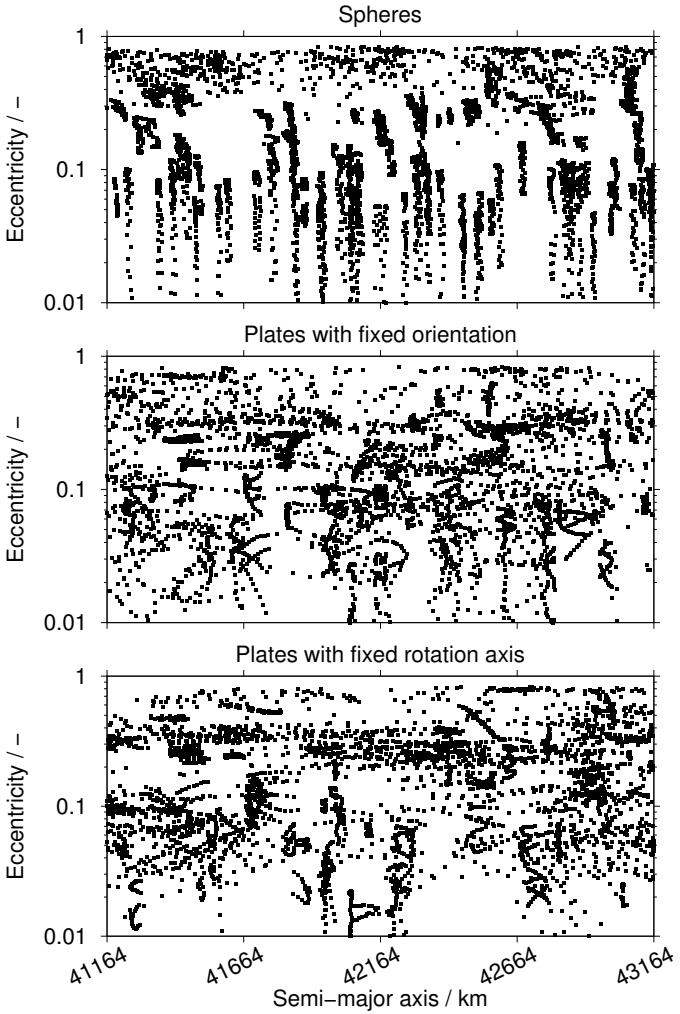

Figure 6.19: Eccentricity vs. semi-major axis of propagated population with $a = 42{,}164 \pm 1000$ km. Results from years 2049 to 2059 merged. Top: spheres. Middle: oriented plates. Bottom: rotating plates.

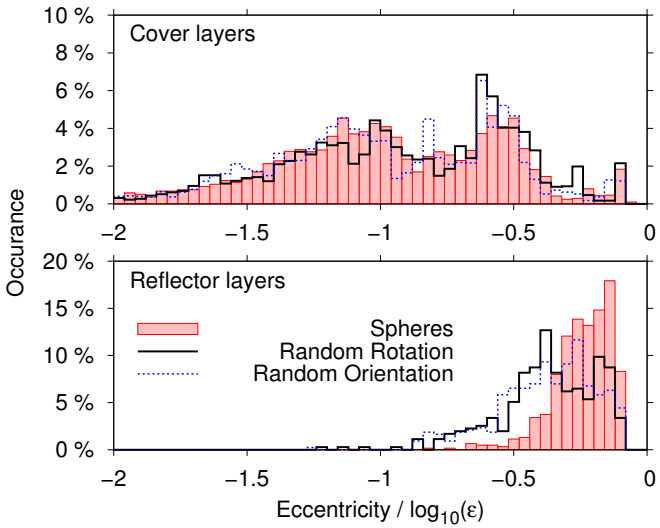

Figure 6.20: Eccentricity distribution of propagated population with $a = 42{,}164 \pm 1000$ km. Results from years 2049 to 2059 are merged.

ferences between the simulation results are visible primarily at high inclinations where reflector layer MLI dominate and SRP accelerations are much higher than the gravitational attractions of the Sun and Moon. For oriented plates, no objects are present in the central region above $i = 20\,^\circ$. Spherical and rotating plates however both contribute here. The regions closer to zero RAAN above $30\,^\circ$ up to $45\,^\circ$ inclination at least is evenly populated by spherical objects while plate-like objects exhibit sparser distributions. Especially for inertially fixed plates, this correlates with the findings of Section 6.4.3 (Figure 6.12) where the maximum inclination was found to be generally lower than for a comparable spherical object. The streaks in Figure 6.21 are produced mainly by cover layer foils while the orbits of reflector layers vary more rapidly and are displayed rather as a series of incoherent points.

The bottom plot in Figure 6.22 shows that reflector layers especially are encountered at high inclinations. These very high inclination objects are also present in

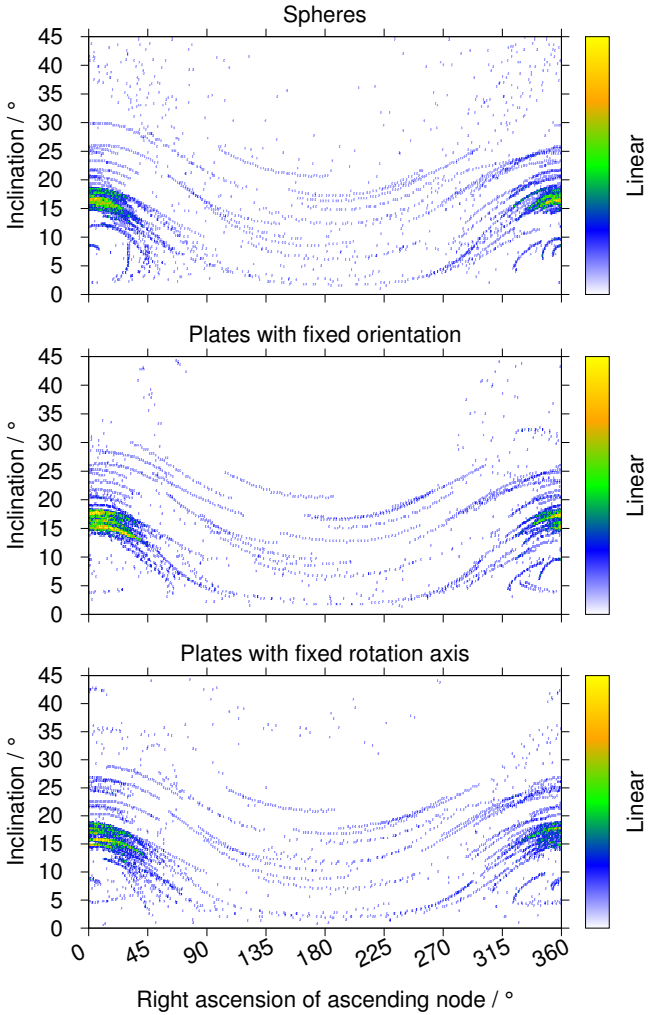

Figure 6.21: Inclination vs. RAAN of propagated population with $a = 42{,}164 \pm 1000$ km. Results from years 2049 to 2059 are merged. Top: spheres. Middle: oriented plates. Bottom: rotating plates.

the initial population. Their creation can be traced back to an inconsistency in the continuous MLI source model in which new objects were ejected with a velocity of 1 km/s instead of 1 m/s from the parent object. This issue is discussed in the later sections and remedied in the updated model. Unlike the eccentricity histogram, no systematic differences can be observed for the distribution in inclination.

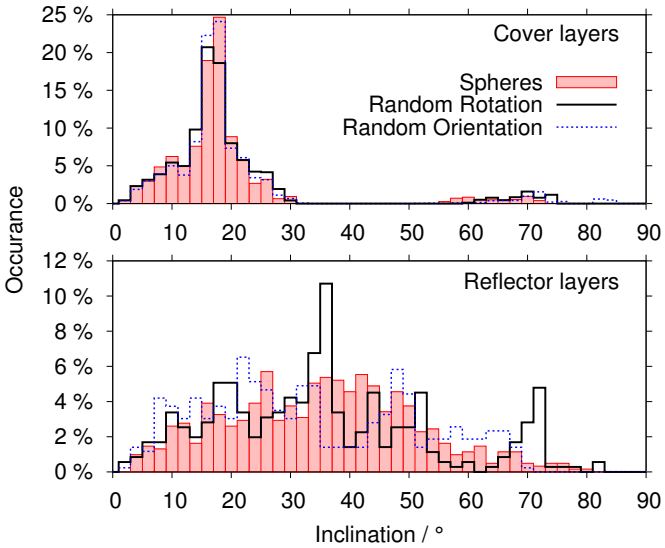

Figure 6.22: Inclination histogram of propagated population with $a = 42{,}164 \pm 1000$ km. Results from years 2049 to 2059 are merged.

6.6 Conclusions of Orbit Perturbation Effects

In this section, a broader view will be given of the results from the previous sections in an attempt to put the individual findings into a larger context.

6.6.1 Spherical HAMR Objects

The lowest area-to-mass ratio looked at here is $1\,m^2/kg$. Spherical objects upwards of $48\,m^2/kg$ deorbit within a few years. Observations of the ESA-SDT show that objects with effective area-to-mass ratios as high as $86\,m^2/kg$ are observed (Schildknecht et al. 2010). In their publication, Schildknecht et al. report on a HAMR object catalog. The number of objects contained in the catalog depends on the number of newly found objects and objects which were lost. Since orbit eccentricities up to 0.8 are reported it stands to reason that at least some of the HAMR objects are lost due to the their orbital demise.

Maximum values in inclination and in eccentricity as well as maximum deviation of semi-major axis from GSO increase monotonously towards larger area-to-mass ratios. Maximum inclination increases linearly from $15\,^\circ$ to $55\,^\circ$. Eccentricity follows a square law dependency between 0.02 and 0.8. Semi-major axis deviations from the GSO altitude increase linearly with area-to-mass ratio for the most part. Maximum deviation ranges from 35 km to about 700 km. Precession and eccentricity oscillation periods decrease with area-to-mass ratio. The inclination is coupled directly with right-ascension of ascending node through the precessing of the orbit around a pole defining a modified Laplace plane. Periods reach down to about 5 years starting at 53. For eccentricity, the period varies between 0.9 and 1.02 years.

For semi-major axis, three effective area-to-mass regions were identified: Up to $5–8\,m^2/kg$, libration about stable points dominates. For the chosen initial condition, the libration exhibits a period of a few years. This value depends on the object's initial longitude position and is a result of the Earth's mass distribution along its equator. A region of secular orbit change ranges from $8\,m^2/kg$ to $25\,m^2/kg$. An annual oscillation with an amplitude on the order of 100 km forms. This variation occurs when the object's orbit intersects the Earth's shadow. For the chosen initial conditions, this takes place twice per year. For higher ratios, the annual oscillation is fully developed. A superimposed beat with a period of 8 to 9 years is observed. The overall mean semi-major axis may deviate from the initial GSO altitude.

6.6.2 Oriented and Rotating HAMR Plates

The orbit evolution of plates with fixed orientation is influenced significantly by the orientation. While some orbit components may undergo large changes characteristic of HAMR objects, other parameters may remain small in comparison to spherical HAMR objects. While the orbit evolution of rotating objects differs from that of the other cases, the rotation rate itself has no effect on the long-term development except when resonance cases take effect. The object analyzed here had an area-to-mass ratio of $28\,\mathrm{m}^2/\mathrm{kg}$ with diffuse and specular reflectance of $\rho_d = \rho_s = 0.313$.

Analogy with spheres Whenever the illuminated area changes slowly throughout a year, the eccentricity evolution deviates from the repeating inverted parabolic pattern. Oriented plates as well as objects with out-of-plane rotation components exhibit either a pronounced 'double hump' (Figure 6.9) or a 'single hump' in which the eccentricity does not necessarily return to the original value after one cycle (Figure 6.11). For plates with fixed orientation, the semi-major axis can vary between a few hundred and about 3000 km in 27 years. Variations for non-resonant rotating plates remained on the order of a few hundred kilometers.

Table 6.4 compares important parameters for an object with an area loading of $m/A = 36\,\mathrm{g/m}^2$. Taking into account the reduction factor $\bar{F}_{\mathrm{plate}} = 0.47$ (Section 6.5.2) as well as the reflectivity coefficient $C_{R\,\mathrm{sphere}} = 1.522$ (Section 6.17), this corresponds to a sphere with an effective area-to-mass ratio of $20\,\mathrm{m}^2/\mathrm{kg}$. In general, the maximum values in inclination, eccentricity and *annual* semi-major axis variations appear to be influenced directly by the orbit-planar and orbit-normal accelerations. Larger normal components i.e. through orientation or rotation lead to high maximum inclination values and lower annual eccentricity and semi-major axis variations. High orbit-planar components invert the result. The spherical case values represent the limiting values for maximum inclination, minimum precession period and for maximum eccentricity of rotating plates. It is interesting to note that in most cases, the *annual variations* in orbit parameters of plates are *smaller* than those of comparable spheres.

Departure from sphere analogy Especially for rotating objects, it is interesting to note that out-of-plane rotation in the studied cases leads to larger long-term deviations in the semi-major axis than the in-plane rotation. The precession pe-

Table 6.4: Comparison of HAMR object evolution for $A/m \approx 28\,\mathrm{m}^2/\mathrm{kg}$ for plates and $A/m \cdot \bar{F}_{\mathrm{plate}} \approx 13\,\mathrm{m}^2/\mathrm{kg}$ for spheres.

	Sphere	*Oriented Plate*	*Rotating Plate*
Maximum inclination	31 °	17 – 31 °	21 – 37 °
Maximum eccentricity	0.4	0.15 – 0.65	0.32 – 0.4
Semi-major axis variation	200 km	100 – 3200 km	$<$ 1000 km
Precession period	23 a	20 – 46 a	20 – 36 a

riod decreases from 53 years with increasing effective area-to-mass ratio. The value of 23 years for a sphere with effective area-to-mass ratio of $20\,\mathrm{m}^2/\mathrm{kg}$ is similar to the extreme values for oriented and rotating plates. Opposite to the inclination of the modified Laplace plane however, the precession period is effected the most when *out-of-plane* components are *smallest*.

6.6.3 Population Evolution

The overall trend seems to suggest that the number of objects with near GSO mean motion decreases over time and that this trend is enhanced for non-spherical objects. Annual variations in semi-major axis are smallest for rotating objects. The inclination distribution of cover layer MLI is very similar for spherical and plate-like objects. This suggests that the main perturbation effect is not radiation pressure but third body perturbation. This is supported by the observation that the semi-major axis variation of objects with effective area-to-mass ratios below 5–8 m^2/kg was dominated by the east-west libration which is caused by the non-circular Earth equator. The principle distribution of reflector layer objects in inclination is similar for the three scenarios. Spherical objects show the smoothest distribution which could be explained by their lower precession period compared to plates (Table 6.4). Out-of-plane orientation components reduce the effects on eccentricity build up, so that HAMR objects generally have more circular orbits than spherical ones.

In conclusion, cover layer MLI with area-to-mass ratios below $10\,\mathrm{m}^2/\mathrm{kg}$ seem to be well represented by spherical objects with regard to inclination and eccen-

tricity distribution. Reflector layer MLI show some discrepancies especially in eccentricity owing to out-of-plane orientation components. Variations in semi-major axis are about an order of magnitude larger for fixed and rotating plate-like objects than for spheres. The differences are however still small enough that this should have only a slight effect on collision velocities with active GSO payloads.

6.7 Outlook

This section takes a brief look at effects which have not been taken into account but which could have a significant influence on the orbit evolution.

Moon shadow Since secular orbit changes occur whenever HAMR objects traverse the Earth's shadow, it stands to reason that the Moon's shadow could have a similar effect. The Moon's distance of about 384,400 km to the Earth and its small radius of about 1738 km lead to an umbra in GEO which is much smaller than the Earth's. The widest eclipse path on the Earth's surface during solar eclipse is no more than 270 km (Comins and III 2000). This in turn reduces the likelihood of an object repeatedly transiting the shadow and thus also the overall effect.

Euler's equations of motion Introducing more complicated motions with nutation and precession would result in different modes of orbit evolution and also a different variety of resonance cases. It is unlikely however that the amplitude or short- and long-term oscillation periods would differ much from the cases investigated here so that the effect on large HAMR populations should have been adequately captured.

Optical material properties In this work, the optical properties of both sides of the MLI plates were identical which should be realistic for the reflector layer MLI. Since most fragments of MLI are believed to originate in fragmentation events, and reflector layers outnumber cover layers by about a factor 10, this could be a valid assumption for many objects. Introducing second surface mirrors for the cover layer MLI could have a noticeable effect for objects with fixed orientation or a rotation axis leading to similar orientations. Rotating objects should behave similar to the ones looked at here. An interesting effect could be introduced if the optical properties were to change over time i.e. through aging effects. Ground

tests show that a reduction in reflectivity by about a factor 2 can occur over time (Kelecy and Jah 2011, Fischer 2011). The orbit variations due to direct solar radiation would therefore likely decrease with time. Thermal emission for objects with different optical properties on either side could cause objects with fixed orientation to exhibit new orbit evolution patterns.

Earth albedo and infrared radiation Approximately 30 % of the Sun's radiation is reflected as albedo. The remaining radiation is absorbed and emitted at a later time as infrared radiation with a power output of about $237\,\mathrm{W/m^2}$ at the Earth's surface (Vallado and McClain 2007). The infrared radiation is independent of the position of the Sun. The exact amount of reflected and absorbed light depends on the amount of clouds, the Earth surface properties (i.e. water, land, snow) and the offset from the sub solar point on the Earth. The power per unit area radiated from the Earth decreases with the square of the distance. The Earth's shadow and the Earth albedo are geometrically coupled. Neglecting uneven power output from albedo as a first order approximation, the mechanism behind perturbative accelerations could be similar to those from the Earth's shadow. The overall effect from albedo is however estimated to be very small since the amount of reflected light is only a fraction of the incoming solar radiation. This is undermined by Vallado and McClain (2007) pp.708 where it is shown that for LEO objects, albedo effects are an order of magnitude below direct solar radiation and the effect diminishes for objects in GSO.

Coupling effects Investigation of coupling effects such as a possible dependency between the period of the annual semi-major axis variations and the RAAN drift could give further insight into the mechanics of HAMR object orbit evolution.

Chapter 7

MLI Model Update

In the final stages of the ESA contract "Maintenance of the ESA *MASTER* Model" which led to the release of the model in its current version (MASTER-2009), a seemingly inconsistent escalation of the number of in-orbit MLI debris was observed which set in after the reference epoch of May 1st of 2009. The models predicted that in a business-as-usual scenario, over 40,000 MLI objects larger than 10 cm would be in orbit in 2060 (see Figure 7.1). This is about the same amount as all other debris sources combined for the same size range. The cause for this was traced back to the model which simulates the continuous release of MLI. For MASTER-2009 it was decided to publish only the MLI population leading up to the reference epoch which had been validated against observations made by the ESA-SDT.

After the release of MASTER-2009, a complete reevaluation of the two MLI models was performed which will be detailed in the current chapter. Initially, an update is presented for the estimation of the area of a spacecraft which is covered by MLI. The chapter continues with a description of updates to fundamental aspects in the derivation of the effective area-to-mass ratio and to the fragmentation source model. An investigation of the continuous source model is performed which prompts the exclusion of the model from further simulations of MLI debris. The chapter closes with a description of the MLI population between 1957 and 2060 resulting from the updated modeling approach.

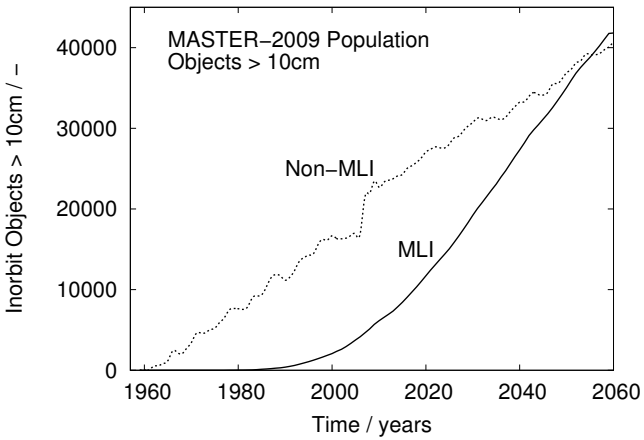

Figure 7.1: Escalation of MASTER-2009 MLI population above 10 cm for future epochs.

7.1 MLI Applications on Spacecraft

For the updated model, a standard MLI stack is assumed to consist of 20 layers. This is an increase compared to the MASTER-2009 model assumption of 12 layers which is still in line with values published in NASA's MLI Guidelines , the EuReCa spacecraft and information obtained through personal communication (Finckenor and Dooling 1999, Stadermann et al. 1997, Steiner 2013).

The average area of a spacecraft which is covered by MLI is reevaluated based on data taken from ESA's **D**atabase and **I**nformation **S**ystem **C**haracterising **O**bjects in **S**pace (DISCOS) (European Space Operations Centre 2010). Historically rocket bodies were often not covered with MLI but rather had painted metal outer casings. For this reason, only data for satellites is used. Rocket bodies are not considered in the creation of MLI debris with the exception of the Titan III Transtage for which an independent estimation is performed in Section 7.3.3. Satellites with identical minimum and maximum cross sectional areas were excluded. These satellites are either spherical spacecraft such as the Laser Relativity Satellite (LARES) which do not use MLI on the external surface or are spacecraft with insufficient geometrical data. Spacecraft with masses above 9 t

were also removed from analysis as these are typically manned missions which do not contribute to MLI debris. The minimum cross sectional area was used so as to exclude the influence from solar arrays on the surface area. The geometry of all satellites is assumed box shaped where all six sides have the same area as the minimum cross sectional area. As an estimate of the satellite bus surface area, the minimum cross sectional area was multiplied by six. The resulting data along with the equation derived for MASTER-2009 (Equation 5.1) based on a more limited data set and a fit to the current data are shown in Figure 7.2.

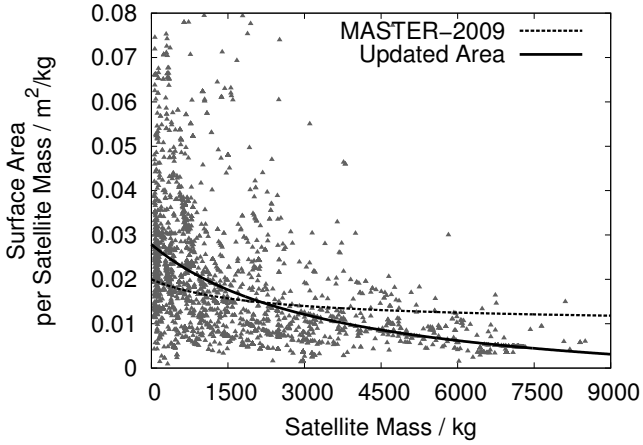

Figure 7.2: Surface area per kilogram of spacecraft mass versus spacecraft mass. Data taken from ESA's DISCOS (European Space Operations Centre 2010).

The north and south facing sides of three-axis stabilized GEO satellites are typically covered with radiators while MLI covers the remaining four surfaces. Equation 7.1 replaces the previously derived equation 5.1. The new equation predicts more MLI surface area for satellite masses below about 3.7 t and less area for heavier ones.

$$\frac{A_{\text{satellite bus}}}{m_{\text{satellite}}} = \frac{2}{3} \cdot 11.2179 \cdot \left(-0.000596311 + \frac{10.9932}{m_{\text{satellite}} + 3567} \right) \tag{7.1}$$

Applying this equation to the EuReCa spacecraft which was used as an example in Section 5.1 returns 25.79 m^2 as total area which would be covered by MLI. This

is slightly less than the 29.37 m^2 which is predicted by Equation 5.1 and still well within the limits set by the estimations based on geometric data of the satellite's bus.

7.2 Effective Area

A renewed look is taken at the parameters of Equation 5.2 describing the reduction in the solar radiation pressure compared to a flat plate oriented perpendicularly to the Sun. Equation 5.2 is restated here as reminder:

$$A_{\text{eff}} = A_{\text{flat}} \cdot F_{\text{reflectivity}} \cdot F_{\text{deformation}} \cdot F_{\text{tumbling}} \tag{7.2}$$

7.2.1 Deformation

The ground tests performed at Kyushu University are used as basis for the *fragmentation source debris* in this update. Table B.1 lists the area-to-mass ratio of the fragments from two ground tests performed at Kyushu University (Murakami 2008). Fragments are given separately for each of the two tests performed and grouped into fragments of cover foil, reflector foil and complex fragments which consist of multiple layers. The values were manually extracted from histograms presented in Murakami's work. Caution is however required when interpreting the presented data. Three fragments in the test titled 'Shot R' were allotted area-to-mass ratios above 600 m^2/kg. Theoretically, the highest value should not exceed that of the flat pristine material which is 28.57 m^2/kg for the cover layer material and 88.50 m^2/kg for the reflector layers. These three fragments are discounted from the results. The highest value for measured area-to-mass ratios thus is 251 m^2/kg which is still much higher than the theoretical maximum. Table 7.1 gives the averaged results for both tests for cover foil, reflector foil and complex multi-layer fragments.

For the two tests, no clear consistency can be observed when comparing the retrieved average values to the values for the pristine material for inner-, outer- and complex fragments. For each fragment type, the average value is in one case lower and in the other case higher than that of the pristine values. Taking the mean value for each fragment type for the two tests leads to consistently lower area-to-mass ratios than the original material: for outer layer MLI fragments, the mean value is reduced by 2.33 %, for inner layer MLI fragments by 1.13 % and for

Table 7.1: Area-to-mass ratio distribution of fragments from ground tests performed by Murakami (2008). Full table is given in Appendix C. All area-to-mass ratio values are given in m^2/kg

	Number of MLI fragments					
	Shot F			*Shot R*		
	Inner	*Outer*	*Complex*	*Inner*	*Outer*	*Complex*
Sum:	62	60	19	32	55	4
Mean A/m:	76.73	23.34	9.60	98.27	32.47	2.55
Pristine A/m:	88.50	28.57	6.82	88.50	28.57	6.82
$\Delta A/m$ in %:	-13.29	-18.30	+40.78	+11.04	+13.64	-62.68

complex fragments by 10.95 %. Due to the high apparent uncertainty in the measurement data, it does not seem to make sense to model effective area-to-mass ratio via a fitted normal distribution. Such a distribution would create too many objects with unrealistically high ratios. Instead it is assumed that deformation of fragments leads to a reduction in effective area which is uniformly distributed between 0 % and 5 %. $F_{\text{deformation}}$ is thus uniformly distributed between 0.95 and 1.00 meaning that simulated MLI fragments retain a plate-like shape.

7.2.2 Tumbling

The reduction in average illuminated area for plate-like debris due to fixed orientation or randomly oriented rotation axes has been studied in Section 6.5.2. It can be assumed that the reduction in average illuminated area matches that presented in Figure 6.18. F_{tumbling} is assigned using a fit to the distribution of rotating plates. The selected probability density function is shown in Figure 7.3.

7.2.3 Reflectivity

UV-, electron- and proton-radiation are major factors which cause the reflectivity of MLI foils to asymptotically approach a reduced value. Chapter 3 gives an account of publications dealing with the optical degradation of insulating materials exposed to the space environment. The penetration depth of radiation into a material depends on factors such as the target material density, the type of radiation and the energy of the radiation. Marco and Remaury (2004) analyzed the

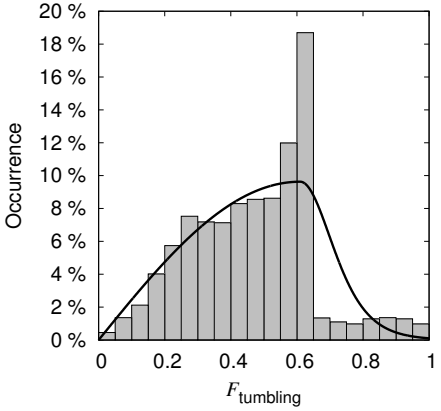

Distribution Parameter	$F_{tumbling}$ /–
c	0.2
Approach Onset	sin
Δx_0	0
$\Delta x_0 + \delta x_1$	0
$\Delta x_0 + \Delta x_1$	0.61
Approach End	$1/\cosh^2$
$\Delta x_0 + \Delta x_1 + \delta x_2$	0.8
$\Delta x_0 + \Delta x_1 + \Delta x_2$	1.0

Figure 7.3: Probability density distribution for F_{Tumbling}.

dose profile from electrons and protons versus penetration depth for an object in GEO. The deposited dose decreased by an order of magnitude within the top micrometer and by another order of magnitude within the next 10 micrometers of the material. High energy electrons exhibited the highest penetration depth of up to about 400 μ. For a cover layer with a thickness between five and 10 mil, the dose deposited in the first reflector layer of an intact blanket would be roughly three orders of magnitude lower than that deposited in the top micrometer of the cover layer. It is postulated that most of the foil within a blanket will have been well protected by the upper layers of the blanket so that on average, the optical properties will be close to the pristine properties when they are released in a fragmentation event. The optical properties of the single layer MLI fragments especially will then be highly susceptible to degradation and degrade quickly towards an asymptotic end value.

For the model, it is assumed that a fragment's reflectivity will remain constant after its release from the parent object. Post release degradation is expected to have a small effect on the overall distribution of MLI debris although it may significantly influence the orbit evolution of individual objects. This effect should be studied in future work. The reflectivity of each object is averaged from its initial value ρ_0 and the degraded reflectivity ρ_{degraded} which is approached in an

asymptotic manner. An uncertainty $\rho_{\text{variation}}$ is introduced based on variations found in laboratory and in-situ measurements:

$$\rho = \frac{\rho_0 - \rho_{\text{degraded}}}{2} + \rho_{\text{variation}} \tag{7.3}$$

All reflectivity values refer to the solar reflectance ($\rho_\odot$). The index $\odot$ has been omitted for ease of reading. Values for the pristine and degraded material are taken as presented in Sections 3.3 and 3.4. These are $\rho_0 = 0.87$ and $\rho_{\text{degraded}} = 0.33$ respectively. The value for the variation is derived subsequently followed by the definition of the reflectivity factor $F_{\text{reflectivity}}$.

Estimating variation Reflectivity is varied within uncertainty boundaries of $\rho_{variation} = \pm 0.04$. This is in line with the uncertainties of the ground measurements as well as the variation in the mean values of the in-situ measured BOL parameters shown in Table 3.3.

Implementation The simplified equation for acceleration due to direct solar radiation pressure on a spherical object is directly proportional to the reflectivity coefficient C_R and the area-to-mass ratio. The complete equation including the reduction factors is written as:

$$\boldsymbol{a}_{\text{RP}} = -S_\odot \frac{\Phi_\odot}{c} C_R \left(\frac{A_{\text{flat}}}{m_{\text{obj}}} F_{\text{reflectivity}} F_{\text{deformation}} F_{\text{tumbling}} \right) \hat{\boldsymbol{s}}_\odot \tag{7.4}$$

The other parameters in this relation have been detailed in Equation 2.6. For propagation, all MLI objects are given a default reflectivity coefficient C_R. The reflectivity factor $F_{\text{reflectivity}}$ simply replaces the default C_R value by an object dependent one (C_R'). With ρ being an object specific value for the reflectivity (note that the index $\odot$ is omitted for simplicity), this leads to the formulation:

$$F_{\text{reflectivity}} = \frac{C_R'}{C_R} = \frac{1+\rho}{C_R} \tag{7.5}$$

With $C_R = 1.3$, and inserting the derived values into Equation 7.3, $F_{\text{reflectivity}}$ would have a valid interval of [1.20,1.26].

7.3 MLI Fragmentation Model

In MASTER-2009 5 % of the total available MLI area was converted into single layer fragments by the MLI fragmentation model. The remaining MLI was assumed to remain fairly intact in so-called *complex fragments*. As the area-to-mass ratio of these fragments is much lower than that of single sheet MLI, the equivalent mass was handed over to the NASA Breakup Model which also accounts for fragments from lightweight phenolic material and was assumed to be similar to that of complex MLI fragments. In this section a simple model for these MLI fragments is introduced. The 5 % limit of MLI to be used for single layer fragments is revised based on ground test results from Murakami (2008). As a core upgrade of the MLI fragmentation model, the fragment sizes of complex and single layer MLI fragments are now coupled to the size of the parent object. This is indicated in the updated fragmentation model schematic shown in Figure 7.4 by the connecting arrow between the satellite mass and the debris characteristic length. Of the two acknowledged fragmentations in GEO, one involved a Titan III Transtage. A very simple model is proposed to give a first order estimation for the orbit distribution of steel foil insulation debris from Titan III Transtage fragmentations. Finally, a plausible estimation of the velocity change is proposed which MLI objects experience through the transfer of kinetic energy during a fragmentation event.

7.3.1 Complex Fragments from Spacecraft

The amount of MLI which is bound in complex fragments is estimated based on the ground tests published by Murakami (2008). In test 'F' and 'R', roughly three and four of the five sides which were covered with MLI remained largely intact. In terms of area, this relates to between 60 % and 80 % of the MLI covered surface which resulted in complex fragments. In the simulations it is assumed that two of the six sides of a typical spacecraft are not covered with MLI due to the presence of radiators and instrumentation. Following the above observation, it is further postulated that three of the four remaining surfaces (75 %) dissociate into complex fragments. The total area available for creation of complex fragments within the simulation is thus expressed using the fraction F_{complex} of the

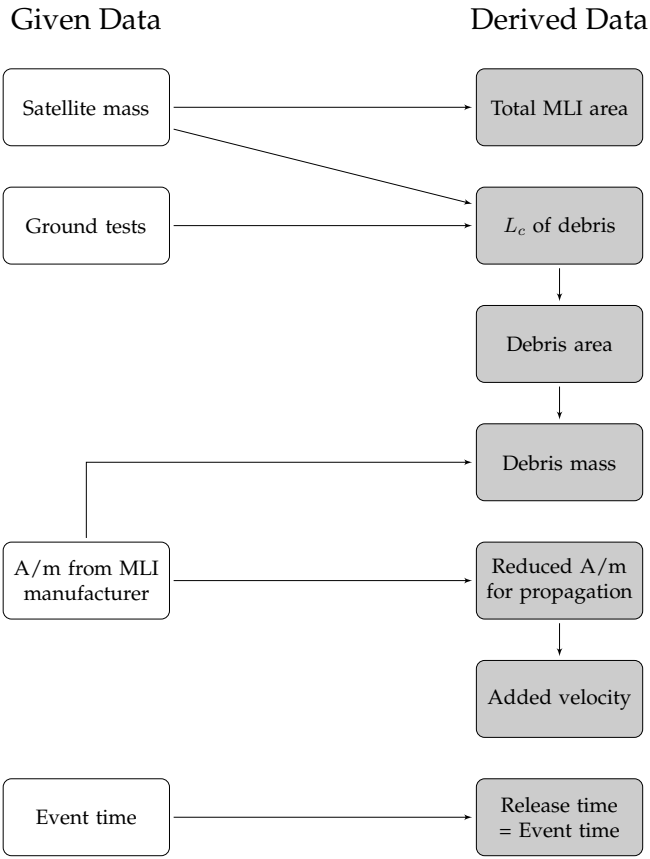

Figure 7.4: Structure of the updated MLI fragmentation model.

total MLI covered area which is bound in complex fragments:

$$A_{\text{tot,complex}} = F_{\text{complex}} \cdot \left[\left(\frac{A_{\text{satellite bus}}}{m_{\text{satellite}}} \right) \cdot m_{\text{satellite}} \right] \tag{7.6}$$
$$F_{\text{complex}} = 0.75$$

$A_{\text{satellite bus}}/m_{\text{satellite}}$ is given by Equation 7.1. Due to the very low number of complex fragments created in an event a very simple approach is chosen to assign

fragment sizes. The length of the edge of an assumed cube-shaped spacecraft is used as the limiting upper characteristic length. To this end the square root of the area of one panel given in Equation 7.1 is taken. The lower limit is set to half of the largest characteristic length and a uniform distribution of sizes is assumed:

$$L_{c,\text{upper limit}} = \left[0.25 \cdot \left(\frac{A_{\text{satellite bus}}}{m_{\text{satellite}}}\right) \cdot m_{\text{satellite}}\right]^{1/2} \tag{7.7}$$

$$L_{c,\text{lower limit}} = 0.5 \cdot L_{c,\text{upper limit}} \tag{7.8}$$

The overall area-to-mass ratio of the fragments is determined by first assigning specific area-to-mass ratios to the two cover layers and to the 18 reflector layers. The area-to-mass ratio of complex fragments is thus determined by:

$$\left(\frac{A}{m}\right)_{\text{complex}} = \left[2 \cdot \left(\frac{A}{m}\right)^{-1}_{\text{cover}} + 18 \cdot \left(\frac{A}{m}\right)^{-1}_{\text{reflector}}\right]^{-1} \tag{7.9}$$

7.3.2 Single Layer Fragments from Spacecraft

The fragment size distribution derived from the data given in Murakami (2008) is used as a baseline (see Figure 5.3). For the current model it is assumed that the smallest fragments in any fragmentation event will be of the same size as those found in the ground tests. The largest fragments of single layer MLI had side lengths, which were the same as one of the test satellite's side panels. In the model, the upper limit is scaled to the size of the parent spacecraft. The limiting characteristic length is fixed by the panel edge length of an assumed cube-shaped spacecraft. The characteristic length of each fragment L'_c is then scaled linearly according to the following relation:

$$x'(x) = x_0 + (x - x_0) \cdot \left(\frac{x_{2,\text{SC}} - x_0}{x_2 - x_0}\right) \tag{7.10}$$

L'_c	Scaled characteristic length	m
L_c	Characteristic length	m
x	$\log_{10}(L_c)$	$\log_{10}$ (m)
x'	$\log_{10}(L'_c)$	$\log_{10}$ (m)
x_0	Δx_0 from the table in Figure 7.5	$\log_{10}$ (m)
x_2	$\Delta x_0 + \Delta x_1 + \delta x_2$ from the table in Figure 7.5	$\log_{10}$ (m)
$x_{2,\text{SC}}$	$\log_{10}$ of length of panel edge of assumed cube shaped spacecraft where panel area is derived using Equation 7.1	$\log_{10}$ (m)

The graph in Figure 7.5 shows the inverted probability distribution in characteristic length for three different panel edge lengths and gives the unscaled distribution parameters.

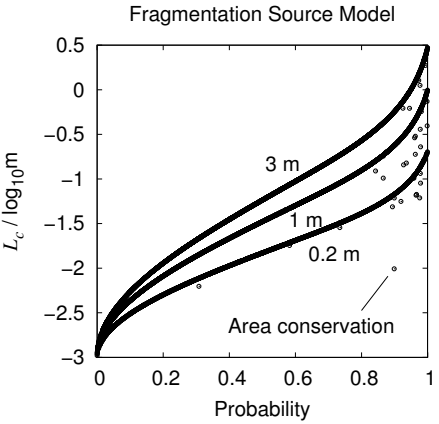

Distribution Parameter	$\log_{10} L_c$ / $\log_{10}$ m
c	0.0001
Approach Onset	sin
Δx_0	-3
$\Delta x_0 + \delta x_1$	-3
$\Delta x_0 + \Delta x_1$	-1.7
Approach End	$1/\cosh^2$
$\Delta x_0 + \Delta x_1 + \delta x_2$	1.5
$\Delta x_0 + \Delta x_1 + \Delta x_2$	-0.7

Figure 7.5: MLI fragmentation model. Left: Inverted probability distribution for fragment characteristic lengths. Results shown for a panel-edge length of 0.2 m (baseline distribution), 1 m and 3 m. Right: Parameters for baseline distribution.

If F_{complex} is the fraction of the MLI covered area bound in complex fragments, then the total area available for creation of fragments in the form of single sheets of MLI is given by:

$$A_{\text{tot,single}} = n_{\text{layers}} \cdot \left(1 - F_{\text{complex}}\right) \cdot \left[\left(\frac{A_{\text{satellite bus}}}{m_{\text{satellite}}}\right) \cdot m_{\text{satellite}}\right] \tag{7.11}$$

$$n_{\text{layers}} = \begin{cases} 2 & : \text{ cover layers} \\ 18 & : \text{ reflector layers} \end{cases} \qquad F_{\text{complex}} = 0.75$$

where $A_{\text{satellite bus}}/m_{\text{satellite}}$ is again given by Equation 7.1.

7.3.3 Titan III Transtage Insulation

Martin-Marietta developed an upper stage for the Titan launcher which was used on the Titan 3 to boost satellites to different orbits (Wade 2013c, Leitenberger

2009). The Transtage upper stage had a diameter of 10 feet (3.048 m) and was 14.75 feet (4.4958 m) long (Park et al. 1973). Thrust was produced using the hypergolic fuel Aerozine 50 and oxidizer N_2O_4 which fed two AJ-10-138 engines. The re-ignitable booster stage used hydrazine monopropellant attitude control thrusters for three-axis stabilization (Morrisey et al. 1969). The fuel and oxidizer tanks were insulated by goldized steel foil separated by a layer of refrasil from the tank wall. In critical regions near the engines, a rubber layer was added for additional insulation (Park et al. 1973). Based on data published by Hi-Temp Insulation Inc., a producer of plated steel foil for space applications, it is estimated that the steel foil had a thickness of about 3 mil.

The MLI fragmentation model was expanded to estimate the steel foil debris which may have been created during fragmentation events of the Transtage rocket body in GEO. This was achieved by adapting the total insulation area, distribution of fragment sizes and the reflectivity of the created debris. The total area of steel foil was derived from the volume for the oxidizer and propellant tanks, exploded assembly drawings of the spacecraft and its overall diameter as published by Park et al. (1973). The respective parameters are presented in Table 7.2. It is assumed that half of the total steel foil will disintegrate into fragments while the rest remains attached to the remnant body. The largest upper limit for fragment sizes L_c is set to slightly less than the circumference of one tank. The lower limit of L_c is equal to half of the upper value. Fragment characteristic lengths are uniformly distributed between these two values. This simplifying approach is identical to the method used for complex MLI fragments. The minimum and maximum reflectivity values are 0.6 and 0.81 and were taken from Kauder (2005) for 1 mil 304 steel foil and for gold plated aluminum respectively.
The aim of the Titan III Transtage insulation debris model was to find out how the orbits of such debris might evolve with respect to the Laplace plane. Especially the estimation of size and number of fragments is overly simplistic and must be viewed with extreme caution.

7.3.4 Added Velocity

The velocity change (Δv) applied to fragments during an explosion or collision event dictates the shape and orientation of their initial orbit. To date, no consistent model exists for estimating the Δv for MLI. Several studies are quoted in the MASTER-2009 Final Report (Flegel et al. 2011a) which looked at Δv from

Table 7.2: Estimated parameters of Titan III Transtage components. Parameters derived from Park et al. (1973).

	Oxidizer tank - N_2O_4	*Fuel tank - Aerozine 50*
Tank volume V_{tank} =	4.99 m^3 (176.22 ft^3)	4.00 m^3 (141.37 ft^3)
Top section	spherical dome with diameter d	spherical dome with diameter d
Mid section	cylinder with diameter d	cylinder with diameter d
Bottom section	cone with height $h_{\text{cone}} = d$	cone with height $h_{\text{cone}} = d/2$
Diameter d	1.51 m	1.22 m
Tank height h_{tank}	4.04 m	4.04 m
Tank area A	16.02 m^2	14.78 m^2

ground tests, observations and simulation results. For upper stages, the highest Δv was derived to be about 3 km/s. It was based on ground tests in which six steel casings were detonated. It is pointed out that detonations should only be possible for liquid hydrogen (LH2) and liquid oxygen (LOX) mixtures which have been utilized by the Ariane H-10 upper stage for instance. Several fragmentation events are known to have occurred involving the early versions of this upper stage (Johnson et al. 2008). A mechanism for venting of remaining fuel after mission end was incorporated into these upper stages starting in 1993 (Bonnal and Naumann 1997). To date, no reports have been published indicating that a passivated H-10 upper stage has ever exploded.

Unfortunately, no measurement data is available detailing velocity changes of MLI during fragmentation events. In space debris simulations, the NASA Breakup Model is the most widely used model for fragmentations and has been published by Johnson et al. (2001) with clarifications and corrections published by Krisko (2011). The Δv used in this model is derived as a function of the area-to-mass ratio. Since this ratio increases towards smaller fragment sizes (Krisko et al. 2008, Oswald et al. 2006), the velocity change of HAMR objects is primarily based on that of small size debris. The data from which this model was derived did not include MLI or other large pieces of HAMR debris. It is therefore unlikely that this relation can be applied to such objects without alteration.

For an acceptable estimation of the Δv some assumptions must be made. The majority of large, coherent MLI is fixed to the outside of spacecraft. Propellant tanks and batteries have been known to be the primary source for violent fragmentations (Johnson et al. 2008). Both are typically located within the insulated satellite structure. It is assumed that MLI debris from the outer insulation is expelled at roughly the same velocity as other fragments of similar size which are closer to the energy source causing the fragmentation. Furthermore, it is assumed that the general dependencies of the Δv equations from the NASA Breakup Model apply also to MLI. The calculated velocity change for MLI from this model is then compared to other debris with similar characteristic lengths. The Δv for MLI is finally scaled with a constant factor to match the distribution of other debris of similar sizes. It was found that reducing the calculated velocity change by a factor of four produced the desired results. Figure 7.6 compares the original calculation to the scaled distribution.

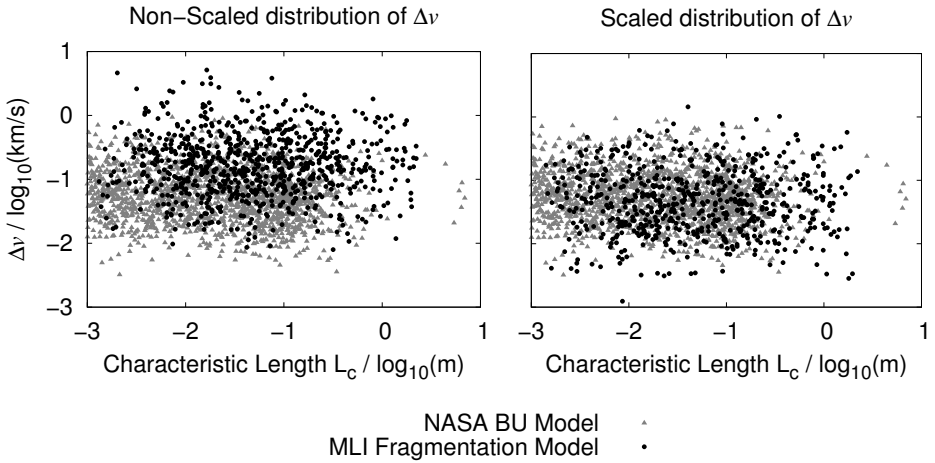

Figure 7.6: Left: Δv applied to MLI fragments using the standard NASA Breakup Model. Right: Δv for MLI is determined by reducing the value given by the NASA Breakup Model by a factor of four.

7.4 Continuous MLI Source Modeling

In the continuous MLI source model, it was planned to apply a small velocity change of 1 m/s to the debris upon release. An implementation error however led to a much larger velocity change of 1 km/s which is about a third of the orbit velocity in GSO and affects the initial orbit significantly. Figure 7.7 shows the inclination versus right ascension of ascending node distribution of MLI objects larger than 50 cm and with semi-major axis above 38,000 km from the uncorrected and corrected model for May 1st, 2009. As can be seen in the results of the uncorrected model, the high velocity change leads to a high spread in orbit normal vectors.

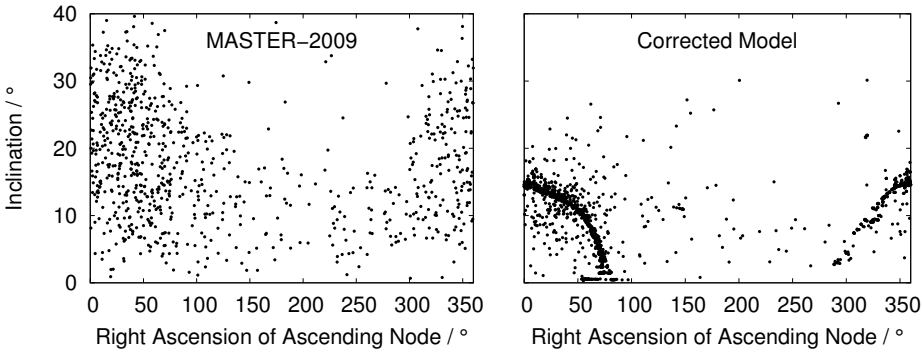

Figure 7.7: Inclination vs. right ascension of ascending node of continuous source MLI > 50 cm for May 1st of 2009. Left: MASTER-2009 model version. Right: Corrected Δv results.

In the validation process of MASTER-2009, this spread was assumed to have resulted mainly from the interaction of solar radiation pressure with the objects. Comparison of the tracklets which were obtained from measurements performed with ESA's Space Debris Telescope to the detections from the simulated surveys showed good correlation with respect to the distribution in inclination and right ascension of ascending node (see Figure 5.6). Furthermore, the spread in orbit plane orientation caused MLI objects to fill a gap which no other debris source could satisfy at the time. Inconsistencies only became apparent once

simulations of the future evolution of the MLI debris were initiated. These exhibited a seemingly unrealistic escalation of the continuous MLI debris source. That the release rate of large pieces of MLI due to ageing-related processes may have been over-predicted is further supported by the results from the update to the MLI debris sizes within the MLI fragmentation model. These changes lead to an increase in the detected MLI debris from fragmentation events. For the total number of simulated detections not to exceed the actual measurements, the release rate of detectable ageing-related MLI debris in turn must be reduced. All of these changes create two issues: for one, only few MLI objects remain whose evolution of the orbit normal vector differs significantly from the typical precessing motion about the Laplace plane. Measured tracklets which exhibited this characteristic must therefore belong to objects whose origin once more is unknown. Finally, objects created by the continuous MLI source can no longer be distinguished from those of the MLI fragmentation model in the simulated observations. All of these factors prompted the decision to exclude the continuous MLI source model from further simulations for the time being.

7.5 Updated MLI Population

Figure 7.8 presents the evolution of the number of in-orbit MLI objects larger than 5 cm over time. Objects with a semi-major axis above 35,000 km typically have their origin in the GEO region and are therefore counted as such. In accordance with the conclusions from the previous section, the continuous MLI source model is omitted and MLI fragments are modeled using the updated fragmentation MLI model only. The fragmentation events up to May 1st of 2009 are based on the 14th edition of "The History of On-Orbit Satellite Fragmentations" (Johnson et al. 2008) and the Orbital Debris Quarterly News (`http://orbitaldebris.jsc.nasa.gov`). Both are published by NASA's Orbital Debris Program Office. For the GEO environment, some additional events have been defined which are presented in Table 8.2 of the following chapter. May 1st of 2009 has been chosen as the reference date as this is also the reference epoch of ESA's MASTER-2009 software. A business-as-usual scenario according to the MASTER-2009 Final Report (Flegel et al. 2011a) is used for the ensuing time frame. Apart from the Transtage upper stage, only MLI fragments from spacecraft have been modeled. Between 2009 and 2060 a total of 90 events involving spacecraft are simulated of which 6 occur in the GEO region. No Transtage frag-

mentations are simulated in the business-as-usual scenario. The grey area surrounding the mean values after 2009 represent the standard deviation resulting from the chosen Monte-Carlo approach. Most MLI debris was created in events which took place during the 1980s. The majority of events during this time involved Soviet spacecraft of the type COSMOS 862 and COSMOS 699. These spacecraft are believed to have employed explosive charges which triggered the events (Johnson et al. 2008). The COSMOS 699 class satellites had perigees typically below 500 km so that debris from these events decayed very quickly. The COSMOS 862 however resided on Molniya orbits with perigees between 500 and 1,500 km and apogees around 40,000 km. Fragments on such orbits may remain on orbit significantly longer and are difficult to track. The decay rate in GEO is much lower than in LEO or even on Molniya orbits due to the absence of atmospheric drag. Only orbits from objects with effective area-to-mass ratios above about 48 m^2/kg become eccentric enough to decay due to atmospheric drag (see Section 6.4.2). This causes a steady increase in MLI debris in GEO.

The distribution of area-to-mass ratios of MLI objects of all sizes for the epoch May 1st of 2009 is shown in Figure 7.9. The left hand plot shows the area loading (A/m) which is purely material dependent. The two individual peaks for

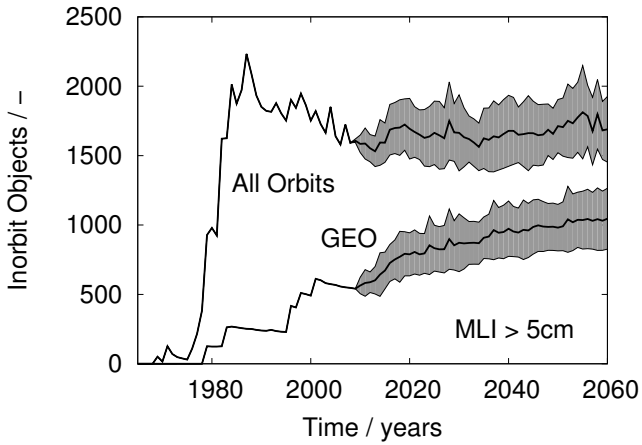

Figure 7.8: Evolution of in-orbit MLI larger then 5 cm over time.

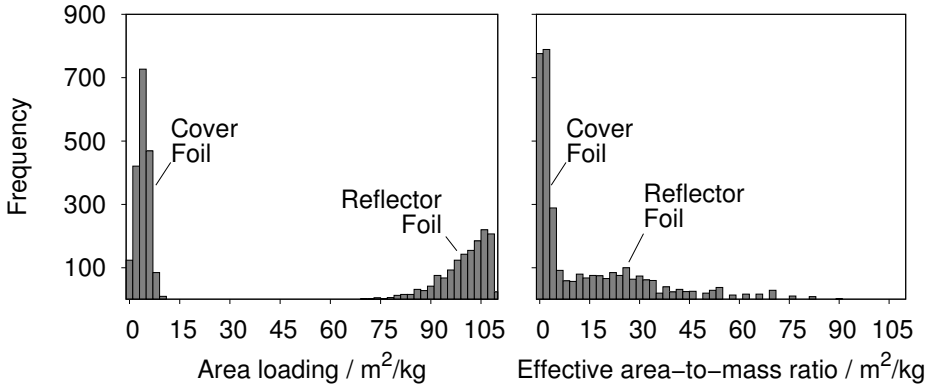

Figure 7.9: Simulated MLI objects for May 1st, 2009. Left: area loading (A/m). Right: Effective AMR ($A/m \cdot F_{\text{reflectivity}} \cdot F_{\text{deformation}} \cdot F_{\text{tumbling}}$).

the thicker cover foil debris and thinner reflector foil objects are clearly visible. Taking into account deformation, tumbling and reflectivity, leads to the effective area-to-mass ratio $(A/m)_{\text{eff}}$ shown in the right hand plot. Compared to the area loading, the effective area-to-mass ratio is lower and the variation in the values for the reflector foil is increased. Most objects have effective area-to-mass ratios well below 50 m^2/kg so that most GEO MLI debris should remain on orbit for an extended period of time.

For the reference epoch, the highest spatial density of MLI objects is found around 800 km where the majority of fragmentation events have occurred (Figure 7.10). Below this altitude the atmospheric drag rapidly increases. MLI objects are especially susceptible to drag due to the large area-to-mass ratios. The shallow peak between 3,000 and 5,000 km is caused by the fragmentation of 1966-056A "PAGEOS" in early 1976 at an altitude near 4200 km. In the simulation the reflector foils of the 55 kg spacecraft decayed within half a year after the event while about 100 cover foil fragments remained in orbit in 2009. The majority of these fragments is smaller than 10 cm in size. The altitudes above this are dominated by fragments from events which occurred on highly eccentric orbits such as Monliya orbits, and on GEO.

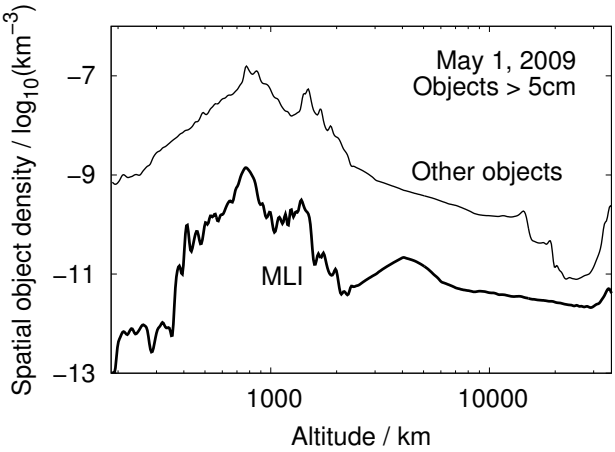

Figure 7.10: Spatial object density over altitude of objects larger than 5 cm.

Chapter 8

Simulating the ESA-SDT Observations

ESA's Space Debris Telescope (ESA-SDT) is situated on Tenerife at 28.1758° N and 16.306° W. It has modified Ritchey-Chrétien optics with a 1.016 m aperture and a liquid nitrogen cooled CCD with 4096×4096 pixels (Schildknecht 2007). In the past, ESA has tasked the Astronomical Institute of the University of Bern (AIUB) to survey the GEO and GEO-transfer orbit (GTO) regions for debris using this telescope. The observations serve the purpose of gaining insight into the number and distribution of objects which are not contained in the catalog of the USSTRATCOM. As such, the obtained data is of statistical nature and is not intended to create a database of objects with regularly updated orbits. The results which will be used in the current work are those from the surveys of the GEO region from the years 2001 to 2007 and from those of the GTO observations performed in the years 2004 to 2007. ESA's **P**rogram for **R**adar and **O**ptical **O**bservation **F**orecasting (*PROOF*) is used to simulate these campaigns based on the given observation profiles and by using simulated orbital debris populations which are correlated with orbits of known objects. Detections which could be matched to objects being tracked by the Space Surveilance Network (SSN) have been removed from the measurements allowing to use the data to validate the computer models underlying the simulated populations.

Initially, an overview will be given of the measurements obtained in the GEO and GTO surveys. Statistics as well as some limitations to the available data are presented. Using the MASTER-2009 GEO fragmentation list and data given by Oswald et al. (2006), a revised list of GEO events is proposed. A compari-

son is then made between the measurement data and simulation results without MLI debris. Following this, fragmentations of Ariane H10 3rd stages on GTO orbits are looked at. Evidence is presented which suggests that the number of detectable fragments which were released during these events may previously have been underpredicted and that these could make up a significant portion of the detections in the GTO observation campaigns. The albedo of MLI is an input which is required by *PROOF* and is derived in the following section. Following this, the results from the simulated SDT campaigns which were obtained using *PROOF* are compared to the measured data. The chapter concludes with an investigation of uncertainties in the MLI model and the possibility of debris contributions from undetected fragmentations.

8.1 ESA's Space Debris Telescope Debris Detections

A major difficulty in detecting debris objects in the vicinity of the GEO region is that they typically appear as very faint objects. A measure for the apparent brightness of an object is the *apparent magnitude*. It describes the brightness of an object relative to a fixed reference value. A logarithmic scale is used in which bright objects have low values and faint objects have high values. As reference, the Sun's and Pluto's maximum apparent magnitudes are about -27 and +14 respectively. An important factor in the apparent magnitude of orbiting objects is the amount of sunlight which is reflected towards the telescope. This does not only depend on the size of the object but also its reflective properties and more importantly, the object's orientation and the relative position of the telescope, the Sun and the object. Schildknecht (2007) estimates that a 10 cm debris object may produce an apparent magnitude of around +20. The ESA-SDT has a lower magnitude detection limit of +22 although the system sensitivity starts to tail off between +19 and +20 magnitude. This very high sensitivity poses harsh constraints on the telescope's design as well as on the observation strategies. On the hardware side, this is achieved by using a very small field of view of 0.709° and exposure times for each frame of two to four seconds depending on the survey. Surveys are specifically designed to concentrate the light from the objects on a limited number of pixels of the camera's CCD. This is done by letting the telescope follow the expected motion of objects on a predefined orbit of interest (blind tracking). Objects residing in the field of view during exposure thus appear as dots while objects on other orbits or stars are visible as streaks

(Schildknecht 2007). Objects in GEO or GTO typically cross the field of view within 2.5 to 4 minutes. The exposure time for one frame is adapted to the specific search strategy. For the GEO observations, an exposure time of 2 seconds was used. For the GTO surveys, longer exposure times of 3 and 4 seconds were chosen. Crossing objects therefore usually appear on two to four subsequent frames only (Schildknecht et al. 2008a). Since it is difficult to observe velocity changes or changes in orbit altitude from the observation of these short orbital arcs, no information on eccentricity can be retrieved and circular orbits must be assumed initially (Schildknecht 2007). Especially for HAMR objects with mean motion similar to GEO and for GTO objects this assumption does not hold. GTO objects typically have eccentricities around 0.7 and HAMR objects exhibit eccentricities as high as 0.8. The tentative orbits derived by this method are called *tracklets*.

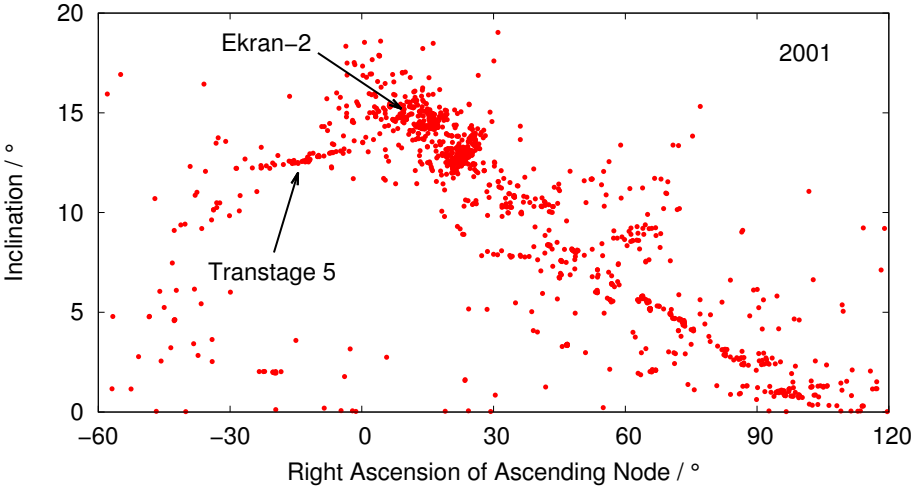

Figure 8.1: ESA-SDT detections from all campaigns performed in 2001. The debris clouds from the only two officially acknowledged fragmentation events of GEO objects are indicated.

In the following, only tracklets of objects which could not be correlated to those in the USSTRATCOM's catalog are looked at. The remaining objects thus are

either debris or classified spacecraft for which no orbit data is publically available. Figure 8.1 shows the inclination and right-ascension of ascending node of uncorrelated tracklets for all observed magnitudes from the GEO campaigns performed in the year 2001. The precession of the orbit plane of uncontrolled objects with mean motions near GEO is very similar for all objects with low area-to-mass ratio. This precession about the Laplace plane is described in more detail in Section 6.4. As a result, these objects exhibit similar parameters in the i-Ω space, leading to a pattern specific to this orbit region. To date, only the fragmentation of the Ekran-2 satellite and the Transtage 5 upper stage have been officially confirmed (Johnson et al. 2008). Figure 8.2 shows the uncorrelated tracklets for the years 2002 to 2007. Detections from GEO campaigns are represented as solid blue dots while tracklets from GTO surveys are given as red circles. The additional GTO observations between 2004 and 2007 resulted in an increase in detections. In the plots, many of these objects are distributed seemingly randomly in i and Ω.

Measurements exhibit an accumulation of detections around +13 magnitude and a more pronounced increase below +15 magnitude which tails off at the detection limit of +19 to +20 magnitude. This characteristic is present to varying degrees in all survey results. It is exemplified by Figure 8.3 which shows a histogram of all uncorrelated tracklets from the 2004 surveys. Of the objects brighter than +14 magnitude, a portion is likely to be debris from fragmentation events. Classified objects may however contribute to these objects as well (Agapov et al. 2008). The region below +15 magnitude is dominated by debris.

Six parameter orbit sets were derived for some of the detected objects by performing follow up observerations. Using this approach, Schildknecht (2007) showed that a significant number of uncorrelated objects from the GTO surveys had eccentricities as high as 0.8 while retaining a mean motion close to that of GEO objects. Derivation of the effective area-to-mass ratio of 28 of these objects initially revealed ratios up to $28\,\mathrm{m}^2/\mathrm{kg}$. Later analyses showed that some objects had even higher ratios (Musci et al. 2010, Schildknecht et al. 2010). MLI is a strong contender for being the source of these objects: not only has it been used since the early space fairing days - the foils are also one of the few materials which have area-to-mass ratios in the range of the observed objects while being large enough that they may be detected by the ESA-SDT.

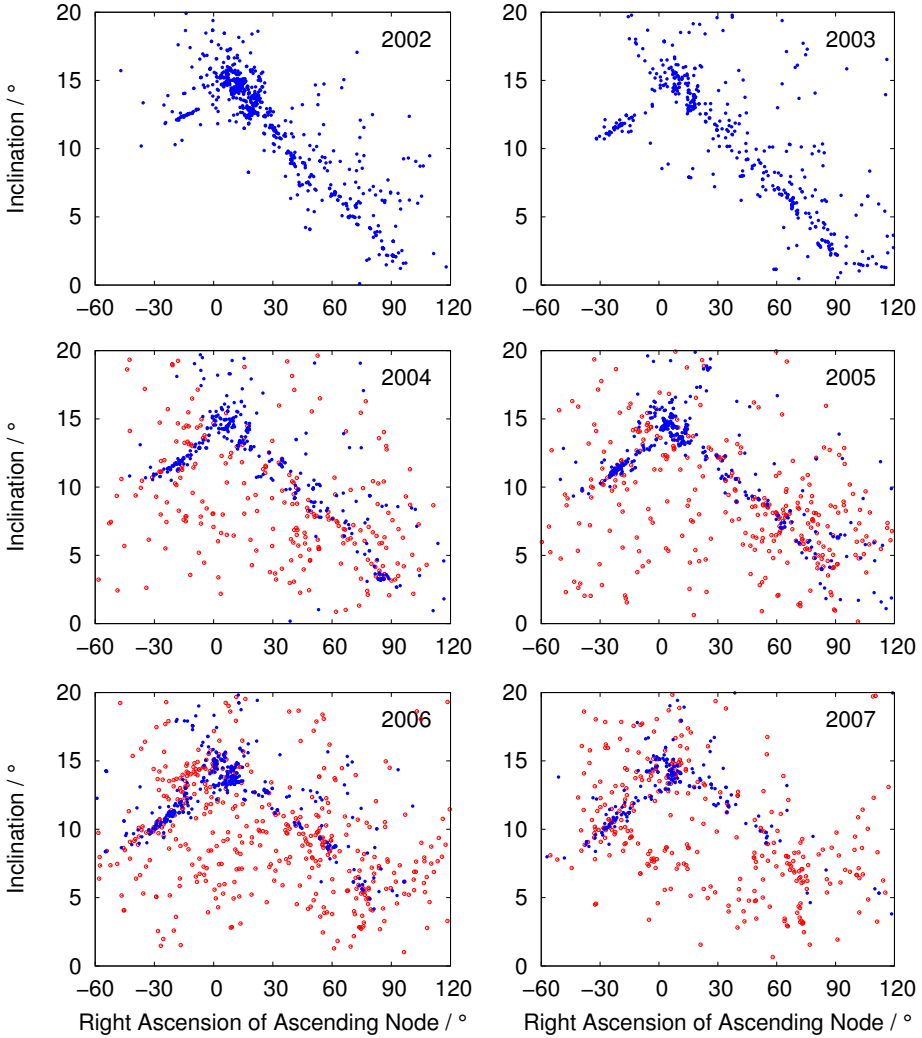

Figure 8.2: Inclination vs. right-ascension of ascending node of uncorrelated tracklets observed by ESA's Space Debris Telescope during the years 2002 through 2007. Detections from GEO surveys are given as solid blue dots. GTO survey detections are represented by red circles.

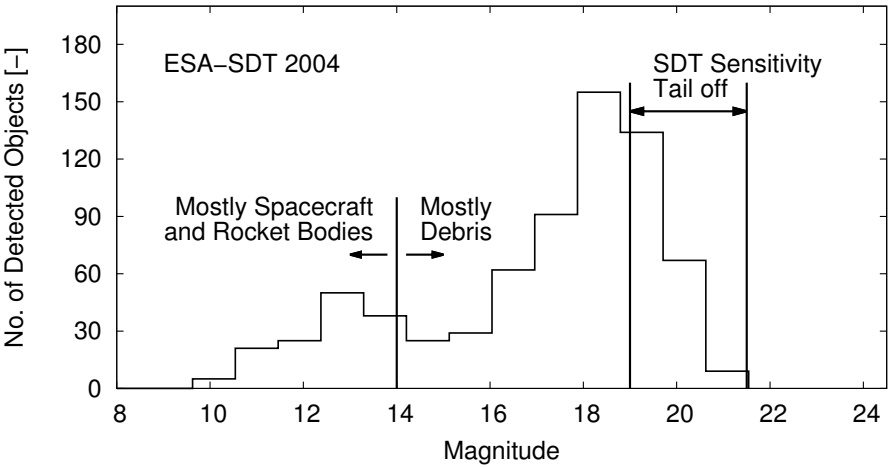

Figure 8.3: Magnitude histogram of uncorrelated detections from 2004 ESA-SDT GEO and GTO surveys.

8.2 Simulating Fragmentations in GEO

Explosion and collision events cause fragments to be ejected at velocities up to a few kilometers per second in extreme cases. Results for the distribution of delta velocities from relevant studies are given in the MASTER-2009 Final Report (Flegel et al. 2011a). These velocities cause the initial orbits of the fragments to vary from that of their parent object. The differences in the orbit period as well as perturbations acting on the shape and orientation of the orbits cause the fragments to disperse over time (Klinkrad and Martin 2006). The more time lies between the fragmentation event and the epoch for which orbit parameters of an object are known, the more difficult it becomes to determine its source of origin. Main reasons for this are the increasing spatial dispersion of the fragments and inaccuracies in the orbit prediction. Perturbative effects however vary for different orbital regimes. Patterns can be found in the orbit evolution of some orbit types which can aid in identifying fragments belonging to the same parent object. For the GEO region, such a pattern can be found in the precessing

motion of the orbit planes of uncontrolled objects with low area-to-mass ratios about the Laplace plane (see Section 6.4). The precession period of these objects is about 53 years. This effect causes the orbit normal vectors of fragments of an event which has occurred in this region to remain similarly oriented in space even decades after an event (Oswald et al. 2006).

Table 8.1: List of GEO fragmentation events from MASTER-2009. Table is reproduced from Flegel et al. (2011c)

Event Type	Int. Desig.	Name	m / kg	Epoch / yyddd.d	a / km	i / °
Known	1977-092A	Ekran-2	1970	78174.0	42182.3	0.1
Known	1968-081E	Titan 3C Transtage 5	1950	92053.4	41835.4	11.9
Unconfirmed	1973-040B	Titan 3C Transtage 24	1950	81067.2	42345.7	5.9
Unconfirmed	1979-087A	Ekran-4	1970	82157.8	42158.1	1.7
Unconfirmed	1979-053C	Titan 3C Transtage 30	1950	82309.0	42403.8	0.6
Unconfirmed	1975-118C	Titan 3C Transtage 28	1950	87072.6	42101.8	8.6
Unconfirmed	1966-053J	Titan 3C Transtage 11	1950	87276.7	40497.2	11.5
Unconfirmed	1967-066G	Titan 3C Transtage 14	1950	94045.4	39842.9	11.7
Unconfirmed	1975-117A	SatCom 1	463	99257.7	42354.6	12.0
Unconfirmed	1988-018B	Telecom 1C	1210	02263.0	42826.4	5.8
Artificial	-	Artificial 1	1750	98180.0	40164.0	0.3
Artificial	-	Artificial 2	1750	92280.0	44850.0	2.0

To this day, only two fragmentation events have been officially confirmed to have occurred in geosynchronous orbits (Johnson et al. 2008). Oswald et al. (2006) lists a total of 21 additional suspected GEO anomalies from which eight were introduced into the MASTER-2009 population as fragmentations. Another two events were added which were required to explain remaining features in the observations but for which no anomalies could be identified. Table 8.1 lists all MASTER-2009 GEO fragmentations. In the current work, the list was revised to better match overall detection features. Compared to the MASTER-2009 fragmentation list, four unconfirmed events (1975-118C, 1975-117A, 1988-018B and 1967-066G) were removed and replaced by two others from the list given by Oswald et al. (2006): 1987-095A and 1983-030A. Also the artificial events were altered to better match observations. The number of fragments produced in the Transtage 11 and 24 incidences as well as by Ekran-4 were reduced. The event epoch of Transtage

30 was postponed from 1982 to 1983. The total number of simulated GEO events has thus been reduced from 12 to 10. The revised list is given in Table 8.2.

Table 8.2: Revised list of GEO fragmentation events. Events with a '*' were modified from the MASTER-2009 list, underlined events have been added.

Event Type	Int. Desig.	Name	m / kg	Epoch / yyddd.d	a / km	i / °
Known	1977-092A	Ekran-2	1970	78174.0	42182.3	0.1
Known	1968-081E	Titan 3C Transtage 5	1950	92053.4	41835.4	11.9
Unconfirmed*	1973-040B	Titan 3C Transtage 24	1950	81067.2	42345.7	5.9
Unconfirmed*	1979-087A	Ekran-4	1970	82157.8	42158.1	1.7
Unconfirmed*	1979-053C	Titan 3C Transtage 30	1950	83309.0	42403.8	0.6
Unconfirmed*	1966-053J	Titan 3C Transtage 11	1950	87276.7	40497.2	11.5
Unconfirmed	1987-095A	TV Sat 1	1750	95356.6	42438.6	5.9
Unconfirmed	1983-030A	SatCom 1R	1750	97273.0	42280.8	3.8
Artificial*	-	Artificial 1	1750	00203.0	40164.0	0.3
Artificial*	-	Artificial 2	1750	95280.0	42164.0	0.3

The orientation of the orbit plane in space is expressed by an orbit's inclination with respect to the Earth's equator and the right-ascension of its ascending node. Figure 8.4 superimposes simulated fragments from the revised list larger than 10 cm for the epoch May 1st, 2001, over the tracklets from the 2001 campaigns in the inclination versus right-ascension of ascending node space. In MASTER-2009, the two artificial events were the sole contributors to the Ω region between 30 and 120 °. Alteration of these events as well as the addition of two new unconfirmed events places a total of four smaller events in this region. A slight over prediction at high inclinations was reduced by removal of two unconfirmed events for which no clustered fragments could be identified. A rather large feature around $i = 8$ ° and between 30 and 70 ° in RAAN can be observed in 2001 which vanishes in the following years as can be seen in Figure 8.5. A plausible explanation for this feature will be given in Section 8.3. Figure 8.5 shows the evolution of the debris clouds over time for the years 2002 through 2007. Simulated fragments larger than 10 cm for the epoch May 1st for each year have been superimposed over uncorrelated tracklets from ESA's SDT.

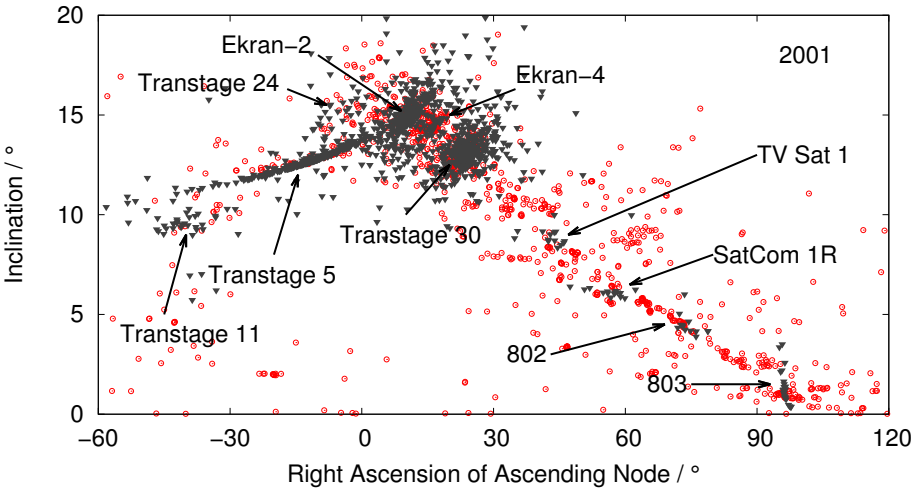

Figure 8.4: Overview of GEO fragmentation events (grey triangles) and ESA-SDT detections (red circles) from 2001. Only debris simulated by the NASA Breakup Model which is larger than 10 cm for the epoch May 1st, 2001 is plotted.

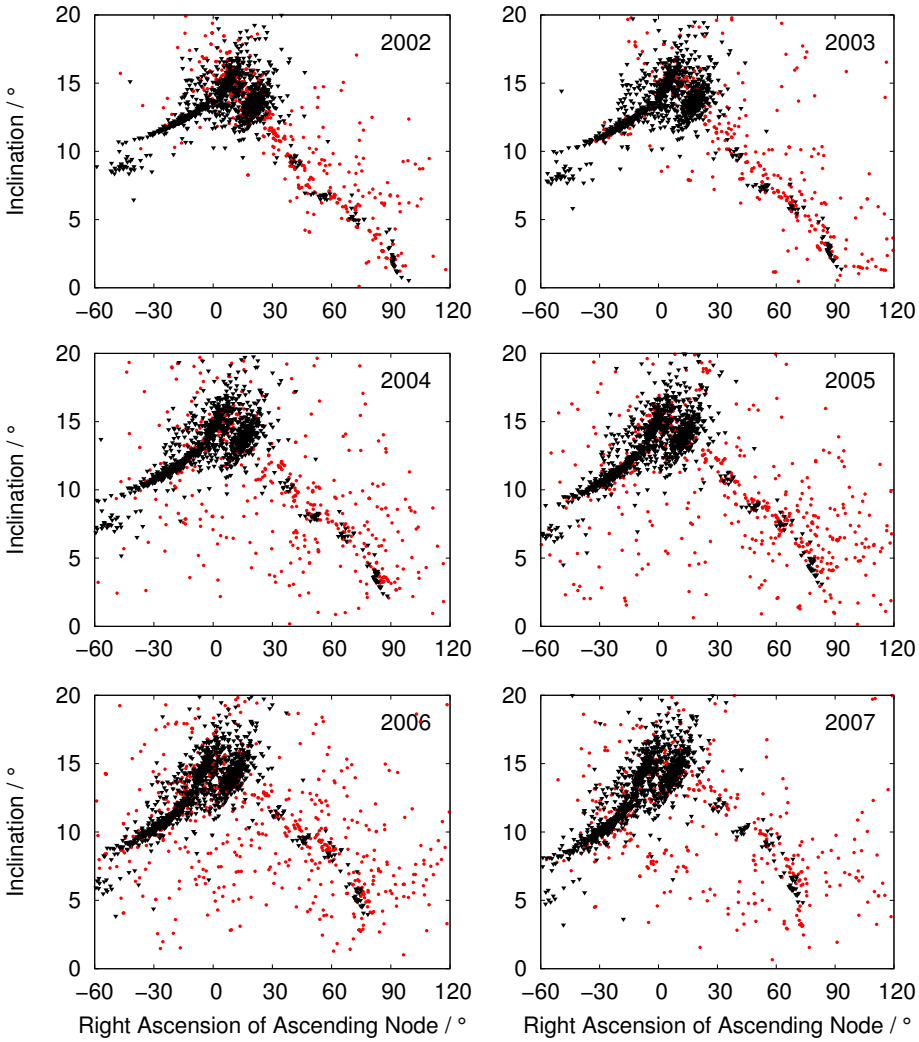

Figure 8.5: Inclination versus right-ascension of ascending node of tracklets from 2002 to 2007 ESA-SDT surveys (red dots). Black dots are fragments > 10 cm for May 1st of each year which were simulated using the NASA Breakup Model.

8.3 Ariane H10 3rd stage fragmentations

The Ariane H10 3rd stage was used as an upper stage for Ariane 2, 3 and 4 in different versions. It was derived from the Ariane 1 H8 upper stage and was retired in 2003 (Wade 2013b). Starting in October 1993, the H10 3rd stages were passivated at the end of their mission by venting remaining propellants (Bonnal et al. 1997). In all, nine fragmentations of Ariane H10 upper stages are known to have occurred - all of them involving the unpassivated version. Within the current work it was found that the fragmentation of the 1989-006B Ariane 2 H10 3rd stage specifically appears to have been observed in surveys of the GEO environment by the ESA-SDT which had previously not been identified. This event is detailed in the following section, followed by an overview of all known H10 events.

8.3.1 1989-006B Fragmentation

On January 27, 1989, Intelsat 5A F-15 was launched with an Ariane 2 V28 rocket. The satellite was successfully inserted into GEO (Wade 2013a). On January 1, 2001, more than ten years after its launch, the rocket stage fragmented in its GTO with the vehicle equipment bay (VEB) attached (Johnson et al. 2008). The rocket body had a length of 9.9 m with an additional 1.15 m for the Vehicle Equipment Bay (VEB) leading to an overall height of 11.05 m (Leitenberger 2010). Wade (2013b) reported an overall length of 11.53 m while Johnson et al. (2008) gives 11.7 m as the total length. The diameter is around 2.60 - 2.66 m (Leitenberger 2010, Wade 2013b, Johnson et al. 2008). The stage used liquid oxygen and liquid hydrogen (LOx/LH2) as oxidizer/ propellant with an HM-7B engine. At the time of event, the vehicle had a mass of 1.48 t according to Johnson et al. (2008). The mass given by Leitenberger (2010) is slightly higher at 1.655 t which is derived from 1.336 t dry mass of the H10 stage plus 319 kg for the VEB. The VEB of the Ariane 2/3 was derived from the Ariane 1 VEB. It contained most of the electrical systems as well as the on-board computer in charge of guidance and attitude control (Johnson 1989). According to Bonnal and Naumann (1997), about 120 kg of LH2 and about 160 kg of LOx remained in the fuel tanks after nominal mission end. This remnant fuel is the most likely cause for the violent fragmentation of the rocket body.

The event was simulated based on the parameters given in Table 8.3. Using *PROOF*, the distribution of the fragmentation debris which could have been de-

Table 8.3: 1989-006B Ariane H10 3rd stage fragmentation event.

Int. Desig.	Name	m / kg	Event / yyddd.d	Launch / yyddd.d	a / km	ϵ / –	i / °
1989-006B	Ariane 2 H10	1480	01001.5000	89027.5000	24492.1	0.7193	8.39

tected in the 2001 to 2007 ESA-SDT surveys was calculated. Figure 8.6 compares the inclination and right ascension of ascending node of these results to the measured tracklets. In the 2001 survey results, the simulation shows multiple detections of the new debris cloud as its right ascension of ascending node drifted due west throughout the campaign year. The same features are clearly visible in the measurement results of the SDT. The drift is the result of the precession of the orbit which is induced by the oblateness of the Earth. For the 1989-006B debris cloud, the mean drift rate was about 140 ° per year. As it depends on the semi-major axis, the inclination and the eccentricity of the orbit, it differs slightly for all fragments and causes the debris cloud to disperse over the entire right ascension of ascending node range in time. This causes the compact features which were observed in the 2001 campaigns to dissolve in the following years. Almost no debris from this event is detected in the simulated 2002 campaigns (see lower plot in Figure 8.6). With the launch of the GTO campaigns in 2004, more of the debris from this event is observed in the simulations in the form of detached clusters.

8.3.2 Simulating Ariane H10 3rd stage fragmentations

Analysis of the 2001 survey results showed that almost all TLE objects which were detected by *PROOF* and which were located in i-Ω regions uncharacteristic of objects on GEO drift orbits were fragments from Ariane H10 3rd stages. It therefore seems likely that other uncorrelated tracklets in this region may belong to uncataloged debris from these events. In MASTER-2009, a total of nine explosion events involving this rocket stage were simulated. The amount of detectable debris was however too little to cover the uncorrelated tracklets in this region. The highly eccentric orbits on which these events occurred make cataloging of fragments difficult. It is possible therefore that a significant number of fragments has not been cataloged. In 1986, the 1986-019C H8 rocket stage exploded on a sun-synchronous LEO. By 2013 almost 500 fragments had been cataloged from

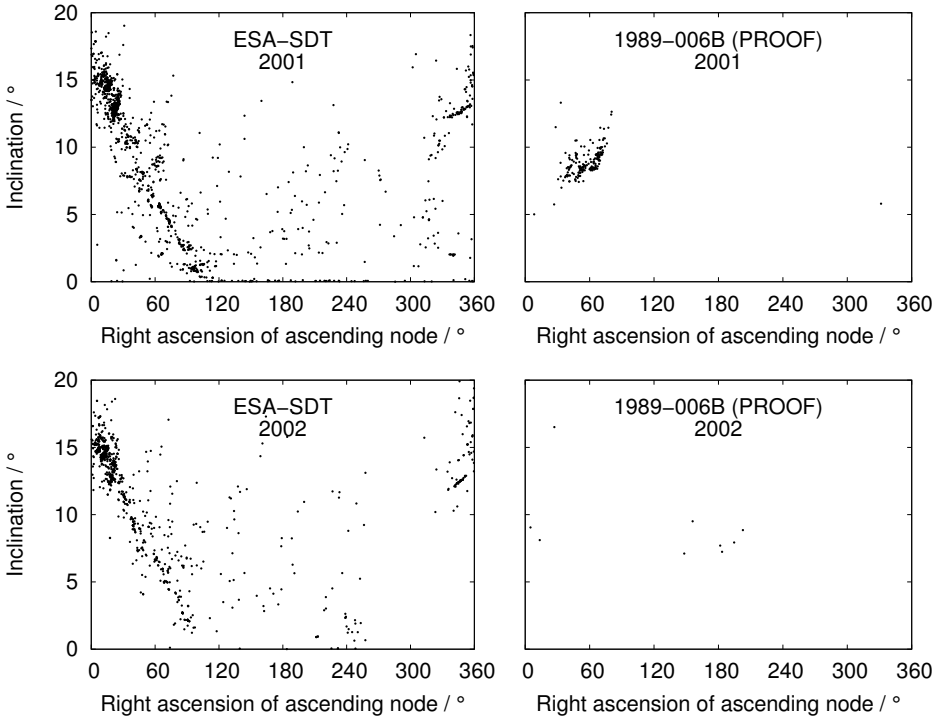

Figure 8.6: Inclination vs. right ascension of ascending node of objects detected during 2001 (top) and 2002 (bottom) surveys. Left: Tracklet data from ESA-SDT. Right: Simulated detections of modeled debris from 1989-006B event.

this event. As the H10 was derived from the H8, it seems all the more likely that the debris created in the fragmentations of the H10 has previously been underestimated. In the current study, it was assumed that almost all H10 events created about 500 fragments larger than 10 cm. Only the 1984-114C and 1988-109C explosions were modeled with fewer fragments. Especially for the fragmentation of the 1988-109C a higher debris count created an over-prediction in the simulations. Table 8.4 gives an overview of the modeled explosions involving Ariane H10 3rd stages. The results of the simulations are presented in Section 8.5.

Table 8.4: Overview of simulated Ariane H10 3rd stage fragmentation events.

Int. Desig.	Name	m / kg	Event / yyddd.d	Launch / yyddd.d	a / km	ϵ / –	i / °
1984-114C	Ariane 3 H10	1100	84326.1007	84315.5500	24513.0	0.7266	7.03
1988-040B	Ariane 2 H10	1480	88191.3125	88139.4900	24361.0	0.7163	7.03
1992-021C	Ariane 4 H10	1800	93111.5000	92106.9800	24319.4	0.7243	4.04
1991-015C	Ariane 44LP H10	1760	94107.0700	91060.9800	20899.4	0.6818	6.56
1991-003C	Ariane 4 H10	1760	96122.5000	91015.9700	21963.1	0.6993	6.73
1988-109C	Ariane 44LP H10	1760	98048.5000	88347.0200	24529.7	0.7216	7.34
1989-006B	Ariane 2 H10	1480	01001.5000	89027.5000	24492.1	0.7193	8.39
1991-075B	Ariane 4 H10	1760	01358.1512	91301.9600	20747.7	0.6814	7.20
1992-041C	Ariane 4 H10	1760	02032.9879	92190.9500	19830.5	0.6664	7.02

8.4 Estimating MLI Albedo

The MLI object albedo and standard deviation are inputs to *PROOF*. An object's albedo is affected by the surface reflectivity, the time averaged orientation with respect to the Sun and to the telescope and the deformation. The time averaged orientation is accounted for in the software by using the randomly tumbling plate assumption. This reduces the effective area by a factor four. The mean albedo is approximated by averaging the maximum and minimum possible effective area which are based on Equation 7.2. The respective values are given in Table 8.5. The standard deviation is calculated by assuming that the minimum and maximum values are equal to the three sigma values.

Table 8.5: Estimating the MLI object albedo for validation with *PROOF*

	Min	Max
$F_{\text{reflectivity}}$	0.33	0.87
$F_{\text{deformation}}$	0.95	1.00
$F_{\text{reflectivity}} \cdot F_{\text{deformation}}$	0.31	0.87
Mean (1σ)	0.59 (0.09)	

8.5 Results

All GEO and GTO fragmentations have been simulated using the NASA Breakup Model and the updated MLI fragmentation model as presented in Section 7. For the GEO and GTO Ariane H10 3rd stage events, the fragmentations listed in Table 8.2 and 8.4 were used respectively. All other events were simulated according to MASTER-2009 (Flegel et al. 2011a). Simulated objects with characteristics similar to fragments contained in the USSTRATCOM's catalog were removed and replaced by the actual objects. The SDT's 2001 to 2007 GEO and GTO surveys were then simulated with *PROOF* using the created population. The result is a list of objects along with their transient orbit elements and other characteristics which would have been detected in the surveys. Since the measurement data from the SDT only contain uncorrelated tracklets, all detected cataloged objects were removed from the simulation results.

The nature of the results from most simulated campaign years is similar. The major conclusions from the comparison to the observed tracklets can be outlined by analysis of the 2001 and 2006 results. Figures 8.7 and 8.8 show the i-Ω distribution of all detections which are brighter than +22 magnitude from these survey years. The upper plot shows the simulated uncorrelated detections while the lower plot depicts the uncorrelated measured tracklets. In the simulation results, red dots and blue triangles are fragments which were created using the NASA Breakup Model. The former represent objects from GEO events while the latter were produced in GTO fragmentations. The AMR of these detected objects is typically much lower than $1\,\mathrm{m}^2/\mathrm{kg}$. Black rectangles are detected MLI fragments. In the inclination range up to $20\,^\circ$, virtually all MLI objects were created in GEO events. The main reason for this is that most GTO fragmentations involved rocket bodies for which no MLI model could be derived due to the lack of information concerning the insulation of these upper stages. As detailed in Section 8.3 the debris cloud from the fragmentation of the 1989-006B Ariane 2 H10 3rd stage is clearly visible in the 2001 survey results. The figures illustrate that a significant part of the measured tracklets cannot be matched using GEO fragmentations and MLI alone. Furthermore, the results suggest that even in the campaigns which were specifically tailored to detect GEO debris, a significant amount of GTO objects might have been observed. GEO- and GTO-fragments with low area-to-mass ratios and HAMR MLI-debris each have different orbit types which can be distinguished in the simulated survey results:

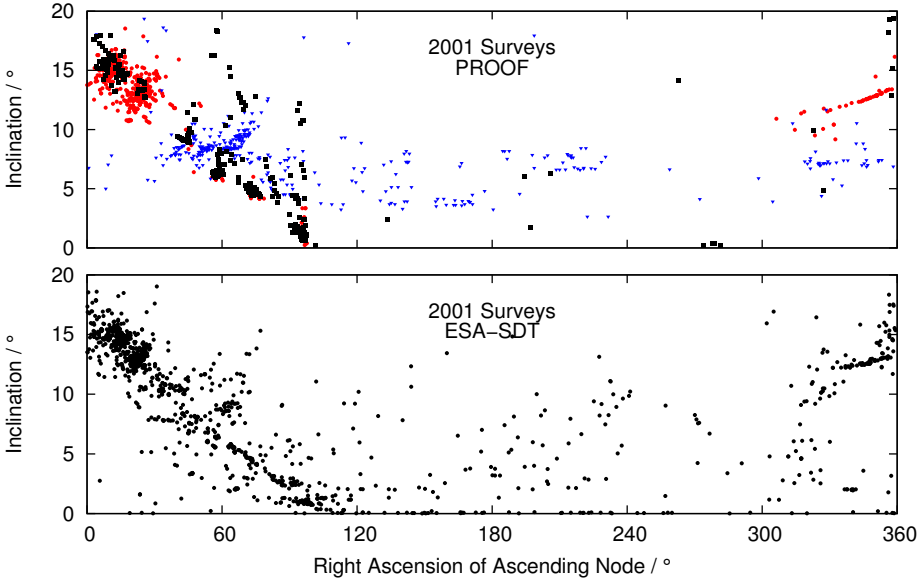

Figure 8.7: Comparison of simulated and observed uncorrelated tracklets with magnitudes brighter than +22 for the 2001 surveys. Top: *PROOF* results; red dots: GEO fragments from NASA-Breakup Model; blue triangles: GTO fragments from NASA Breakup Model; black rectangles: GEO MLI debris. Bottom: ESA-SDT tracklets from GEO surveys.

GEO Debris The orbit evolution of the low AMR GEO fragments is dominated by the orbit precession about the Laplace plane. A description of this effect along with the influence of the area-to-mass ratio on the orientation of this plane is given in Section 6.4. The orbits of MLI debris precess about a modified Laplace plane, leading to higher inclinations and precession rates. MLI debris therefore typically occupies more highly inclined orbits than low AMR debris from the same events. The precession rate of objects with AMR values upwards of about $10\,\mathrm{m}^2/\mathrm{kg}$ is fast enough that some of these objects have similar i-Ω combinations as GTO detections at the time of the observations.

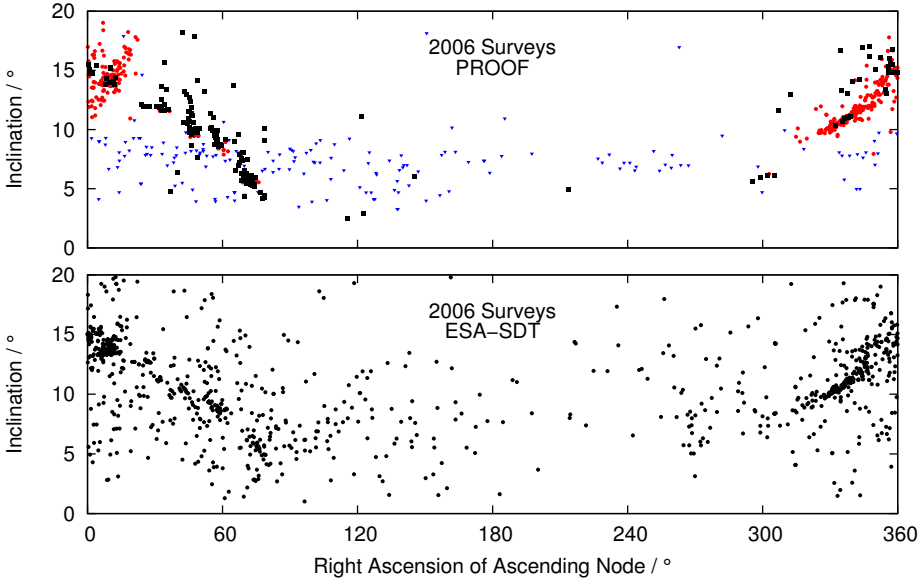

Figure 8.8: Comparison of simulated and observed uncorrelated tracklets with magnitudes brighter than +22 for the 2006 surveys. Top: *PROOF* results; red dots: GEO fragments from NASA-Breakup Model; blue triangles: GTO fragments from NASA Breakup Model; black rectangles: GEO MLI debris. Bottom: ESA-SDT tracklets from GEO and GTO surveys.

GTO Debris Low AMR GTO fragments occupy the inclination band between 4 and 9 °. Virtually all of the simulated GTO detections at these inclinations are of fragments from the nine H10 events (see Section 8.3), almost all of which occurred on orbits with inclinations around 7 °. The measured tracklets which fall in the vicinity of the simulated GTO debris are spread more widely in inclination than the simulated detections. A possible cause is that the uncertainty in the GTO tracklet parameters is influenced by the position of the object on its orbit: The initial orbit determination method assumes that the observed object is moving perpendicularly to its momentary orbit radius vector. For GTOs this only occurs when the objects are at their apo- or perigee. For all other locations, the obtained parameters are skewed by the change in the object's distance from the Earth during detection (Schildknecht 2007, 2013).

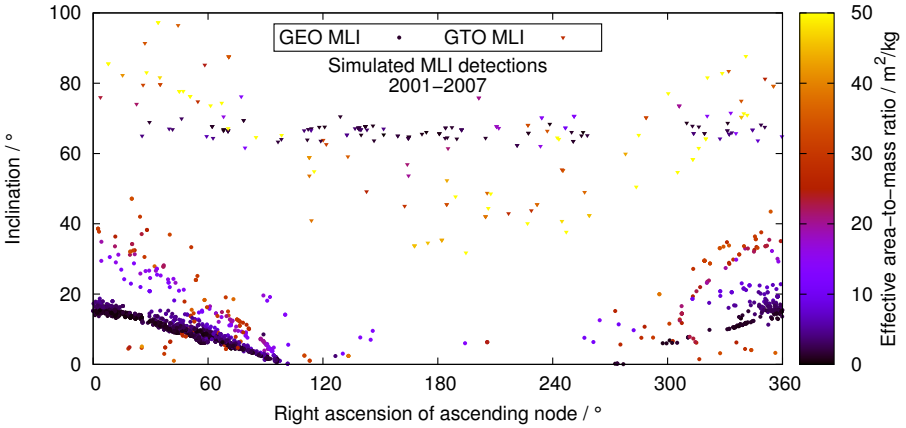

Figure 8.9: Inclination versus right ascension of ascending node distribution of MLI detections from all simulated surveys. Objects are color coded based on their effective area-to-mass ratio.

MLI Debris For the most part, the GEO MLI objects are on orbits similar to the debris simulated by the NASA Breakup Model with inclinations below 20 °. Figure 8.9 is a superposition of the MLI detections from all simulated surveys. MLI debris originating from GEO events are shown as circles while GTO MLI objects are represented by triangles. All objects are color coded based on their effective area-to-mass ratio. MLI from GTO events is created mostly in explosions of former Soviet satellites on Molniya orbits of the type Cosmos-862. The spacecraft carried explosive charges which were to detonate if control of the spacecraft was lost. In all, 16 events involving this spacecraft type are known to have occurred between 1977 and 1986 (Johnson et al. 2008). In the simulated observations, a total of 253 GTO MLI detections were triggered. The measurement data however only contains 34 tracklets with inclinations above 40 °. Several possibilities exist for this discrepancy. It is possible that the model for MLI which is released in these events and the ensuing orbit prediction is not well suited to these spacecraft and orbit types. It is also possible that the observation methods are not well suited to detect these objects. A deeper investigation of this issue is not part of the current work but should be adressed in future studies.

Figure 8.10 depicts the distribution of effective area-to-mass ratio of all detections of GEO and GTO MLI from the simulated surveys. The majority of detected objects have area-to-mass ratios below $10\,\mathrm{m}^2/\mathrm{kg}$ with some detected objects revealing ratios up to about $80\,\mathrm{m}^2/\mathrm{kg}$. The qualitative distribution is very similar to the one published in Schildknecht et al. (2010). Their histogram showed the frequency of derived effective area-to-mass ratios of 274 uncorrelated objects from a AIUB/ESA HAMR object catalog.

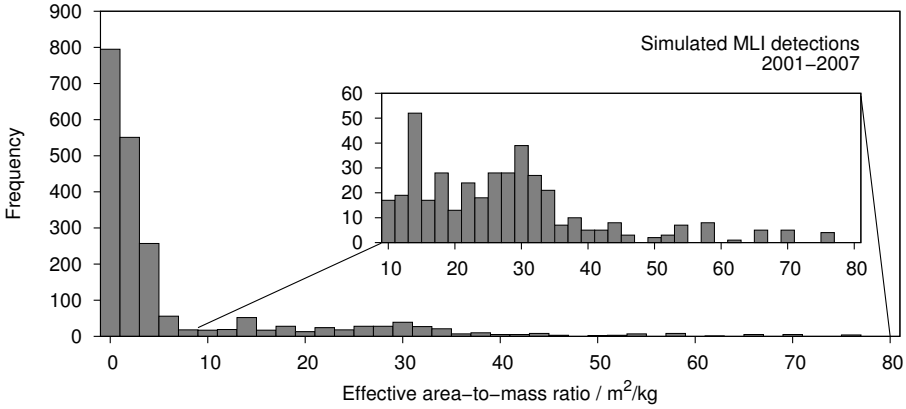

Figure 8.10: Histogram of effective area-to-mass ratio ($A/m \cdot C_R$) of all detected MLI objects using *PROOF*.

In Section 6.4.2, the orbit evolution of spherical HAMR GEO objects was investigated using a special perturbations propagator. The dependency of inclination of the modified Laplace plane on the effective area-to-mass ratio exhibited a near linear relation up to effective area-to-mass ratios of about $40\,\mathrm{m}^2/\mathrm{kg}$ (see Figure 6.4). The current Figure 8.11 compares this relation with the inclination and effective area-to-mass ratio of all simulated GEO MLI detections. The figure shows that the inclination of the detected objects for the most part remains below the previously derived relation for the maximum inclination. Detected MLI from GEO events exhibit effective area-to-mass ratios up to about $45\,\mathrm{m}^2/\mathrm{kg}$ although 90 % of the detected objects have ratios below $17\,\mathrm{m}^2/\mathrm{kg}$.

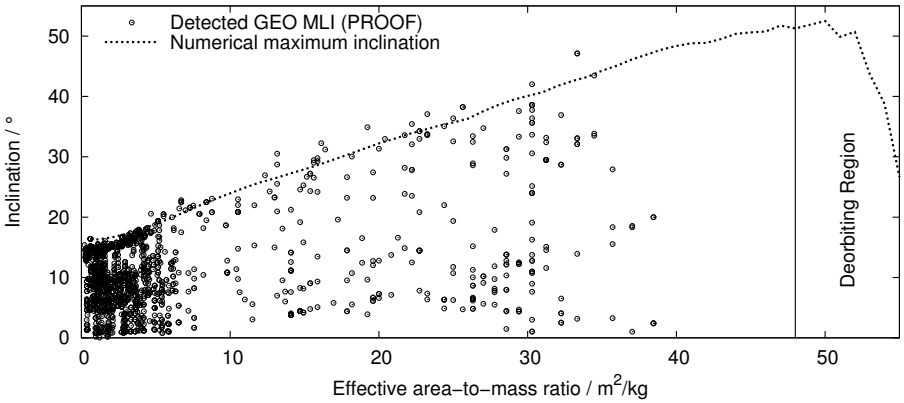

Figure 8.11: Inclination versus effective area-to-mass ratio of GEO MLI objects. The broken line is the relation of maximum attained inclination and effective area-to-mass ratio derived for spherical HAMR objects with initial GSO using a special perturbations model (Section 6.4.2). The circles show the relation of all MLI objects detected in the simulated campaigns using *PROOF*.

The eccentricities of the detected GEO MLI objects range from near 0 up to 0.76 with 90 % of the objects exhibiting eccentricities below 0.28. The remaining non-MLI GEO fragments all have eccentricities below 0.6 of which 90 % have much lower values below 0.06. The eccentricity versus mean motion of all detected objects is shown in Figure 8.12. The red dots are detections of non-MLI with origin in GEO events. The blue triangles represent detections of non-MLI with origin in GTO and the black rectangles are detected MLI. As already described, the MLI objects with mean motions around two were mostly created in explosions of former Soviet satellites on Molniya orbits. As with the effective area-to-mass ratio, this plot also exhibits the same principal features as the corresponding plot of 1057 uncorrelated tracklets presented by Schildknecht et al. (2010). In their publication, the uncorrelated high eccentricity GEO detections are spread more widely in mean motion. A possible cause could be that the MLI objects are simulated as spheres instead of flat plates which is likely to be a better approximation of their true shape. In Chapter 6 it was shown that the variation in semi-major axis may be a factor 10 higher for plate-like than for spherical MLI objects.

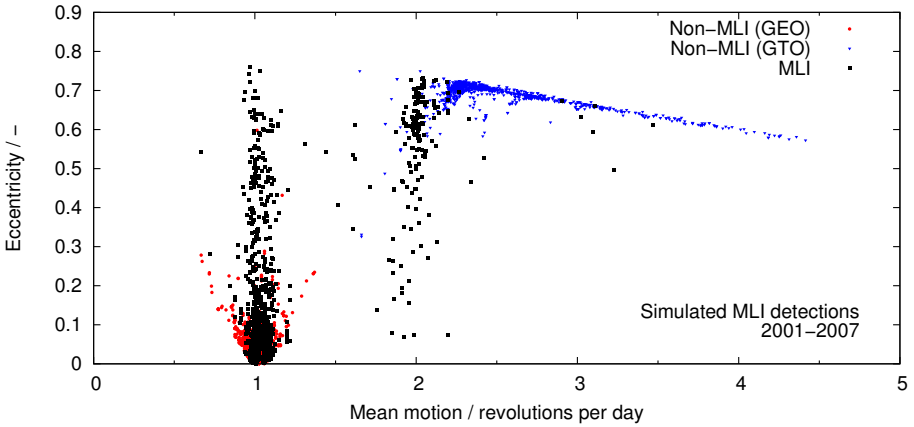

Figure 8.12: Eccentricity versus mean motion of all objects detected in the simulated campaigns using *PROOF*.

The histogram in Figure 8.13 compares the annual number of detections from the surveys to the simulated results for all magnitudes brighter than +22. The diagram shows that the overall trend in the simulated detections follows the measured detection rates quite well. The average deviation is about 12 % and the maximum deviation 24 %. The diagram also shows that detections of non-MLI GEO objects dominate the simulation results followed by GEO MLI and GTO non-MLI objects. Here, non-MLI objects are fragmentation debris which is modeled using the NASA Breakup Model. Table G.1 contains the exact detection numbers which underly this figure along with the results for the magnitude range +14 to +22.

The distribution of the magnitudes of the detected objects is shown in Figure 8.14 for the 2001 and 2006 surveys. The peak in the measurement data around +12 magnitude appears in all surveys and is persistently under predicted by the models. The much larger peak towards fainter objects is sometimes over- and sometimes under predicted by the models. The deviations in this region account for the overall variations also seen in the total detection numbers in Figure 8.13. The smaller peak for the brighter objects is characteristic of spacecraft and rocket

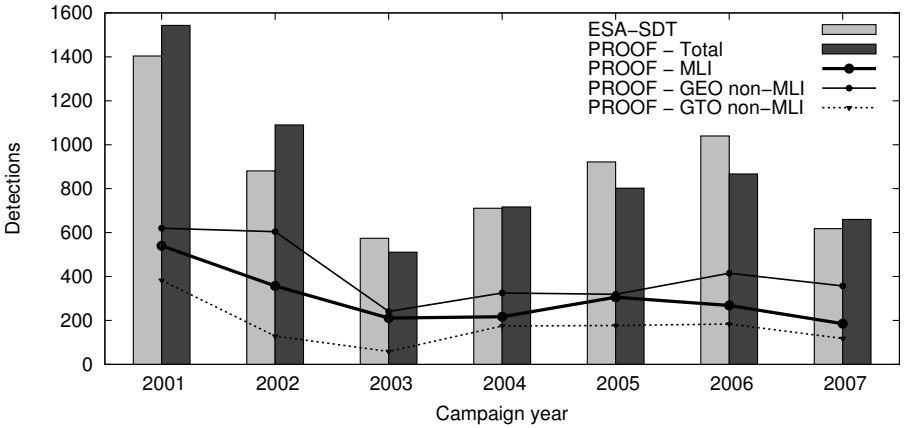

Figure 8.13: Comparison of all detections with magnitudes above +22 from ESA-SDT's 2001 to 2007 GEO and GTO surveys to simulated results using *PROOF* and updated populations. "GEO" objects are all detected objects with semi-major axis larger than 38,000 km. "GTO" objects are those objects with smaller semi-major axis below 38,000 km.

bodies which typically exhibit magnitudes between +10 and +15. It is possible that the uncorrelated detections in this range are sightings of cataloged objects for which orbit data is published but could nevertheless not be correlated. Another viable option is an abundance of objects for which no orbit data is published by the USSTRATCOM as is common practice for many signal intelligence satellites.

8.6 Error Analysis

The results presented in the previous section show good correlation between simulation results and observational data. To conclusively prove the validity of the simulations, the origin and properties of every detected object would have to be known. Paradoxically, were this data available, simulations would not be required. In support of the current results, alternate explanations for the large number of detections during the GTO campaigns have been analyzed. The core question to which an answer was sought was whether MLI debris or undetected

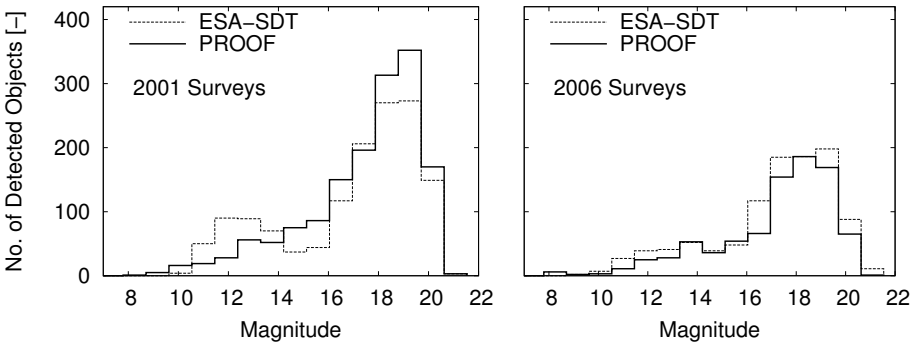

Figure 8.14: Apparent magnitude histogram for measured and simulated detections from the 2001 and 2006 surveys.

fragmentations in GEO could explain those detections which are currently covered by fragmentation debris of Ariane H10 3rd stages. To this end, four options have been explored whose results are presented in the following. Initially, it is reviewed whether MLI originating on GEO could be a significant contributor to this region. The possibility of GEO anomalous events is then examined in which large MLI debris pieces may be released. Following this, the underlying assumptions which were applied in deriving the velocity change which MLI obtains during a fragmentation are tested. The final option which is discussed is whether fragmentations may have gone undetected which would have occured on a GSO but whose combination of inclination and right ascension of ascending node is outside of the typical precession cone of equatorial GSO.

8.6.1 Drifting GEO MLI

Objects with low area-to-mass ratios which are on GSO and whose orbital plane coincides with the Laplace plane show only very small variations in inclination and right ascension of ascending node. Similar objects whose initial orbital plane have a different orientation precess about the Laplace plane normal vector. In Section 6.4 it was demonstrated that HAMR objects precess about modified Laplace planes. The dependency of the modified Laplace plane on the area-to-mass ratio can best be described using terms applied to keplerian orbits: While the inclination of these modified planes was found to increase sig-

nificantly for higher area-to-mass ratios, their right ascension of ascending node remained mostly constant. Furthermore, this precessing motion was seen to be superimposed by an annual variation of the orbit plane. This additional fluctuation causes HAMR objects whose initial orbit normal vector is located on the precession cone passing through the Earth's rotational axis to attain non-zero inclinations even at right ascension of ascending node values around $180\,^\circ$.

If the Laplace plane coincided with the Earth's equator, the drift of the right ascension of ascending node resulting from the precession would be constant. Due to its offset however, the drift rate is lowest near $\Omega = 0\,^\circ$ and highest around $\Omega = 180\,^\circ$. It can be concluded that if MLI were the source for the ESA-SDT detections which are outside of the precession cone of equatorial GSO, a continuous source of large MLI debris objects would be necessary. As was demonstrated in the introduction to Chapter 5, such a source model would lead to highly questionable results for future MLI debris predictions. In addition, the identification of the explosion debris of 1989-006B in ESA-SDT's 2001 surveys suggests that fragmentation debris from GTO events may be a better candidate for a large part of these detections.

8.6.2 Anomalous GEO Events

The most consistent source for information on anomalous events is the *History of On-Orbit Satellite Fragmentations* which is published by NASA's Orbital Debris Program Office. The latest edition is the 14^{th} and was made available in June of 2008 (Johnson et al. 2008). During anomalous events, typically small numbers of debris are released at low velocities. As indicated by Johnson et al. (2008), anomalous events "can be caused by material deterioration of items such as thermal blankets, protective shields, or solar panels, or by impact of small particles." A total of 51 such events have been recorded of which none occurred in the GEO region. It seems unlikely, however possible, that no such events have occurred on GEO. It is more probable that such events have so far eluded detection due to the small size of the created debris. Finally, MLI are known for their fast changing orbit parameters: the eccentricity oscillates with a period of about one year and can vary by as much as 0.8 during this time (see Section 6.4). It is therefore possible that objects were detected but could not be tracked. Other than the observations of some non-GEO anomalous events, no data is available which would support the presence of a large number of deterioration based debris. It

therefore seems unlikely that enough MLI has been created in anomalous events to contribute significantly to uncorrelated detections of ESA's SDT.

8.6.3 Velocity Imparted on MLI During Fragmentations

Changing the Δv applied to MLI objects within the simulation allows to examine its influence on the distribution of detections in inclination and right ascension of ascending node. If changing the Δv within reasonable boundaries leads to significant detections in i-Ω regions which are currently covered by simulated Ariane H10 fragments, then further investigations are required to determine how each source contributes to the observations. Since no test- or observational data is available detailing the velocity change of MLI debris specifically, the term *reasonable boundaries* can become very flexible. In lieu of such data, extreme values for velocity change which have been published for fragmentations and for non-catastrophic impacts are used as benchmarks. As test cases, the Δv given by the NASA Breakup Model was increased by factors 2, 4 and 6. The baseline Δv as published in Johnson et al. (2001) is used. The Δv which is applied within the MLI fragmentation model described in Section 7.3 is also based on this model but is reduced by a constant factor. Figure 8.15 shows the distribution of velocities among all MLI debris created in GEO fragmentations for the four scaling factors. The average velocity was increased from 0.17 km/s to 0.34 km/s, 0.68 km/s and to 1.02 km/s respectively. 98 % ($2\,\sigma$) of all MLI objects have velocities below 1.8 km/s for the unaltered NASA Breakup Model and below 10.6 km/s for the largest velocity increase. Cone ejecta are the only other debris source for which ejection velocities of a similar order of magnitude are known. For an impact velocity of 10 km/s, the cone ejection velocity can reach about 30 km/s (Flegel et al. 2011a). Due to the very specific conditions which must be met for such high velocities, it is very unlikely, that MLI could obtain such speeds during any fragmentation event. The observation campaigns between 2004 and 2007 of ESA's SDT were finally simulated using only these MLI populations with scaled velocities.

Simulated MLI detections brighter than magnitude +22 for the years 2004 to 2007 are combined into composite plots in Figure 8.16. The 2004 to 2007 surveys were selected as they include the GTO surveys in which most of the detections of objects which do not seem to follow the common orbit precession about the Laplace plane were made. It can be seen that even in the combined plots, only few de-

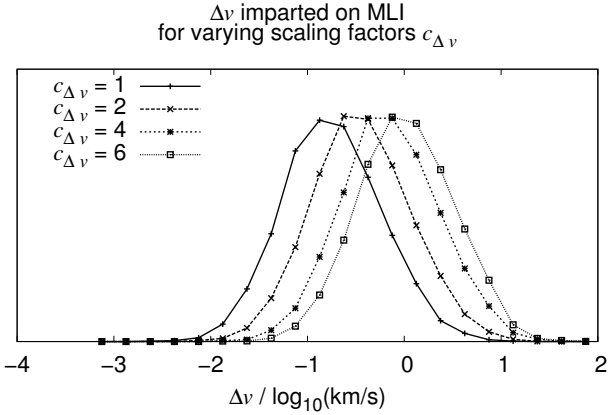

Figure 8.15: Δv distribution among MLI debris created in GEO fragmentations. Added velocity is increased by constant scaling factor $c_{\Delta v}$ = 2,4 and 6.

tections of MLI appear in the regions of interest. Combined with the extremely high Δv applied to create these results it seems all the more likely that GTO fragmentations are the major contributors to the i-Ω regions under consideration.

8.6.4 Events in Unconventional GEO Regions

Fragmentation clouds which are created in GSO and which produce larger, more massive objects all precess about a common pole which is the normal vector of the Laplace plane. The precession rate of the orbits of these objects depends mostly on the initial orbit plane orientation in relation to the Laplace plane. Since large, massive fragments typically obtain low Δv during fragmentation, their initial orbits are usually similar to that of the parent object. It follows that the orientation of the orbital planes of the debris remain comparable despite their precessing motion. This relation is used to spot debris belonging to individual fragmentation events near the GEO region. The only clouds which are visible in any of the surveys were created by objects whose initial orbit was close to the equatorial plane or which were on low inclination GTO. The probability for one or more fragmentation events to have occurred in a geosynchronous orbit whose

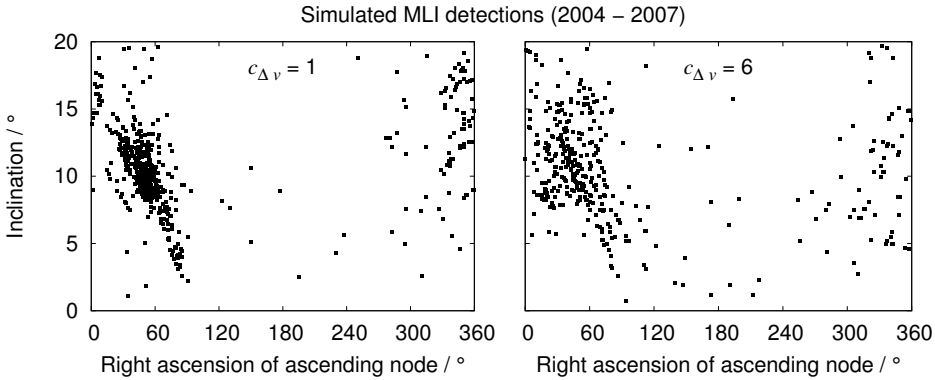

Figure 8.16: Influence of fragmentation Δv on detections of MLI. Simulated MLI detections are superimposed for the observation campaigns between 2004 and 2007. Left: original NASA Breakup Model Δv. Right: Δv increased by factor 6 compared to original NASA Breakup Model.

orbital plane did not originate in the equatorial plane is therefore considered to be low.

Chapter 9

Summary

The electromagnetic radiation from the Sun which impinges on an object is the primary source for radiation pressure acceleration. A realistic estimation of the amount of light which is reflected by MLI debris is therefore paramount to correctly simulate the resulting orbit perturbations. For modeling purposes an average reflectivity value is required which is representative of typical MLI foils. Optical properties published from in-situ and ground measurements for a wide range of materials which are commonly used for MLI were evaluated. From this data a mean initial reflectivity value of 0.87 was derived. Furthermore, it was found that degradation will likely cause the reflectivity to approach an end value asymptotically. Based on very limited data it was decided to use an end value of 0.33. The deterioration rate was found to vary considerably depending on mission altitude, orbit inclination, MLI material and orientation of the respective surface relative to flight direction. First estimates of the time until optical properties could approach the end value were based on the number of equivalent solar hours and assumed a linear degradation rate. For different missions and materials the estimated degradation time ranged from 6.6 to over 100 years. These values must be viewed with extreme caution due to the simplified approach.

The orbit evolution of high area-to-mass ratio (HAMR) spheres, HAMR plates and HAMR rotating plates was studied for the special case of geostationary orbits. For spherical objects it was found that simple linear or quadratic relations can often be found between the effective area-to-mass ratio and the beat period or beat amplitude and of inclination and eccentricity evolution. The evaluated effective area-to-mass ratios ranged from $1\,\mathrm{m}^2/\mathrm{kg}$ to about $60\,\mathrm{m}^2/\mathrm{kg}$. Above an area-to-mass ratio of about $48\,\mathrm{m}^2/\mathrm{kg}$ HAMR objects start interacting with the

upper atmosphere and deorbit within a few years. Plate-like objects exhibited markedly different orbit evolutions than spherical objects. Precession period, the orientation of the modified Laplace Plane as well as variations in the semi-major axis all were shown to depend largely on the principle inertial orientation of the objects.

Several key aspects of the MLI fragmentation source model were updated to include findings obtained in the course of this thesis. The most important changes affect the distribution of fragment sizes, the derivation of Δv assigned to MLI debris during fragmentations and the determination of the effective area. A simple model was derived for complex MLI fragments consisting of multiple foil layers which are created during fragmentation of a spacecraft. Several indications were revealed which suggest that the continuous source MLI model greatly overestimates the rate at which MLI separates from spacecraft. It was finally decided to remove this model, leaving fragmentation events as the sole contributor to MLI debris.

The ESA Space Debris Telescope surveys of the GEO and GTO regions which were performed between 2001 and 2007 were re-evaluated based on the updated MLI models. During these comparisons, compelling evidence was found that debris which has been created in at least nine violent fragmentations of Ariane H-10 upper stages between 1984 and 2002 has likely been underestimated in the past and may be the main contributor to detections of GTO fragments in these surveys. Specifically the debris cloud of 1989-006B which fragmented on January 1st 2001 is clearly visible in the survey results from that year. The overall results show that although MLI can attain much higher inclinations than other debris from GEO events, it is often difficult to discern MLI from other GEO fragmentation debris if only the orientation of the orbit normal vector is considered. A good method for identifying MLI debris is by also looking at the eccentricity and mean motion. While 90 % of non-MLI fragments with mean motions around 'one' remain at eccentricities below 0.06, the majority of MLI objects has eccentricities up to 0.6. The majority of simulated MLI debris has effective area-to-mass ratios below $40\,\mathrm{m}^2/\mathrm{kg}$ while a small number of objects may have values up to $100\,\mathrm{m}^2/\mathrm{kg}$. The modeling results show remarkable agreement with the distribution of tracklet data from the GEO and GTO surveys performed with ESA's Space Debris Telescope. In addition, long-arc data from HAMR objects which has been evaluated by (Schildknecht et al. 2010) is very well matched. The

absolute annual detection numbers support the conclusion that ageing related separation of MLI is quite likely only a small contributor to the visible debris population.

Chapter 10

Outlook

The relation between eccentricity build-up and area-to-mass ratio of GEO HAMR objects has a significant influence on the orbital lifetime and therefore on the nature of the in-orbit population. Future studies should investigate whether this aspect is modeled sufficiently well in the MLI fragmentation source model. Some sources for HAMR objects may still be ill-represented by the current model. In the past years, several Briz-M upper stages have experienced breakups for which currently no MLI fragmentation model exists.

Comparison of simulated GTO survey results to observations by ESA's Space Debris Telescope show an overprediction of simulated MLI debris created by Cosmos-863 type spacecraft. Possible sources for this discrepency should be explored. In the course of this thesis, a first re-evaluation of the list of Ariane H-10 fragmentation events has been undertaken which led to an increased correlation between simulations and observed debris. The applied changes however only account for a few variations between the individual H-10 events. A more in-depth study should be undertaken to obtain a more realistic picture of these fragmentation events.

Individual MLI foils are often separated by very light weight spacer netting. No dedicated model exists currently which takes this material into account. Due to its low reflective properties, it may be that a significant amount of netting material is in orbit which is not considered. Finally, complex MLI fragments consisting of several damaged layers of MLI could disintegrate over time. Since about 75 % of all MLI debris area is assumed to be "hidden" in this type of fragment, a post fragmentation release of MLI could be an important source to consider in the prediction of the future MLI debris environment.

Bibliography

Agapov, V., Molotov, I., Khutorovsky, Z. and Titenko, V. Analysis of the results of the 3 years observations of the geo belt and the heo objects by the ison network. In *Proceeding of the 59th International Astronautical Congress*. International Astronautical Federation, September 2008. Paper Number: IAC-08-A6.1.02.

Agapov, V., Molotov, I. and Khutorovsky, Z. Analysis of situation in geo protected region. In *Proceedings of the 10th Advanced Maui Optical Space Surveillance Technologies Conference, Maui, Hawaii*, September 2009.

Allan, R. and Cook, G. The long-period motion of the plane of a distant circular orbit. Technical report, Defense Documentation Center for Scientific and Technical Information, Cameron Station, Alexandria, Virginia, December 1963. Technical Note Space 52.

Anselmo, L. and Pardini, C. Orbital evolution of geosynchronous objects with high area-to-mass ratios. In *Proceedings of the Fourth European Conference on Space Debris*, pages 279 – 284, 18–20 April 2005. ESA SP-587.

Anselmo, L. and Pardini, C. Long-term dynamical evolution of high area-to-mass ratio debris released into high earth orbits. *Acta Astronautica*, 67:204 – 216, 2010. doi: 10.1016/j.actaastro.2009.10.017.

Banks, B. A., Backus, J. A., Manno, M. V., Waters, D. L., Cameron, K. C. and de Groh, K. K. Prediction of atomic oxygen erosion yield for spacecraft polymers. *Journal of Spacecraft and Rockets*, 48 No. 1:14 – 22, 2011.

Boeing. Boeing 702MP - Intelsat. 2013. Retrieved January 27 2013, from `http://www.boeing.com/defense-space/space/bss/factsheets/702/intelsat/intelsat.html`.

Bonnal, C. and Naumann, W. Ariane debris mitigation measures - past and future. *Acta Astronautica*, 40(2–8):275–282, 1997.

Bonnal, C., Sanchez, M. and Naumann, W. Ariane debris mitigation measures. In *Proceedings of the Second European Conference on Space Debris held in Darmstadt, Germany*, pages 681–688, 17–19 March 1997. ESA SP-393-681B.

Comins, N. F. and III, W. J. K. *Discovering the Universe*. W. H. Freeman and Company, New York, 5 edition, 2000. ISBN 0-7167-3637-3.

de Groh, K. K. and Smith, D. C. Investigation of Teflon FEP Embrittlement on Spacecraft in Low Earth Orbit. Technical Report NASA/TM-113153, National Aeronautics and Space Administration, Lewis Research Center, 1997.

de Groh, K. K., Banks, B. A., Sechkar, E. A. and Scheiman, D. A. Simulated Solar Flare X-Ray and Thermal Cycling Durability Evaluation of Hubble Space Telescope Thermal Control Candidate Replacement Materials. Technical Report NASA/TM-1998-207426, National Aeronautics and Space Administration, Lewis Research Center, 1998.

DeMars, K., Jah, M., Giza, D. and Kelecy, T. Orbit Determination Performance Improvements for High Area-to-Mass Ratio Space Object Tracking Using an Adaptive Gaussian Mixtures Estimation Algorithm. In *Proceedings of the 21st Internatinoal Symposium on Space Flight Dynamics*, 2009.

DeMars, K. J., Bishop, R. H. and Jah, M. K. Space Object Tracking in the Presence of Attitude-Dependent Solar Radiation Pressure Effects. In *Proceedings of the Astrodynamics Specialist Conference*, Girdwood, Alaska, USA, July 31 – August 4 2011. AAS / AIAA. Paper Number AAS 11-582.

Dever, J. A., de Groh, K. K., Townsend, J. and Wang, L. L. Mechanical Properties Degradation of Teflon ® FEP Returned From the Hubble Space Telescope. Technical Report NASA/TM-1998-206618, National Aeronautics and Space Administration, Lewis Research Center, January 1998.

ESA. Press Release No. 29-1997: New Cassini-Huygens launch date. July 16 1997. Retrieved January 30 2013, from `http://www.esa.int/For_Media/Press_Releases/New_Cassini-Huygens_launch_date`.

ESA. Venus express preliminary investigations bring encouraging news. 25 October 2005. Retrieved January 30 2013, from `http://www.esa.int/Our_Activities/Operations/Venus_Express_preliminary_investigations_bring_encouraging_news`.

ESA. EURECA (European Retrievable Carrier). 2008. Retrieved January 27 2013, from http://www.eoportal.org/directory/pres_EURECAEuropeanRetrievableCarrier.html.

ESA-ESTEC. Space product assurance – materials, mechanical parts and processes. Technical report, Noordwijk, The Netherlands, 6 March 2009. ECSS-Q-ST-70c.

European Space Operations Centre. **D**atabase and **I**nformation **S**ystem **C**haracterising **O**bjects in **S**pace (**DISCOS**). 2010. Retrieved from http://mas15.esoc.esa.de:9000/.

Finckenor, M. and Dooling, D. Multilayer Insulation Material Guidelines. Technical report, National Aeronautics and Space Administration, Marshall Space Flight Center, 1999. NASA/TP-1999-209263.

Fischer, E. Properties of multi-layer insulation debris. Studienarbeit, Institute of Aerospace Systems, Technische Universität Braunschweig, 2011. R-1131-S.

Flegel, S., Gelhaus, J., Möckel, M., Wiedemann, C., Kempf, D., Krag, H. and Vörsmann, P. Maintenance of the ESA *MASTER* Model – Final Report. Technical Report ESA Contract Number: 21705/08/D/HK, European Space Agency, June 2011a.

Flegel, S., Gelhaus, J., Möckel, M., Wiedemann, C., Krag, H., Klinkrad, H. and Vörsmann, P. Multi-layer insulation model for MASTER-2009. *Acta Astronautica*, 69:911 – 922, 2011b. doi: 10.1016/j.actaastro.2011.06.015.

Flegel, S. K. Modelling the High-Area-to-Mass Ratio Debris Popoulation in GEO. Studienarbeit, Institute of Aerospace Systems, Technische Universität Braunschweig, 2006. R-0603-S.

Flegel, S. K., Gelhaus, J., Wiedemann, C., Möckel, M., Braun, V., Vörsmann, P., Krag, H. and Klinkrad, H. Modeling multi-layer insulation debris in GEO. In *Proceedings of the 60th Deutsche Luft- und Raumfahrtkongress held in Bremen, Germany*, 27–29 September 2011c. No. DLRK2011-241286.

Flegel, S. K., Gelhaus, J., Möckel, M., Braun, V., Kebschull, C., Wiedemann, C., Vörsmann, P., Krag, H. and Klinkrad, H. Estimating the error in statistical

hamr object populations resulting from simplified radiation pressure modeling. In *Proceedings of the 13th Advanced Maui Optical Space Surveillance Technologies Conference, Maui, Hawaii*, 9–12 September 2012.

Früh, C. and Schildknecht, T. Investigation of Properties and Characteristics of High-Area-to-Mass- Ratio Objects Based on Examples of Optical Observation Data of Space Debris Objects in GEO-like Orbits. In *Proceedings of the 11th Advanced Maui Optical and Space Surveillance Technologies Conference*, September 2010.

Hamilton, W. R. *Researches Respecting Quaternions: First Series*, volume 21(1) of *Transactions of the Royal Irish Academy*. 1848.

Hi-Temp Insulation Inc. Brochure. Retrieved July 2, 2013, from `http://www.hi-tempinsulation.com/HTI%20brochure.pdf`.

IADC. Iadc space debris mitigation guidelines. Technical Report IADC-02-01, Inter-Agency Space Debris Coordination Committee, October 2002.

Johnson, N., Krisko, P., Liou, J.-C. and Anz-Meador, P. Nasa's new breakup model of evolve 4.0. *Advances in Space Research*, 28(9):1377 – 1384, 2001. ISSN 0273-1177. doi: 10.1016/S0273-1177(01)00423-9.

Johnson, N. L. Orbital Debris from Upper-Stage Breakup - Characteristics of the Ariane 1 Third Stage. *Progress in Astronautics and Aeronautics*, 121:100 ff., 1989. ISBN 0-930403-58-4.

Johnson, N. L., Stansbery, E., Liou, J.-C., Horstman, M., Stokely, C. and Whitlock, D. The characteristics and consequences of the break-up of the fengyun-1c spacecraft. In *Proceedings of the 58th International Astronautical Congress*. International Astronautical Federation, September 2007. Paper Number IAC-07-A6.3.01.

Johnson, N. L., Stansbery, E., Whitlock, D. O., Abercromby, K. J. and Shoots, D. History of On-orbit Satellite Fragmentations - 14^{th} edition. Technical Report NASA/TM-2008-214779, Orbital Debris Program Office, National Aeronautics and Space Administration, June 2008.

Kauder, L. Spacecraft Thermal Control Coatings References. Technical report, National Aeronautics and Space Administration, Goddard Space Flight Center, 2005. NASA/TP-2005-212792.

Kelecy, T. and Jah, M. Analysis of Orbital Prediction Accuracy Improvements using High Fidelity Physical Solar Radiation Pressure Models for Tracking High Area-to-Mass Ratio Objects. In *Proceedings of the Fifth European Conference on Space Debris, Darmstadt, Germany*, March 30 – April 2, 2009a.

Kelecy, T. and Jah, M. Analysis of Orbit Prediction Sensitivity to Thermal Emissions Acceleration Modeling for High Area-to-mass Ratio (HAMR) Objects. In *Proceedings of the 10th Advanced Maui Optical Space Surveillance Technologies Conference, Maui, Hawaii*, 2009b.

Kelecy, T. and Jah, M. Analysis of high area-to-mass ratio (HAMR) GEO space object orbit determination and prediction performance: Initial strategies to recover and predict HAMR GEO trajectories with no a priori information. *Acta Astronautica*, 69:551 – 558, 2011. doi: 10.1016/j.actaastro.2011.04.019.

Kelecy, T., Jah, M. K. and DeMars, K. Application of a Multiple Hypothesis Filter to Near GEO High Area-to-Mass Ratio Space Objects State Estimation. In *Proceedings of the International Astronautical Congress*, Cape Town, South Africa, October 2011. International Astronautical Federation. Paper Number IAC-11-C1.2.12.

Klinkrad, H. and Martin, C. *Space Debris - Models and Risk Analysis*. Springer-Praxis Books in Astronautical Engineering, 2006. ISBN 3-540-25448-X.

Krag, H., Klinkrad, H., Jähn, R., Oswald, M., Flegel, S. and Schildknecht, T. Improving geo space debris environment modelling with the help of esa space debris telescope observations. In *Proceedings of the 37th COSPAR Scientific Assembly*. Committee on Space Research, July 2008.

Krisko, P. Proper Implementation of the 1998 NASA Breakup Model. *Orbital Debris Quarterly News*, 15(4), October 2011.

Krisko, P. H., Horstman, M. and Fudge, M. L. SOCIT4 collisional-breakup test data analysis: With shape and materials characterization. *Advances in Space Research*, 41(7):1138 – 1146, 2008. doi: 10.1016/j.asr.2007.10.023.

Leitenberger, B. Die Titan 3+4. 2009. Retrieved July 2, 2013, from `http://www.bernd-leitenberger.de/titan34.shtml`.

Leitenberger, B. Die Geschichte der Europarakete Ariane. 2010. Retrieved August 6, 2013, from `http://www.bernd-leitenberger.de/ariane23.shtml`.

Marco, J. and Remaury, S. Evaluation of Thermal Control Coatings Degradation in Simulated GEO-Space Environment. In *High Performance Polymers*, volume 16, pages 177 – 196. SAGE Publications, September 2004. doi: 10.1177/0954008304044102.

Marshall, J. A. and Luthcke, S. B. Modeling radiation forces acting on Topex/Poseidon for precision orbit determination. *Journal of Spacecraft and Rockets*, 31(1):99 – 105, January–February 1994.

Molotov, I., Agapov, V. et al. International scientific optical network for space debris research. *Advances in Space Research*, 41:1022 – 1028, 2008. doi: 10.1016/j.asr.2007.04.048.

Montenbruck, O. and Gill, E. *Satellite Orbits*. Springer-Verlag Berlin Heidelberg New York, 2000. ISBN: 3-540-67280-X.

Morrisey, D. C., Maybee, D. C., Staples, J. W. and Skartvedt, C. G. Development of the Titan III Transtage ACS Hydrazine Monopropellant Rocket Engine Modules. In *Proceedings of the AIAA 5th Propulsion Joint Specialist Conference held at the U.S. Air Force Academy in Colorado*, 9–13 June 1969. AIAA Paper No. 69-422.

Murakami, J. Micro-Satellite Impact Tests To Investigate Multi-Layer Insulation Framgents. Graduate thesis, Space Systems Dynamics Laboratory, Kyushu University, 2008.

Murakami, J. Personal communication, April 13 2009.

Musci, R., Schildknecht, T. and Ploner, M. Analyzing long observation arcs for objects with high area-to-mass ratios in geostationary orbits. *Acta Astronautica*, 66:693 – 703, 2010. doi: 10.1016/j.actaastro.2009.08.025.

Oswald, M. Generierung und Darstellung von Objektwolken mit ungleichmäßiger Richtungsverteilung der zusätzlichen Geschwindigkeiten am Beispiel eines Flüssigkeitsaustritts auf einer niedrigen Erdumlaufbahn. Diplom thesis, Institute of Aerospace Systems, Technische Universität Braunschweig, 2001.

Oswald, M., Stabroth, S., Wiedemann, C., Wegener, P., Martin, C. and Klinkrad, H. Upgrade of the MASTER Model – Final Report. Technical Report ESA Contract Number: 18014/03/D/HK(SC), European Space Agency, April 2006.

Park, L. T., Corbin, J. D. and Ernst, R. D. Titan Transtage Spacecraft Propulsion System. In *Proceedings of the AIAA/SAE 9th Propulsion Conference held in Las Vegas, Nevada*, 5–7 November 1973. AIAA Paper No. 73-1210.

Picone, J., Hedin, A., Drob, D. P. and Aikin, A. C. Nrl-msise-00 empirical model of the atmosphere: Statistical comparisons and scientific issues. *Journal of Geophysical Research*, 107(1468):16 ff., 2002. doi: 10.1029/2002JA009430.

Pisacane, V. L. and Moore, R. C., editors. *Fundamentals of Space Systems*. JHU/APL series in science and engineering. Oxford University Press, Inc., 1994.

Remaury, S., Nabarra, P., Bellouard, E. and d'Escrivan, S. In-Flight Aging of Thermal Coatings: THERME Experiment. *Journal of Spacecraft and Rockets*, 48 (1):27 – 33, January–February 2011. doi: doi:10.2514/1.49377.

Rosengren, A. J. and Scheeres, D. J. Long-term dynamics of high area-to-mass ratio space debris in geo. In *Proceedings of the 63rd International Astronautical Congress*. International Astronautical Federation, 2008. IAC-12-A6.2.5.

Schildknecht, T. Optical surveys for space debris. *Astron Astrophys Rev*, 14:41 – 111, 2007. doi: 10.1007/s00159-006-0003-9.

Schildknecht, T. Personal communication, August, 15 2013.

Schildknecht, T., Musci, R., Ploner, M., Beutler, G., Flury, W., Kuusela, J., de Leon Cruz, J. and de Fatima Dominguez Palmero, L. Optical observations of space debris in GEO and in highly-eccentric orbits. *Advances in Space Research*, 34:901 – 911, 2004. doi: 10.1016/j.asr.2003.01.009.

Schildknecht, T., Musci, R., Flury, W., Kuusela, J., de Leon Cruz, J. and de Fatima Dominguez Palmero, L. Optical observations of space debris in high-altitude orbits. In *Proceedings of the Fourth European Conference on Space Debris*, pages 113–118, 2005. ESA SP-587.

Schildknecht, T., Flohrer, T., Musci, R. and Jehn, R. Statistical analysis of the ESA optical space debris surveys. *Acta Astronautica*, 63:119 – 127, 2008a. doi: 10.1016/j.actaastro.2007.12.035.

Schildknecht, T., Musci, R. and Flohrer, T. Properties of the high area-to-mass ratio space debris population at high altitudes. *Acta Astronautica*, 41:1039 – 1045, 2008b. doi: 10.1016/j.asr.2007.01.045.

Schildknecht, T., Musci, R., Früh, C. and Ploner, M. Color photometry and light curve observatinos of space debris in geo. In *Proceedings of the 9th Advanced Maui Optical and Space Surveillance Technologies Conference*, September 2008c.

Schildknecht, T., Vananti, A., Krag, H. and Klinkrad, H. European efforts to survey, track, and characterize small-size objects at high altitudes. In *Proceedings of the 8th US/Russian Space Surveillance Workshop*, Maui, HI, USA, April 2010.

Sheldahl. The red book, April 2006. Retrieved from `http://www.sheldahl.com/Products/WebPages/RedBook.aspx`.

Sheldahl. The red book, 2009. Retrieved from `http://www.sheldahl.com/Products/WebPages/RedBook.aspx`.

Sheldahl. The red book, August 2012. Retrieved from `http://www.sheldahl.com/Products/WebPages/RedBook.aspx`.

Stadermann, F. J., Heiss, C. H. and Reichling, M. Evaluation of impact craters on solar cell samples and thermal MLI blankets. *Advances in Space Research*, 20(8): 1517–1521, 1997.

Steiner, B. Personal communication, April 10 2013.

Townsend, J. A., Hansen, P. A., McClendon, M. W., Dever, J. A. and Triolo, J. J. Evaluation and selection of replacement thermal control materials for the hubble space telescope. Technical report, 1998.

Vallado, D. A. An Analysis of State Vector Propagation Using Differing Flight Dynamics Programs. In *Proceedings of the Spaceflight Mechanics Conference*, Copper Mountain, CO, January 23–27 2005. AAS/AIAA. Paper Number AAS 05-199.

Vallado, D. A. and McClain, W. D. *Fundamentals of Astrodynamics and Applications*. Published jointly by Microcosm Press and Springer, 3^{rd} edition, 2007. ISBN 978-0-387-71831-6.

Wade, M. Ariane - Encyclopedia Astronautica. 2013a. Retrieved August 6, 2013, from `http://www.astronautix.com/fam/ariane.htm`.

Wade, M. Ariane H10 - Encyclopedia Astronautica. 2013b. Retrieved August 6, 2013, from http://www.astronautix.com/stages/arineh10.htm.

Wade, M. Titan Transtage - Encyclopedia Astronautica. 2013c. Retrieved July 2, 2013, from http://www.astronautix.com/stages/titstage.htm.

Wright, I., Sexton, A. and Grady, M. EURECA Multi-Layer Insulation Impact Morphology and Residue Analysis - Final Report (Contract No: RFQ/3-8001/94/NL/JG). 1995. Retrieved January 27 2013, from http://space-env.esa.int/madweb/eureca/mli/reports/oumli/oumlirp.php.

Appendix A

Equivalent Solar Hours

This section derives the equivalent solar hours (ESH) *per year* of significant satellite surfaces. The factor C is the number of hours in a year ($C = 365.25\,\mathrm{d/a} \cdot 24\,\mathrm{h/d}$). The angles ϕ and γ are two orthogonal angles for the offset of the surface-Sun vector from the surface normal vector.

$$
\begin{aligned}
ESH_{\text{GEO, E/W}} &= C \cdot \frac{180^\circ}{47^\circ \cdot \pi} \cdot \int_{\gamma=-23.5^\circ}^{+23.5^\circ} \left(\frac{1}{2\pi} \int_{\phi=-\pi/2}^{+\pi/2} \cos\gamma \cos\phi \, d\phi \right) d\gamma && \text{(A.1)} \\
&\approx 2712\,\mathrm{h} \\
ESH_{\text{GEO, N/S}} &= C \cdot \frac{180^\circ}{23.5^\circ \cdot \pi} \cdot \frac{1}{2} \cdot \int_{0}^{+23.5^\circ} \sin\gamma \, d\gamma && \text{(A.2)} \\
&\approx 886\,\mathrm{h} \\
ESH_{\text{SSO, 6:00}} &= C \cdot \frac{180^\circ}{47^\circ \cdot \pi} \cdot \frac{1}{2} \cdot \int_{-23.5^\circ}^{+23.5^\circ} \cos\phi \, d\phi && \text{(A.3)} \\
&\approx 8522\,\mathrm{h} \\
ESH_{\text{SSO, 12:00}} &= C \cdot \frac{1}{2\pi} \cdot \int_{-\pi/2}^{+\pi/2} \cos\phi \, d\phi && \text{(A.4)} \\
&\approx 2790\,\mathrm{h}
\end{aligned}
$$

Appendix B

Area-to-Mass Ratio of HAMR Fragments

Table B.1 lists the fragments from two ground tests performed at Kyushu University split by tests, area-to-mass ratios and fragment types. Fragment types are inner-layer MLI foils, outer- or cover-layer MLI foils and complex fragments. Complex fragments consist of partially or completely intact MLI blankets.

Table B.1: Area-to-mass ratio distribution of fragments from ground tests performed by Murakami (2008). Table was also derived by Fischer (2011). All area-to-mass ratio values in m^2/kg

		Number of MLI fragments					
log	A/m in	*Shot F*			*Shot R*		
A/m	m^2/kg	*Inner*	*Outer*	*Complex*	*Inner*	*Outer*	*Complex*
0.3	2.00	0	0	0	0	0	1
0.4	2.51	0	1	0	0	0	2
0.5	3.16	0	0	1	0	0	1
0.6	3.98	0	1	4	0	0	0
0.7	5.01	0	2	0	0	0	0
0.8	6.31	0	0	1	0	0	0
0.9	7.94	0	0	4	0	0	0
1.0	10.00	0	1	4	0	0	0
1.1	12.59	1	3	1	0	1	0

log A/m	A/m in m^2/kg	Number of MLI fragments					
		Shot F			*Shot R*		
		Inner	*Outer*	*Complex*	*Inner*	*Outer*	*Complex*
1.2	15.85	0	14	3	0	10	0
1.3	19.95	1	15	0	0	16	0
1.4	25.12	0	13	1	0	15	0
1.5	31.62	3	4	0	1	3	0
1.6	39.81	1	1	0	0	4	0
1.7	50.12	6	2	0	2	1	0
1.8	63.10	13	1	0	5	1	0
1.9	79.43	23	2	0	10	0	0
2.0	100.00	10	0	0	6	1	0
2.1	125.89	1	0	0	0	2	0
2.2	158.49	2	0	0	1	0	0
2.3	199.53	1	0	0	3	1	0
2.4	251.19	0	0	0	1	0	0
2.5	316.23	0	0	0	0	0	0
2.6	398.11	0	0	0	0	0	0
2.7	501.19	0	0	0	0	0	0
2.8	630.96	0	0	0	0	0	0
2.9	794.33	0	0	0	1	0	0
3.0	1000.00	0	0	0	1	0	0
3.1	1258.93	0	0	0	0	0	0
3.2	1584.89	0	0	0	1	0	0
Sum:		62	60	19	32	55	4
Mean A/m:		76.73	23.34	9.60	98.27	32.47	2.55
Pristine A/m:		88.50	28.57	6.82	88.50	28.57	6.82
$\Delta A/m$ in %:		-13.29	-18.30	+40.78	+11.04	+13.64	-62.68

Appendix C

Eccentricity versus Effective Area-to-Mass Ratio

The influence of the area-to-mass ratio of a spherical GEO object on the eccentricity oscillation period is studied. Orbit propagation using the numerical propagator *ZUNIEM* is performed over a time frame of 10,000 days (see Section 6.4). The equation which could be fit to the data points from the numerical simulation results for the eccentricity period is given by Equation C.1. The unit is 'years'.

$$\epsilon_{\text{Period}}\left(\frac{A}{m}\right)_{\text{eff}} = \left(-0.0190807 \cdot \left(\frac{A}{m}\right)^2_{\text{eff}} - 0.0612214 \cdot \left(\frac{A}{m}\right)_{\text{eff}} + 372.621\right)/365.25 \tag{C.1}$$

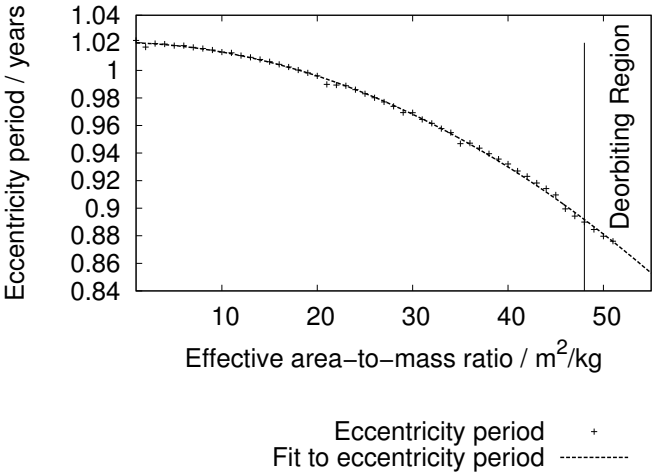

Figure C.1: Spheres: Dependency of maximum eccentricity on effective area-to-mass ratio ($A/m \cdot C_r$). Data points from numerical simulation and fit to data.

Appendix D

Special Perturbations

D.1 Radiation Pressure

The generalized special perturbations equation for any radiation pressure acceleration is given by equation D.1. This equation expands on the one given in Section 6.2 in that it includes indices for additional radiation sources and thermal re-radiation. It must be possible to approximate the object's surface through a finite number of flat surfaces i. Self radiation is however *not* taken into account.

$$\boldsymbol{a}_{\text{RP}} = -\frac{1}{m_{\text{sat}}\, c} \cdot \sum_{i=1}^{n} \left[\sum_{\text{src}=1}^{\text{m}} \left(\Phi_{\text{src}}\, S_{\text{src}}\, \boldsymbol{R}_{i,\,\text{src}}\, \frac{(\boldsymbol{s}_{i,\,\text{src}} \circ \boldsymbol{n}_i)}{\|\boldsymbol{s}\|_{i,\,\text{src}} \cdot \|\boldsymbol{n}\|_i}\, A_i \right) + \boldsymbol{P}_i\, A_i \right] \tag{D.1}$$

n	total number of surface elements of object	–
m	total number of radiation sources	–
$\boldsymbol{a}_{\text{RP}}$	radiation pressure acceleration	m/s
m_{sat}	satellite mass	kg
c	speed of light	m/s
A_i	area of flat surface element i	m^2
Φ_{src}	electromagnetic radiation flux from radiation source *src*	W/m^2
S_{src}	shadow function for radiation source *src*	$\in [0,1]$
$\boldsymbol{R}_{i,\,\text{src}}$	specular and diffuse reflection terms for flat surface element i relative to radiation source *src*	$R \in [1,2]$

$\boldsymbol{s}_{i,\,\mathrm{src}}$	vector pointing from surface element i to radiation source *src*	m
$\boldsymbol{n}_i$	surface element i normal vector	m
$(\boldsymbol{s}_{i,\,\mathrm{src}} \circ \boldsymbol{n}_i)$	$\|\boldsymbol{s}\|_{i,\,\mathrm{src}} \cdot \|\boldsymbol{n}\|_i \cdot \cos\alpha$, with α according to Figure 6.2	–
$\boldsymbol{P}_i$	radiation emitted from surface element i (i.e. through thermal re-radiation)	W/m2

D.2 Rotating Motion

All rotating objects are gyroscopes. The motion of a gyroscope can be modelled using Euler's equations of motion. The direction cosine matrix of the previous section describes the orientation of an object within our inertial frame. Euler's equations of motion are used to obtain the *change* in the rotation axis relative to the inertial ECI frame. The link between these two formulations is given by a description of an object rotating about an axis which is *fixed* in the ECI frame. The following two steps are therefore required:

1. Generic change in orientation of body frame relative to ECI frame is expressed as function of angular velocity vector $\boldsymbol{\omega}$
2. Angular velocity vector changes are described through Euler's equations of motion

Kinematic Equation for Body Frame in Inertial Frame The rotating motion of the object is accounted for by the kinematic equation. For quaternions, the relation can be written as:

$$\dot{\boldsymbol{q}}_B^E = \frac{1}{2} \cdot \begin{bmatrix} 0 & -r & q & p \\ r & 0 & -p & q \\ -q & p & 0 & r \\ -p & -q & -r & 0 \end{bmatrix} \cdot \boldsymbol{q}_B^E, \tag{D.2}$$

where

$$\begin{pmatrix} p \\ q \\ r \end{pmatrix} = \begin{pmatrix} p_B \\ q_B \\ r_B \end{pmatrix}^E = \boldsymbol{\omega}_B^E \tag{D.3}$$

is the angular velocity vector of the body frame expressed in the ECI frame. In each time step Equation D.2 must be integrated to obtain the new orientation of the object:

$$\boldsymbol{q}\left(t_1\right) = \boldsymbol{q}\left(t_0\right) + \int_{t_0}^{t_1} \dot{\boldsymbol{q}}\, dt. \tag{D.4}$$

Care must be taken that the constraint in Equation 6.11 is meat. The result can then be inserted into Equation 6.14.

Euler's Equation of Motion Finally, the change in the angular velocity vector must be modelled. Any rotating object may be simulated by Euler's equation of motion:

$$\boldsymbol{M} = \dot{\boldsymbol{L}} + \boldsymbol{\omega} \times \boldsymbol{L}. \tag{D.5}$$

$\boldsymbol{M}$ are external moments, $\boldsymbol{L}$ is the angular momentum vector and ω is the angular velocity vector from Equation D.3. The angular momentum is the product of the moment of inertia tensor $\underline{\underline{J}}$ and the angular velocity vector:

$$\boldsymbol{L} = \underline{\underline{J}} \cdot \boldsymbol{\omega} \qquad\qquad \dot{\boldsymbol{L}} = \underline{\underline{J}} \cdot \dot{\boldsymbol{\omega}}. \tag{D.6}$$

It is assumed that the origin of the body frame is positioned on the center of mass of all simulated objects. In this case, all components spare the diagonal of the moment of inertia tensor become zero:

$$\underline{\underline{J}} = \begin{bmatrix} J_{xx} & 0 & 0 \\ 0 & J_{yy} & 0 \\ 0 & 0 & J_{zz} \end{bmatrix}. \tag{D.7}$$

Rearranging equation D.5 and inserting D.7 results in the relation for the change in the angular velocity vector:

$$\dot{\boldsymbol{\omega}} = \begin{pmatrix} \dot{p} \\ \dot{q} \\ \dot{r} \end{pmatrix} = \begin{pmatrix} J_{xx}^{-1}\left[qr\left(J_{yy} - J_{zz}\right) + M_x\right] \\ J_{yy}^{-1}\left[pr\left(J_{zz} - J_{xx}\right) + M_y\right] \\ J_{zz}^{-1}\left[pq\left(J_{xx} - J_{yy}\right) + M_z\right] \end{pmatrix}. \tag{D.8}$$

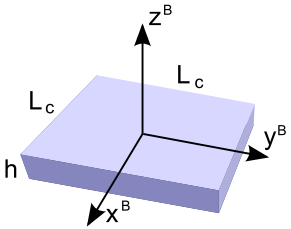

Figure D.1: The body frame has its origin in the center of mass

Integration again produces the new angular velocity vector in each time step:

$$\boldsymbol{\omega}(t_1) = \boldsymbol{\omega}(t_0) + \int_{t_0}^{t_1} \dot{\boldsymbol{\omega}}\, dt \tag{D.9}$$

Moment of Inertia The generic equations for the moment of inertia tensor components are:

$$\begin{aligned} J_{xx} &= \int_m \left(y^2 + z^2\right) dm \\ J_{yy} &= \int_m \left(x^2 + z^2\right) dm \\ J_{zz} &= \int_m \left(y^2 + y^2\right) dm \end{aligned} \tag{D.10}$$

x, y and z are the axes of the body frame with its origin in the center of mass. In the current work, all objects are assumed to be square plates. Using equation 5.10 and defining the body frame according to Figure D.1, the components of the moment of inertia tensor are derived:

$$\begin{aligned} J_{xx} &= \frac{m}{12}\left(L_c^2 + h^2\right) \\ J_{yy} &= \frac{m}{12}\left(h^2 + L_c^2\right) \\ J_{zz} &= \frac{m}{6} L_c^2 \end{aligned} \tag{D.11}$$

Appendix E

Orbit Evolution of Plates

The current chapter shows the short- and long-term evolution of plate-like objects with initial geosynchronous orbits in the equatorial plane. At $\pm 90\,^{\circ}$ in-plane rotation, the object's normal vector is oriented perpendicular to the incident solar radiation during those times when its orbit intersects the Earth's shadow. For this case, the secular effect on semi-major axis is small over the time-frame of 1,000 days (Figure E.1). In the 10,000 day results, its effect is on the order of the $\pm 30^{\circ}$ cases (Figure E.2). The extreme case in eccentricity for the out-of-plane orientation is given by the $\pm 90^{\circ}$ case where the object is oriented with its normal vector parallel to the Earth's rotation axis $\hat{\boldsymbol{K}}$ (see Figure 6.7). In this case, only the Earth's tilt against the ecliptic causes the object's surfaces to be illuminated by the Sun leading to a maximum tilt angle with respect to the Sun of $23.45\,^{\circ}$. The influence of SRP on the orbit evolution is lowest in this case.

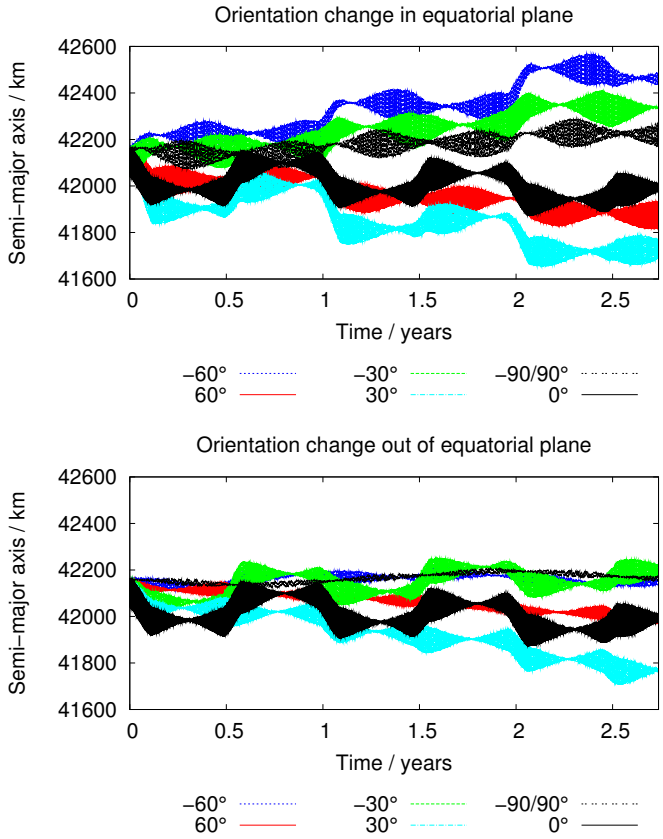

Figure E.1: Fixed plates: Change in semi-major axis over 1,000 days. Top: surface normal vector is rotated around Z-axis of ECI. Bottom: surface normal vector is rotated about Y-axis of ECI.

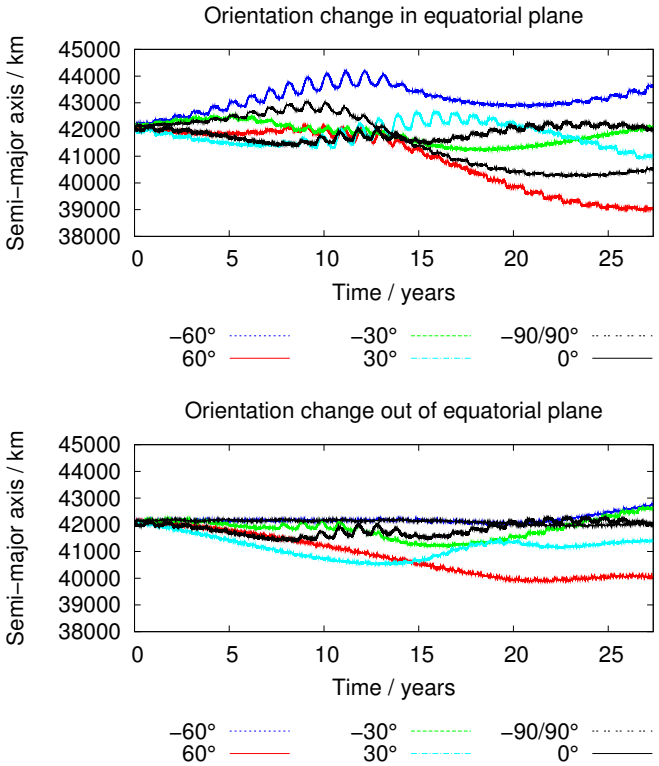

Figure E.2: Fixed plates: Change in semi-major axis over 10,000 days. Top: surface normal vector is rotated around Z-axis of ECI. Bottom: surface normal vector is rotated about Y-axis of ECI.

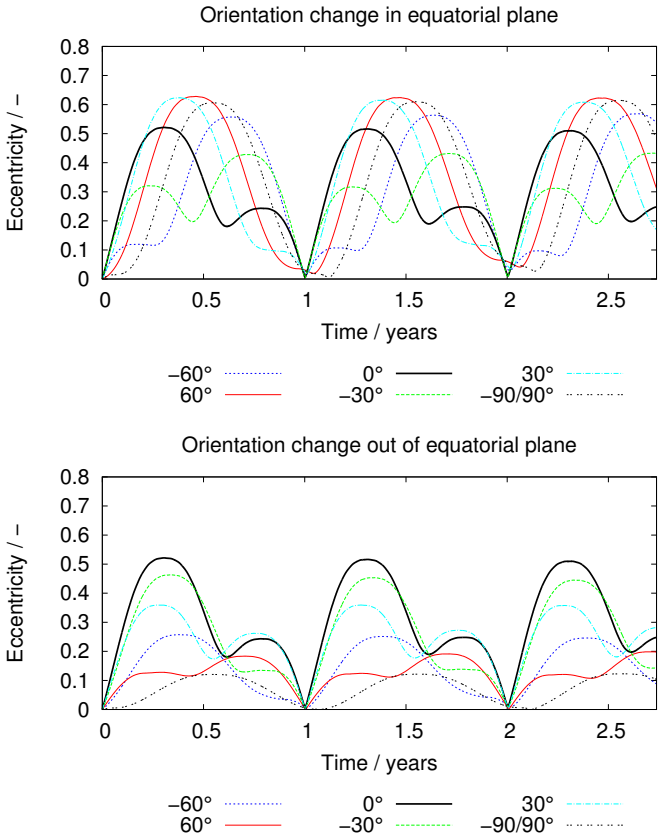

Figure E.3: Fixed plates: Change in eccentricity over 1,000 days. Top: surface normal vector is rotated around Z-axis of ECI. Bottom: surface normal vector is rotated about Y-axis of ECI.

Appendix F

Average Illuminated Area: $F_{\text{rotating plate}}$

Let A_{eff} be the time average projected area, or *effective* area, of a plate-like object rotating about an axis in its surface plane. The single-side surface area of the object is A. The rotation rate is ω and the rotation period $T = 2\pi/\omega$. The effective area of the rotating plate at time t is given by:

$$A_{\text{eff}}(t) = A \cdot \cos(\omega t) \tag{F.1}$$

To obtain A_{eff}, the projected area is integrated over one half rotation $= T/2$. To remove the time parameter in the solution, the result is divided by $T/2$. This leads to the following deriviation:

$$\begin{aligned} A_{\text{eff}} &= \frac{A}{T/2} \int_{-T/4}^{-T/4} \cos(\omega t)\, \delta t \\ &= A\, \frac{2}{T\,\omega} \sin(\omega t) \Big|_{-T/4}^{T/4} \\ &= A \frac{2}{T\,\omega} \left[\sin\left(\frac{\pi}{2}\right) - \sin\left(-\frac{\pi}{2}\right) \right] \\ &= A \frac{2}{T\,\omega} \cdot 2 \end{aligned} \tag{F.2}$$

With $T = 2\pi/\omega$, this resolves to

$$A_{\text{eff}} = A\frac{2}{\pi} \tag{F.3}$$

This relation shows that the single-side surface area is reduced by a factor of $2/\pi$, thus leading to

$$F_{\text{rotating plate}} = \frac{2}{\pi} \tag{F.4}$$

Appendix G

Detection Results

Table G.1 compares the annual detections from the ESA SDT's surveys between 2001 and 2007 to the simulated detections. The results are given for all detections brighter than +22 magnitude and for the range +14 to +22 magnitude. The latter range is introduced as spacecraft typically have magnitudes brighter than +14. Above this threshold, some classified spacecraft may have been detected which could not be correlated. Since these are not covered by the models the reduced range in magnitudes eases the comparison of the models to the observation data.

Table G.1: Comparison of detections from ESA-SDT's 2001 to 2007 GEO and GTO surveys to simulated results using PROOF-2009 and updated populations. "GEO" objects are all detected objects with semi-major axis larger than 38,000 km. "GTO" objects are those objects with smaller semi-major axis below 38,000 km.

		2001	2002	2003	2004	2005	2006	2007
Magnitudes 0 to +22								
PROOF	MLI	540	357	211	217	306	268	185
	GEO non-MLI	620	604	241	325	319	415	357
	GTO non-MLI	383	129	59	175	177	184	118
	Total	**1543**	**1090**	**511**	**717**	**802**	**867**	**660**
ESA-SDT		**1404**	**881**	**574**	**711**	**922**	**1040**	**618**
Magnitudes +14 to +22								
PROOF	MLI	437	296	168	171	225	192	137
	GEO non-MLI	560	551	209	301	279	365	324
	GTO non-MLI	352	122	52	165	165	171	113
	Total	**1349**	**969**	**429**	**637**	**669**	**728**	**574**
ESA-SDT		**1090**	**721**	**480**	**563**	**764**	**862**	**478**